Process Induced Residual Stress in Thermoset Polymer with Metallic Insert

---

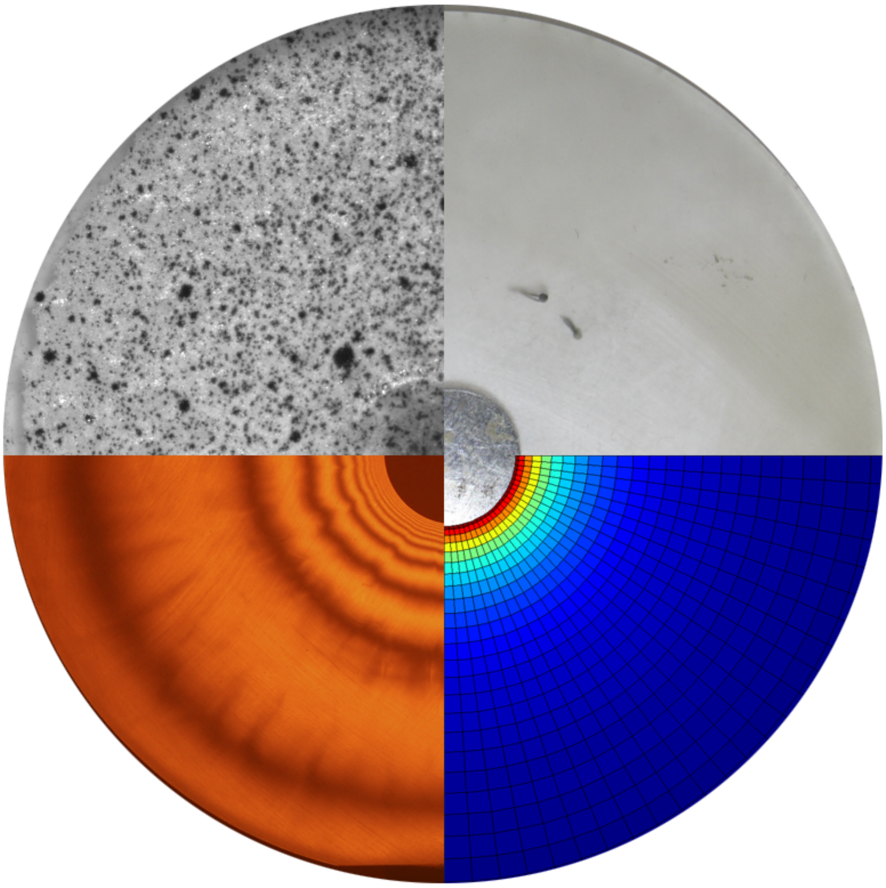

4^{th} semester, MSc
Jens Grandjean Jørgensen
Design of mechanical systems
Aalborg University
3^{rd} June 2014

School of-
Engineering and Science
Mechanical & Manufacturing
Engineering
Fibigerstraede 16
9220 Aalborg East

Title:
Process Induced Residual Stress in Thermoset Polymer with Metallic Insert
Theme:
Master's Thesis

Period:
DMS4, spring semester 2014
23^{rd} January - 3^{rd} June

Project group:
2.217c - Fib16

Participant:

Jens Grandjean Jørgensen

Supervisors:
Johnny Jakobsen
Lars Rosgaard Jensen

Pages:
85 (75)

Appendix number:
9

Synopsis:

In this project, process induced stress and strain in a simple epoxy test specimen, with a steel insert, is considered. The subject is studied by both experimental and numerically methods.

Through experimental in-situ measurements, using digital image correlation (DIC), the average strain is obtained, and afterwards separated into a thermal and a chemical contribution.

The residual stress of the test specimen is evaluated by using photoelasticity. However, the stress-optical law is not valid for this problem, because the temperature varies over time. Hence, another approach is considered, where the change in the photoelastic measurement is considered, when the insert is removed. This is considered to yield good results of the residual stress at the end of the process.

The test specimen is furthermore considered theoretically through a numerical model. The model is based on the finite element method (FEM), and has been coded in MATLAB. It includes the chemical curing process and material properties, which is dependent on degree of cure and temperature. Different material models have been implemented in the numerical model, based on elastic, viscoelastic, or pseudo-viscoelastic considerations.

The numerical model yields strain results which correlate very well with the average strain, obtained by the DIC measurements. By using the pseudo-viscoelastic model, known as the cure hardening instantaneously linearly elastic (CHILE) model, reasonable correlation with the photoelastic stress measurements is obtained.

Resumé

Projektet omhandler proces inducerede tøjninger og egenspændinger i et simpelt testemne af hærdeplast, hvori der er indstøbt en metalindsats. Igennem projektet er der udført både eksperimentelle forsøg, og numeriske simuleringer af testemnet, for at evaluere spændinger og tøjninger.

Testemnet er som udgangspunkt uhærdet epoxy i en cirkulær silikoneform, hvor der i midten er placeret en cylindrisk stålindsats. Når emnet udhærdes i en ovn dannes der egenspændinger. Egenspændingerne opstår, fordi epoxyens volumen ændre sig, som følge af selve processen, mens stålindsatsens volumen kun påvirkes i mindre grad. Det medfører, at epoxyens deformation begrænses af stålindsatsen, hvormed der opstår spændinger.

For at begrænse, at testemnets deformation påvirkse af udefrakommende faktorer, er der designet en form med meget lav stivhed. Formen er støbt af silikone, og har en godstykkelse på 2 mm. Det medfører at testemnet kan deformere næsten uhindret, gennem hele processen.

Volumenændringen i epoxyen sker på grund af to forskellige fænomener. Det ene fænomen er, at epoxyen krymper når det hærder, på grund af den kemiske reaktion. Dette sker dog imens temperaturen er høj, hvormed stivheden er lav og epoxyen forventes at opføre sig viskoelastisk. Det vil sige, at det kemiske krymp ikke medfører egenspændinger i stor grad. Det andet fænomen er volumen ændringen på grund af den termiske udvidelse i materialet. Det får epoxyen til at krympe når emnet nedkøles efter at hærdeprocessen er fulført. Denne del forventes at være årsag til hoveddelen af egenspændingerne.

Testemnet betragtes som nævnt både eksperimentelt of teoretisk. Den eksperimentelle del består af forsøg med en metode, kendt som ”digital image correlation” (DIC), samt spændingsoptiske forsøg. DIC målingerne forudsætter, at der er et passende stokastisk mønster på overfladen af emnet, som kan identificeres og følges af systemet. En række forskellige metoder, til at opnå et sådan mønster på overfladen af uhærdet epoxy, er undersøgt. Det viser sig, at ekspanderet perlit med et stænk af sort spray maling giver et fornuftigt mønster. DIC målingerne udføres igennem hele processen, hvor der tages billeder af testemnet imens det er i ovnen, under både hærdeprocessen og den efterfølgende nedkøling. Ud fra målingerne detekteres gel-dannelsen, og den gennemsnitlige tøjning i testemnet bruges til at bestemme det kemiske og termiske krymp.

Desuden udføres spændingsoptiske forsøg, hvor testemnet betragtes i et polariskop. Her forsager spændinger i emnet mørke linjer, som kan relateres til spændingstilstanden. Linjerne kan dog ikke relateres direkte til spændingstilstanden, i dette tilfælde, fordi processen foregår ved varierende temperatur. Derfor udføres i stedet forsøg, hvor ændringen i de spændingsoptiske målinger betragtes, når stålindsatsen fjernes fra testemnet. Ved denne metode opnås fornuftige målinger af spændingstilstanden i emnet.

Igennem projektet der er udviklet en numerisk model, der kan simulere spændinger og deformationer i test emnet. Modellen bygger på elementmetoden (FEM), og er kodet i MATLAB. Som en del af modellen estimeres udhærdningsgraden ud fra temperaturforløbet. Udhærdningsgraden og temperaturforløbet bruges desuden til at estimere de øjebliklige mekaniske egenskaber, som anvendes i den mekaniske model.

Der er blevet implementeret fire forskellige materialemodeller, for at vurdere hvilken tilgang der giver det bedste resultat. Den simpleste er en elastisk model, der dog overestimere spændingstilstanden betydeligt. Derudover er der implementeret to forskellige viskoelastiske modeller. Den ene er Kelvin modellen, som, på baggrund af de estimerede materiale parametre, giver stort set samme resultat som den elastiske model. Den anden viskoelastiske model er Maxwell modellen, som viser sig at underestimere spændingerne betydeligt. Den sidste materialemodel er kendt som CHILE modellen. Denne viser sig at give fornuftige resultater.

Preface

This project report is written by Jens Grandjean Jørgensen during 4^{th} semester of the master program in ”Design of Mechanical Systems” at Aalborg University. The project concerns ”Process Induced Residual Stress in Thermoset Polymer with Metallic Insert”.

Prior to this preface, page V, a short summery is given in Danish.

In this project sources are as a main rule cited by surname and year. A list of bibliography is found at page 87. The used nomenclature is found on page XI.

The main report consists of three parts. Before the first part, an introduction to the problem is given in chapter 1. Part I consider the experimental approach to the project, whereas part II consider the numerical modelling. In the end, in part III, the results are presented.

The appendixes are included at the end of this document, as part IV. Appendix I is a list of the contents on the appendix CD. It contains e.g. the report as a PDF file, MATLAB-scripts and LabView VI's. Throughout the report, the appendix CD is referred to as appendix I.

Contents

Nomenclature

Symbol:	Description:	Unit:
D''	Loss compliance	$[\mathrm{Pa}^{-1}]$
D'	Storage compliance	$[\mathrm{Pa}^{-1}]$
D_I	Instantaneous compliance	$[\mathrm{Pa}^{-1}]$
D	Compliance modulus	$[\mathrm{Pa}^{-1}]$
E''	Loss modulus	[Pa]
E'	Storage modulus	[Pa]
E_f	Young's modulus of the fibre material	[Pa]
E_m	Young's modulus of the matrix material	[Pa]
E^0_{CSM}	Initial modulus of CSM composite, before gelation	[Pa]
E^{ult}_{CSM}	Ultimate modulus of CSM composite	[Pa]
E_{CSM}	In-plane Young's modulus for CSM composite	[Pa]
E^{ult}_m	Ultimate modulus of epoxy matrix	[Pa]
E_{subT_g}	Maximum attainable modulus at a given degree of cure	[Pa]
E	Young's modulus	[Pa]
G_f	Shear modulus of the fibre material	[Pa]
G_m	Shear modulus of the matrix material	[Pa]
N	Fringe order	[ ]
P	Force	[N]
R	Ideal gas constant	$\left[\frac{\mathrm{J}}{\mathrm{mol\,K}}\right]$
S_{ij}	Compliance matrix	$[\mathrm{Pa}^{-1}]$
T_g	Glass transition temperature	[K]
T_{gel}	Temperature at which gelation occur	[K]
T	Temperature	[K]
V_f	Volume fraction of fibres	[ ]
$[M]$	Matrix in constitutive relation	$[\mathrm{Pa}^{-1}]$
$[V]$	Matrix which includes Poisson's ratio	[ ]
$\Delta(\sigma_1 - \sigma_2)$	Change in principal stress difference	[Pa]
ΔN	Change in fringe order	[ ]

Continued on next page

Symbol:	**Description:**	**Unit:**
$\Delta\sigma$	Increment in stress	[Pa]
$\Delta\varepsilon$	Increment in strain	[ ]
Δt	Time increment	[s]
α_{aT_g}	Coefficient of thermal expansion above T_g	$\left[\mathrm{K}^{-1}\right]$
α_{bT_g}	Coefficient of thermal expansion below T_g	$\left[\mathrm{K}^{-1}\right]$
α	Coefficient of thermal expansion	$\left[\mathrm{K}^{-1}\right]$
β	Chemical shrinkage rate parameter	[ ]
η	Viscosity	$\left[\frac{\mathrm{kg}}{\mathrm{sm}}\right]$
γ^H	hereditary shear strain	[ ]
γ	Shear strain	[ ]
ν_f	Poisson's ratio of the fibre material	[ ]
ν_m	Poisson's ratio of the matrix material	[ ]
ν	Poisson's ratio	[ ]
ω_{load}	Frequency of the applied load	$[\mathrm{s}^{-1}]$
$\dot{\varepsilon}_{dashpot}$	Strain rate of dashpot element	$[\mathrm{s}^{-1}]$
$\dot{\varepsilon}_{spring}$	Strain rate of spring element	$[\mathrm{s}^{-1}]$
$\dot{\varepsilon}$	Strain rate	$[\mathrm{s}^{-1}]$
$\dot{c}$	Rate of cure	$[s^{-1}]$
σ_1	First principal stress	[Pa]
σ_2	Second principal stress	[Pa]
σ_x	Stress in the x-direction	[Pa]
σ_y	Stress in the y-direction	[Pa]
σ	Stress	[Pa]
τ_{xy}	Shear stress w.r.t. the x and y axes	[Pa]
θ	Angle between fibre direction and axis 1	[rad]
ε^0	Strain which is calculated with respect to the initial deformation state	[ ]
ε^H	Hereditary strain	[ ]
ε^m	Mechanical strain	[ ]

Continued on next page

Symbol:	**Description:**	**Unit:**
ε^{end}	Strain which is calculated with respect to the final deformation state	[ ]
ε_x	Strain in the x-direction	[ ]
ε_y	Strain in the y-direction	[ ]
ε_{chem}	Chemical strain	[ ]
ε_{therm}	Thermal strain	[ ]
ε	Strain	[ ]
c_{gel}	Degree of cure at gel point	[ ]
c_{max}	Maximum degree of cure at a given temperature	[ ]
c	Degree of cure	[ ]
f_σ	Fringe constant	$\left[\frac{\mathrm{N}}{\mathrm{m}}\right]$
h	Height of plane specimen	[m]
m_i	Parameter in the model for $\dot{c}$	[ ]
n_i	Parameter in the model for $\dot{c}$	[ ]
n_{elem}	Number of elements in meshed model	[ ]
$n_{samples}$	Number of samples	[ ]
n_{time}	Number of time steps	[ ]
r_i	Inner radius	[m]
r_o	Outer radius	[m]
r	Radius	[m]
t'	Dummy variable of time	[s]
t_{gel}	Time at which gelation occur	[s]
t	Time	[s]

1 Introduction

Fibre reinforced composite parts are used in a wide variety of industries, where low mass and high performance are required. Fibre composites are superior to other materials, such as metals, due to the high strength and stiffness to mass ratio, and the possibility of producing parts with complex geometries. The composite can consist of many different material combinations, to improve e.g. strength, stiffness, impact resistance, heat resistance, mass, or price of a part. A combination which is commonly used is glass fibre and a thermosetting polymer, such as epoxy.

To be able to transfer loads into composite structures, it is typically necessary to include metallic inserts. However, commonly used design methods do not predict the local stress field around inserts. If the stress field is not known, the full potential of fibre reinforced polymers cannot be utilized.

In figure 1.1 and 1.2, two examples of composite structures with metallic inserts are shown. Figure 1.1 is the root section of wind turbine blade, where the insert for bolting the blade to the hub is moulded into the root section. [Gardiner, 2012] In other cases, the inserts are joined mechanically to the root section of the wind turbine blade. [Black, 2013]

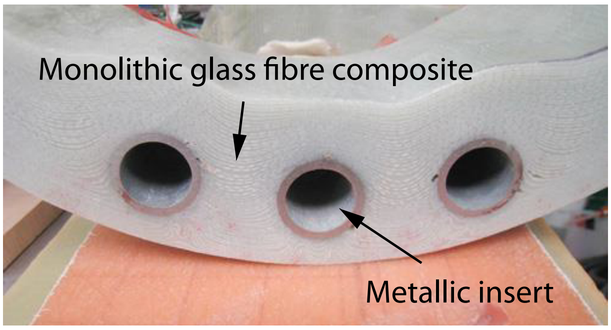

Figure 1.1 Root section of a wind turbine blade, which is produced with molded-in inserts. [Gardiner, 2012]

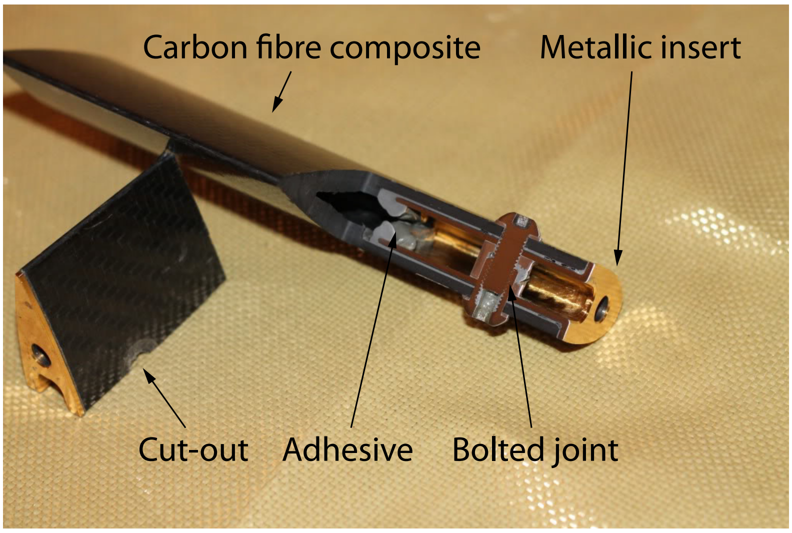

Figure 1.2 Cut-out of a formula one pushrod, where a titanium insert is glued and bolted to the end of a carbon fibre rod. [Garvey, 2010]

Figure 1.2 shows an insert in a pushrod in the suspension of a formula one race car. The carbon fibre pushrod has been machined in the end, after which an insert of titanium is joined to the rod by adhesives and a bolted joint. This might not be either the strongest or lightest solution[1]. It might be a better solution to mould the insert into the part, thereby avoiding the adhesive and the bolted joint.

The insert will typically cause a stress concentration in the surrounding material, due to the geometry and the difference in stiffness. However, the stress field around an insert is also affected by the manufacturing process, if the insert is moulded into the structure. The curing process can induce residual stress in the part, which can cause deformations, and either reduce or increase the strength of the part. Residual stresses occur if the material surrounding the insert is restricted in it deformation. Likewise, residual stresses occur on a microscopic level, if the fibre material undergoes different volumetric strains than the matrix material. Most thermoset composite materials do undergo volumetric strains during the process. The volumetric strain is partly caused by thermal expansion. Generally, metals and common fibre materials, such as steel and glass fibre, has low thermal expansion, compared to e.g. epoxy. A thermosetting polymer, furthermore undergo a volumetric strain when it cures due to the chemical reaction.

Residual stress around an insert is assessed to be a relevant problem in composite structures as well as neat thermosetting polymer structures. However, there is no literature, to the author's knowledge, concerning this specific problem. Most literature regarding process induce residual stresses consider stresses and deformations in fibre composite laminate. Hahn and Pagano [1975] are among the first, to publish literature on the subject. Subsequently, others, such as: Nairn and Zoller [1985], White and Hahn [1992a], White and Kim [1998], Johnston et al. [2001], Ruiz and Trochu [2005], and Abou-Msallem et al. [2010] have studied the subject as well. Other authors has made more general approach, where e.g. Fuhong et al. [2007] has conducted an analysis of residual stress by using a 3D finite element method. Zobeiry [2006] considers 3D as well, but considers viscoelastic effects as well.

To be able to utilize the full potential of the material, it is necessary to understand how the manufacturing process affects the stress field around an insert. If it can be predicted by a model, it might be possible to use that to change the design or manufacturing parameters to increase the performance of a fibre composite structure.

1.1 Problem statement

A simple test specimen, in which residual stress is induced during curing, is considered. The goal of the project is to:

- Use experimental methods to obtain stress and strain measurements during and after the curing process.
- Develop a numerical model to simulate the process. In addition to the mechanical system, the model should include the curing kinetics and models of the material properties which varies during the process.

---

[1] It should be noted, that this is probably a pushrod of a former formula one car, hence, it is not assessed to be the state of the art solution for pushrods.

- Validate the numerical model, by comparing the simulated stress and strain field with the experimental measurements.

The scope of the project is simplified to considering only a neat epoxy resin, with a metallic insert. Hence, the test specimen is produced without fibres.

The project is divided into two parts, part I which considers the experimental study of the stress and strain field, and part II which considers the numerical model. Both parts include variations of the experimental test configurations. The test specimen is described in section 1.2.

1.2 Test specimen

Throughout the project, a test specimen is considered both physically and theoretically. Hence, the term ”test specimen” denotes both the physical object used in the experiment, and the computer model which is simulated numerically.

The experiment, which is performed both physically and numerically, consist of a test specimen of uncured epoxy resin, with a metallic insert. The test specimen is studied during and after the curing process, where various methods are used to obtain the strain and stress field.

The test specimen should be a simple geometry of epoxy resin, in which a metallic insert is placed to induce residual stress. It should be designed so it is easy to produce consistent specimens, it should be simple to model, and it should be possible to obtain good stress and strain measurements.

The geometry is chosen as a circular disc, with a circular steel insert in the middle, as shown in figure 1.3.

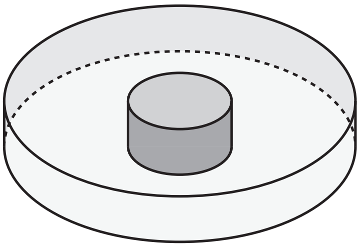

Figure 1.3 Sketch of test specimen

The geometry of the test specimen is very simple, by which it is simple to model. Because the test specimen is symmetric, it is not necessary to model the entire part. The geometry is also considered to be easy to discretise, because the outline is easily formulated mathematically.

It is considered, that the test specimen is not very sensitive to geometrical inaccuracies. If e.g. the outer geometry is uneven, or if the position of the insert is out of centre, it is not considered to affect the stress or strain measurements significantly. This is because the boundary of the test specimen is considered to be far from the local stress field around the insert. However, the thickness of the test specimen should be even, and the geometry of the insert should be well-defined.

In addition to the geometry, it is also necessary to have well defined boundary conditions. Hence, the mould in which the test specimen is cast should be designed with that in mind.

It is desired that the boundaries should either be free, by which no loads are transferred, or fixed, by which no displacement is allowed. A fixed boundary condition would be obtained by making the mould rigid and ensuring good adhesion between the epoxy and the mould surface. However, it would limit the deformation of the test specimen, and thus make the experiment less interesting.

A free boundary condition can be obtained by a very compliant mould, or by a surface with negligible friction and adhesion.

It has been attempted to cast a test specimen on surfaces with low friction. Hence, two test specimens have been cast, on teflon and kapton foil respectively. The adhesion of the epoxy on the foils was low, by which it was easy to peel off the foils afterwards. However, because the epoxy does bond to the foils, it requires a large shear load to get slip. Hence, the friction on the surface cannot be neglected.

Thus, it is decided to make a compliant mould for the test specimen, by which the boundaries are considered to be free.

The dimensions of the test specimen are chosen, as shown in figure 1.4. The thickness of the physical test specimen is approximately 6 mm, as described in section 2.5.

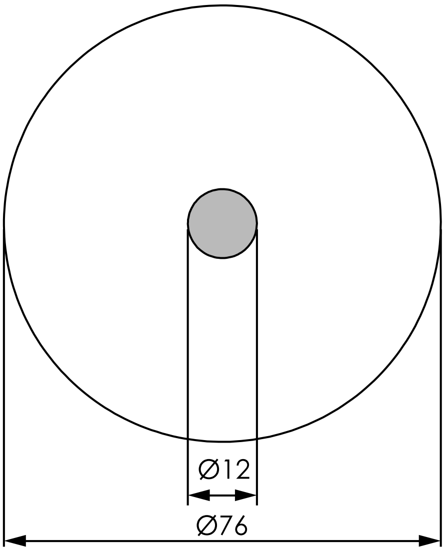

Figure 1.4 Drawing of test specimen, with dimensions in millimetres.

1.3 Process

In this section, the process which is considered throughout the project is described. It is, on a general level, described how the experiments are conducted, and how the residual stress is formed.

At the start, the epoxy is in the viscous phase. The curing process of the epoxy resin is activated at the time of mixing, however, the curing reaction is accelerated when the test specimen is heated. [Osswald and Menges, 2003]

The first part of the process is where the curing process occurs. The curing process is an irreversible chemical reaction, where cross-links are formed between the polymer chains of the epoxy resin. [Osswald and Menges, 2003] By forming cross-links, the epoxy builds up the mechanical properties. However, at the same time, a chemical shrinkage occurs. This chemical shrinkage is considered to cause residual stresses, as the metallic insert does not strain due to the chemical reaction.

However, when the epoxy is in the viscous phase, it cannot sustain any stress, because viscous stresses require a strain rate. Hence, the chemical shrinkage does not cause residual stresses until the epoxy enters the rubber phase. The transition from the viscous phase to the rubber phase is known as the gel point. [Osswald and Menges, 2003] The gel point is defined as ”the instant at which the weight average molecular weight diverges to infinity” [Winter, 1987] due to chemically cross-linking. Furthermore, the gel point is the point, after which residual stresses may start to form in the material. [Abou-Msallem et al., 2010]

In the stage, after the curing process is complete, there is no chemical shrinkage. If the temperature is constant, there is neither thermal expansion. Even so, the residual stress might not be constant. According to several authors, the epoxy behaves viscoelastic in the rubber phase (e.g. Lin and Yi [1990], White and Kim [1998], Ruiz and Trochu [2005], and Juliano et al. [2007]). Some authors even assumes that the structure is ”stress free” before it is cooled [Hahn and Pagano, 1975] [White and Hahn, 1992a]. However, according to Abou-Msallem et al. [2010], residual stresses remain in the part, unless the stress is above the yield stress.

The last stage is the cooling. In this stage, the negative thermal expansion causes the epoxy to contract, by which residual stress occur. At some point during the cooling, the temperature becomes less than the glass transition temperature, T_g. At this point, the epoxy transforms into the glass phase, where it behaves more elastic. Hence, the residual stress which is induced during the final stage of cooling is not expected to vanish due to relaxation.

In figure 1.5, a temperature history of a curing process is sketched together with the degree of curing and the glass transition temperature (T_g).

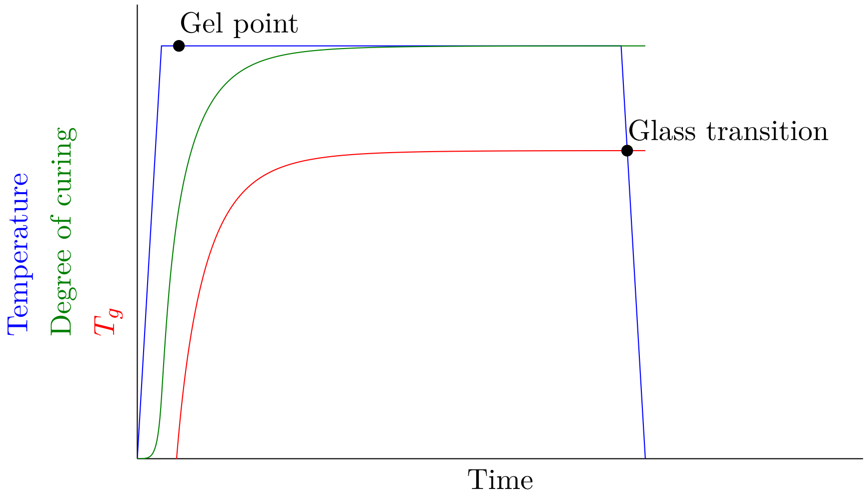

Figure 1.5 Sketch of the temperature, degree of curing, and T_g during the curing process.

In the figure, the gel point is marked. As described above, the epoxy resin is viscous before the gel point, and rubbery after. The point, until which chemical shrinkage occur in the test specimen, is where the degree of curing reaches a constant level. And, finally the glass transition, where the epoxy transforms into the glass phase, is maked as the point where the temperature crosses the graph of T_g.

Part I

Experimental approach

In this part of the report, experimental approaches are considered to determine the stress and strain field of the test specimen, during and after the curing process.

In chapter 2, a number of different experimental methods, which can be used to determine the stress and strain field, are considered.
Every experiment is based on the same circular test specimen of uncured epoxy, with a cylindrical steel insert. Digital image correlation (DIC) is used to obtain in-situ strain measurements of the test specimen, as described in chapter 3. Photoelasticity is used to obtain stress measurements, as described in chapter 4.

Experimental methods 2

In this chapter, a number of different experimental methods, which can be used to obtain the stress or strain field of the test specimen, are considered. However, it is not a complete study of available methods. In section 2.5, it is described how the test specimen is prepared for the experiments.

Ideally, in-situ measurements of the entire stress and strain field are to be performed. From the measurements the following phenomena should be identified and correlated with the numerical model, considered in part II:

- Gel point
- Visco-elastic behaviour
- Thermal expansion
- Chemical shrinkage
- Stress and strain field around the insert
- Temperature

2.1 Strain measurements

A commonly used method for measuring deformations of mechanical structures is strain gauges. Kim and Daniel [2002] has used both fibre optic and electrical resistance strain gauges to measure strains in a fibre composite laminate during curing. It is assessed that such a method could be used in this project. However, the method cannot be used to evaluate the entire strain field, as the strain gauge only measures the strain at a single point. Furthermore, to measure the strain of the epoxy test specimen, the deformation of the strain gauge must follow the deformation of the test specimen. However, it is considered that the stiffness of the epoxy is very low at the time of gelation, by which the strain gauge might be too stiff to follow the deformation.

Another method is to observe the global deformation of the test specimen. A method, which is used for fibre laminates, is to consider the process induced curvature of a thin laminate with unsymmetrical lay-up. This method is used by White and Hahn [1992b] to evaluate the residual stress of a graphite-bismaleimide composite. However, this method cannot be used on the specific test specimen, considered in this project.

A full field strain measurement can be obtained by using Digital Image Correlation (DIC). The DIC method determines the deformation of a body, by comparing images of the undeformed and the deformed state. The method requires a stochastic pattern on the surface of the test specimen, by which small subsets of the images, known as facets, can be matched between two (or more) images by using a correlation function. This results in a full displacement field of the area which is considered. The system uses one or two cameras to capture images of the test specimen, by which either 2D or 3D measurements can be obtained [Hamilton, 2011]. This method has been used by Peiris [2008] to make in-situ shrinkage analysis of epoxy resin during curing and to detect the gel point.

The DIC system can only determine deformations in the surface of the test specimen, and it requires the stochastic pattern to be applied on the uncured epoxy resin, if the entire process is to be considered. Furthermore, the resolution of the results is limited by the quality of the surface pattern. However, it requires no contact with the test specimen, and the system is available in the laboratory. Hence, the method is used in this project, as described in chapter 3.

2.2 Stress measurements

Generally very few methods exist, which can be used to measure stresses directly. Most methods are based on deformation measurements, which are converted to stresses through a constitutive law.

However, photoelasticity is a method which is insinuated by both Dally and Riley [1991], and Phillips [1998] to be related to the stress. However, both describe photoelasticity as a method for determining the stresses in structures, by considering a scale model in a polariscope, within the linearly elastic region. The method is based on light, which is illuminated through optical elements and the loaded test specimen. This causes fringes to appear in the test specimen, which are related to the principal stress difference. [Phillips, 1998] The relation between the fringes and the principal stress difference is described in more details in chapter 4. This method is used to study the test specimen, as the equipment is available in the laboratory, and because it is a simple method to determine the full field stress distribution.

To study the viscoelastic behaviour of the test specimen, the stress relaxation is to be observed by photoelastic measurements during the curing process.

A different category of test, which can be used to study the residual stressed in the test specimen is destructive tests. One method is based on layer removal of a laminate, and is related to the method which considers curvature of unsymmetrical lay-up. One or more layers are removed from a laminate, after which residual stresses through the thickness causes the remaining layers to deform. [Parlevliet et al., 2007] However, this method is not suitable for this specific test specimen.

A commonly used destructive tests for determining residual stress is based on hole drilling. By drilling a small hole in the test specimen, the residual stress is released in the surrounding material. This causes a deformation which can be measured by e.g. strain gauges. [Parlevliet et al., 2007] Another approach is to determine the deformation by DIC measurements or the stress field by photoelastic measurements. A disadvantage of this method is, it is only applicable on the test specimen at the end of the process, when the test specimen is cured and cooled. Still, the method is assessed to be suitable for the test specimen, considered in this project.

The residual stress is considered to be largest in the area close to the metallic insert, by which the hole should be drilled close to the insert. However, in this area the deformation, caused by the residual stress, might be affected by the insert, which complicates the measurement. Hence, a method is used, which is inspired by the hole drilling method, where the entire insert is removed, and the stress field is observed by using photoelasticity.

2.3 Temperature

The temperature of the test specimen is measured during the curing process by using thermocouples. The thermocouples are placed in the uncured epoxy, and remain there until the end of the process. Thermocouples, however, cannot determine the temperature throughout the test specimen. Hence, experiments are made with multiple thermocouples, at different positions, in a single test specimen.

2.4 Applied methods

In this section, it is summarised, which of the methods discussed above, are applied in the project.

The aim is to identify the gel point, thermal expansion, chemical shrinkage as well as the overall stress field by in-situ DIC measurements of the process. The viscoelastic behaviour and the stress field should be determined by in-situ and subsequent photoelastic measurements, which is combined with removal of the metallic insert. At every experiment, the temperature is measured by using thermocouples.

2.5 Preparation of test specimen

In this section, it is described how the test specimen is prepared for the experiments. However, only the part which is common for the DIC and photoelastic measurements is considered. The parts with are specific for the experimental methods are described in chapter 3 and 4, respectively.

As presented in section 1.2, the mould for the test specimen should be very compliant, by which the boundaries can be considered as free. Hence, a mould is made of silicone rubber, which has a low stiffness. Furthermore, the mould is made with a material thickness of 2 mm, which is considered to make it compliant. A sketch of the cross section, with dimensions, are given in figure 2.1.

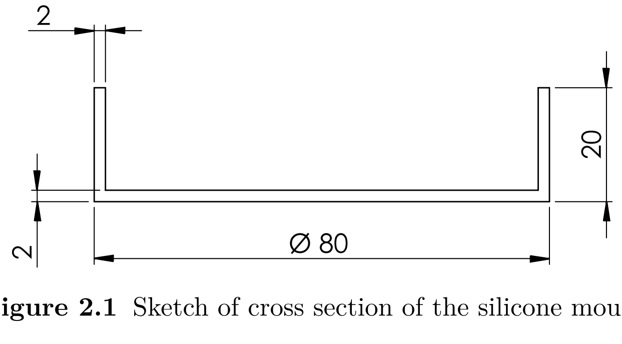

Figure 2.1 Sketch of cross section of the silicone mould

The silicone mould is cast in an aluminium mould. The technical drawings of the aluminium mould is given in appendix H. The silicone rubber used for the mould is Elastosil M4511 with Catalyst T21 from Wacker Silicones. Young's modulus of the material is not given by the product data sheet. However, Young's modulus is estimated to roughly 0.6 MPa [1] from the

---

[1] Young's modulus is estimated as the tensile strength divided by the elongation at break. Hence, the average Young's modulus is obtained. However, the material is presumed to have a non-linear stress strain relation, by which the estimated Young's modulus might be inaccurate at low strains.

tensile strength of 3.5 MPa and the elongation at break of 600 % [Wacker Silicones, 2013]. This is less than 0.02 % of the fully cured epoxy at room temperature. Hence, the stiffness of the mould is considered to be negligible, even for partially cured epoxy at elevated temperature.

To limit shear loads between the silicone mould, and the base underneath, the mould is placed on a base of poppy seeds which serve as roller bearings. This is assessed to allow the mould to deform more freely.

The epoxy system used for the test specimen is ”Epikote Resin MGS RIM 035” and ”Epikure Curing Agent MGS RIMH 038”, because it is available in the laboratory. Furthermore, experimental data of the material properties is available, which is used to model the system in part II of the report.

The insert is made of steel, because it has high Young’s modulus, and because the thermal expansion is low compared to e.g. aluminium. The coefficient of thermal expansion of carbon steel is 11.7 $\frac{\mathrm{\mu m}}{\mathrm{mK}}$, wheras it is 23.1 $\frac{\mathrm{\mu m}}{\mathrm{mK}}$ for aluminium. [Andersen et al., 2007]

The insert is a solid cylinder with a diameter of 12 mm. The height of the insert is approximately 6 mm. As the epoxy is poured approximately to the height of the insert, this also defines the thickness of the test specimen.

By making the test specimen thinner, it would be more accurate to assume a state of plane stress. However, as photoelasticity is used to measure the stress field, it is advantageous to have a thick test specimen, because, as described later in the report, the number of optical fringes is proportional to the thickness of test specimen. Hence, a thicker test specimen yields more data points, and hence increases the accuracy of the measurements. Furthermore, a thin test specimen would have a lower stiffness, and hence increase the influence of the mould stiffness. The thickness of 6 mm is assessed to be a fair compromise, even though it might violate the assumption of plane stress near the insert.

When the mould is made, an insert is prepared and positioned approximately at the centre of the mould, by rough measurements using a ruler.

The two components of the epoxy system are mixed carefully in the right mixing ratio, as stated in the product data sheet [HEXION, 2008]. The mixed epoxy is degassed in a vacuum to reduce air bobbles in the final test specimen.

Afterwards, the mixed epoxy is poured into the silicone mould with a steel insert. The test specimen is then placed in a vacuum again, to remove air bobbles formed due to the pouring of the epoxy[2]. Even small air bobbles will cause large imperfections in the test specimen, because the air expands when the temperature is increased. When the test specimen is ready, it is put in an oven for curing.

In figure 2.2, a test specimen in the silicone mould is shown.

---

[2] Some of the silicone moulds has imperfections at the surface due air bubbles. By placing the test specimen in a vacuum, these are filled with epoxy.

Figure 2.2 Test specimen with steel insert in a silicone mould.

When the silicone mould with the uncured test specimen is placed in the oven, a temperature sensor is placed inside the test specimen, and another near the test specimen, in the free air of the oven. The position of the temperature sensor inside the test specimen is not very consistent in the different experiments. However, as shown in appendix A, there is a significant temperature variation through the thickness of the test specimen.

The type of the used temperature sensors is K-thermocouples. The voltage from the thermocouples is amplified by an AD595 thermocouple amplifier [Analog Devices, 1999], from which the signal is acquired by using a National Instrument USB-6009 data acquisition (DAQ) module. The temperature is sampled at 10 Hz, after which the value is averaged over 50 samples to reduce noise. The program used for data acquisition, known as a Virtual Instrument (VI), is appended on the appendix CD, appendix I. The temperature measurement is limited to values above approximately 34 °C, which is due to the power supply of the AD595 amplifier.

Digital image correlation 3

Digital image correlation (DIC) is used to make in-situ deformation measurements of the test specimen during the cure. Hence, DIC is used on the test specimen, while it is in the oven. To do this, an oven is placed with the opening upwards, as seen in figure 3.1. The door of the oven has been replaced with a transparent lid of acrylic glass to allow the DIC measurements.

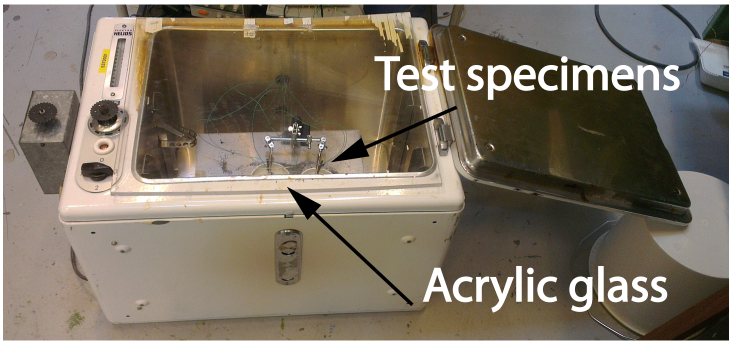

Figure 3.1 Oven with a lid of acrylic glass, which is used for DIC measurements.

The 2D setup, with a single camera, is simpler to use, as it does not require calibration. However, it must be ensured that the test specimen is normal to the camera, and that there is no out-of-plane displacement.

The 3D setup requires calibration. This makes it more arduous to use, and makes it more sensitive to disturbances in the setup. Furthermore, it requires good lighting conditions for both cameras. However, by using two cameras, the out-of-plane displacement can be measured, which eliminates that as a source of error.

In this project it is decided to use the 3D setup. Because of the variation of temperature during the experiment, thermal expansion of the entire setup could cause out-of-plane displacement of the test specimen. Furthermore, the epoxy resin has a considerable thermal and chemical strain during the process. This causes a volume change, which also causes out-of-plane displacement.

3.1 Surface pattern

The DIC system measures the deformation by identifying and tracking unique patterns on the surface of the test specimen. Hence, it is required that the test specimen has a stochastic pattern with distinct contrast difference on the surface. Usually this pattern is obtained by using two different colours of spray paint, however, that approach is not feasible on the uncured epoxy resin used in this project. Several methods have been attempted to obtain a good surface pattern, as described in appendix B.

It is discovered that a suitable pattern can be obtained by sprinkling expanded perlite on the surface, which is applied a speckle of black spray paint. However, before the pattern is applied to the surface, the epoxy resin in the mould must be preheated. Otherwise, the surface pattern tends to be ruined by what is assessed to be convection in the uncured epoxy. It has yielded successful results by preheating to approximately 60 °C before applying the surface pattern. The surface pattern which is used for the DIC measurements are shown in figure 3.2.

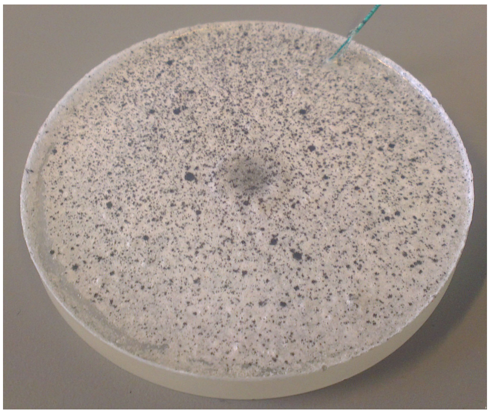

Figure 3.2 Stochastic surface pattern with expanded perlite, applied a speckle of black spray paint.

The surface pattern, with expanded perlite and spray paint, has a suitable pattern. However, the expanded perlite might affect the stiffness of the test specimen, which would affect the result. Yet, the surface pattern is used, as there is no better alternative. Furthermore, it might cause inaccuracies, that the displacements are measured on the surface only. Because the test specimen has a thickness of approximately 6 mm, the strain might vary through the thickness. However, it is assumed that the surface strain is a representative measure of the strain through the thickness of the test specimen.

3.2 Experiment

The oven in figure 3.1 is used for the experiment. The analogue dial is set for approximately 100 °C, after which the oven is allowed to preheat.

The temperature of the oven and the test specimen, during the experiment is shown in figure 3.3. The temperature sensor in the test specimen is approximately 11 mm from the edge, near the bottom side of the test specimen.

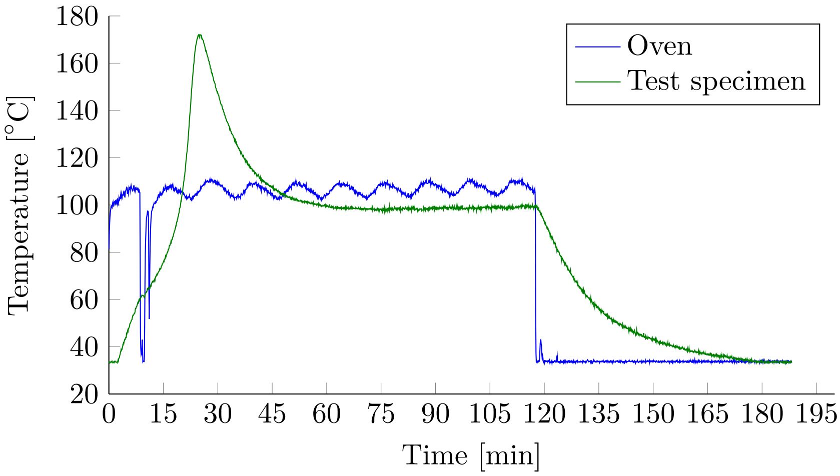

Figure 3.3 Temperature in the oven and test specimen during the DIC measurement.

The epoxy resin of the test specimen reaches a temperature of 60 °C after approximately 8 min and 30 s. At this time, the lid is removed from the oven, and the surface pattern is applied. This is seen in figure 3.3 as a significant drop in temperature in the oven.

Approximately 12 min into the experiment, the oven is closed with the lid, the DIC system is set up, and the image capturing is started. The setup is seen in figure 3.4, where two cameras[1] are in position above the oven with the test specimen. To synchronise the time scales of the temperature measurements, and the DIC measurements, the time of the first image capture w.r.t. to the temperature measurement is noted.

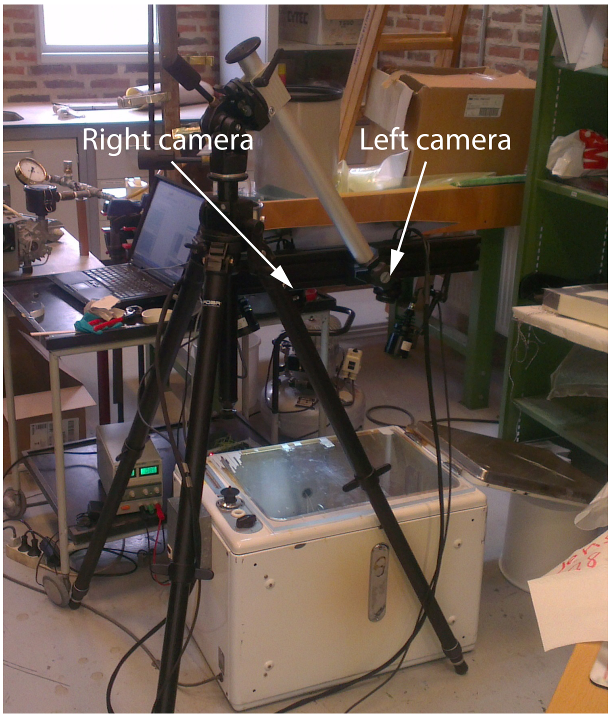

Figure 3.4 Test setup with DIC system in position above the oven.

During the first approximately 25 min, the temperature of the test specimen increase. The temperature of the test specimen reaches a temperature of more than 170 °C, which is considerably more than the temperature of the oven. This is due to the exothermic chemical reaction of the curing process. Afterwards, the chemical reaction ease off and the temperature decrease to a steady-state temperature. The steady-state temperature of the test specimen is lower than the oven temperature. This is assessed to be due to the location of the temperature sensor in the oven.

After approximately 117 min and 30 s, the oven is turned off, and the lid is removed. This causes the temperature of the oven to drop rapidly, as seen in figure 3.3.

In figure 3.5 and 3.6, the first image from the left and right camera are shown. The results from the DIC measurements are given according to a global x-y-z coordinate system. The coordinate system is presumed to be determined through the calibration procedure. Because the two cameras are angled w.r.t. each other, neither of the images are aligned with the global coordinate system. However, the x*-y* coordinate systems in the figures are assessed to resemble the global x-y coordinate system approximately. Note that the x*-y* coordinate systems in the two images are not the same coordinate system.

---

[1] 4M cameras (4 mega pixels) with 2.8/50 mm lenses, family C

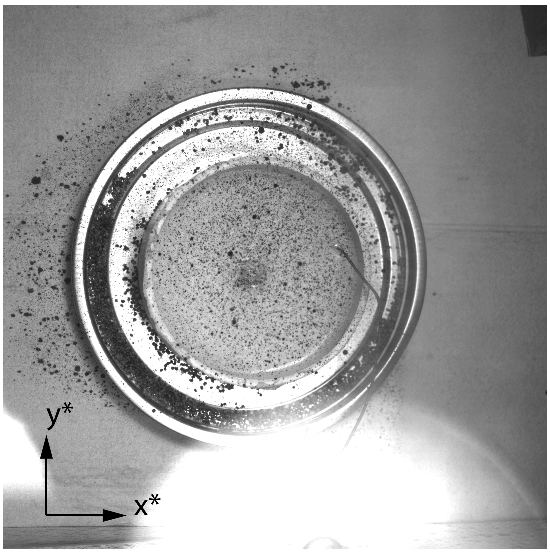

Figure 3.5 Image from left camera of DIC system

Figure 3.6 Image from right camera of DIC system

The DIC system is calibrated by using a CP20 175x140 calibration object. This yields a measuring area with length and width between 110 and 155 mm. [GOM mbH, 2007] The measuring area is larger than the test specimen. This results in lower resolution of the measured data. However, the measuring area is determined by the calibration object. The calibration object, which is used, has been chosen as the best compromise of the available calibration objects.

Images like figure 3.5 and 3.6 are captured by the DIC system for every 10 s. However, no images were captured in the interval from 46 min and 51 s to 78 min and 59 s, because the DIC system crashed. This happened again from 132 min and 39 s to 133 min and 58 s.

3.3 Results

The captured images are processed by the GOM ARAMIS-v6.2.0-6 software. The facet size is set to 30x30 pixels, which is approximately 3x3 mm, as this yields reasonable data. A smaller facet size induces more noise, whereas a larger facet size reduces the resolution of the result. Yet, the strain field which is obtained by the measurements cannot be used to study the local stress field near the insert. This is seen in figure 3.7, where the strain field is shown from the last images, at 187 min and 48 s after the start, w.r.t. the global x-y coordinate system. The strain is calculated from the deformation w.r.t. the deformation state, when the first set of images is captured. As seen, there is no evident strain gradient around the insert in the centre.

According to Hamilton [2011], ”very rough surfaces are problematic”. Hence, the poor result from the DIC measurements is assessed to be because of the surface of the test specimen. The expanded perlite on the surface causes a rough texture. A few air bubbles has been trapped below the expanded perlite and has caused bulges in the surface. Furthermore, there is a bulge in the surface around the steel insert. This is assessed to be due to deformations in the surface, before gelation of the epoxy.

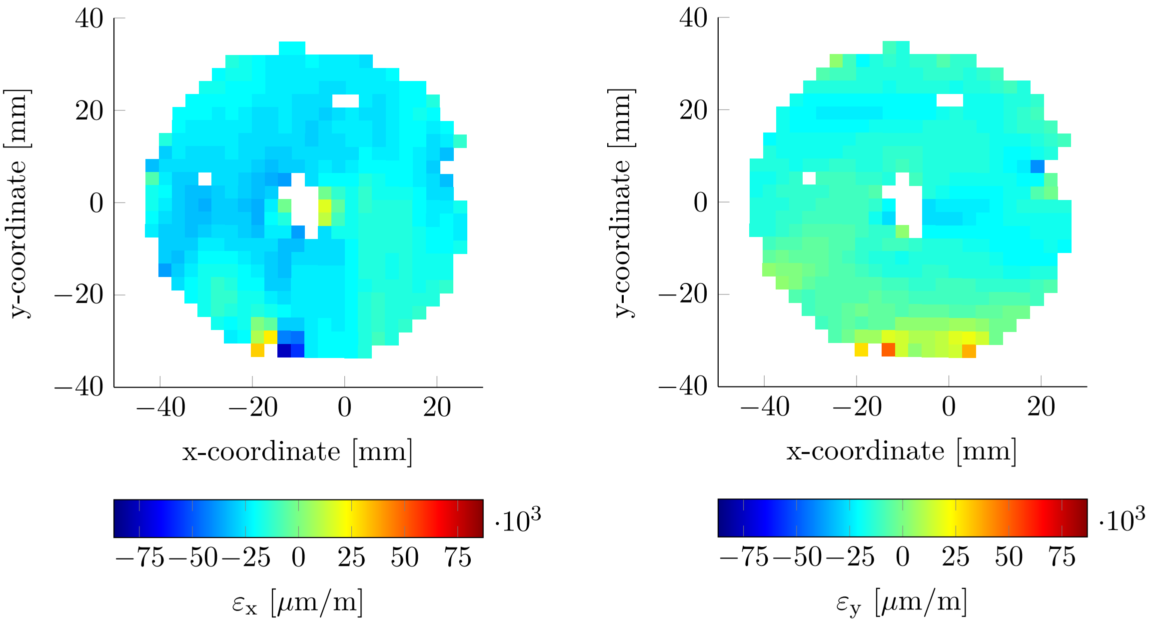

Figure 3.7 Strain field from DIC measurement at 187 min and 48 s

3.3.1 Average strain

Even though the strain gradient is not evident, the data can be used to evaluate the thermal and chemical strain of the epoxy, due to thermal expansion and chemical shrinkage. For every time step, the average value of strain throughout the test specimen is calculated. This is assumed to resemble the sum of thermal and chemical strain. To reduce the uncertainty due to noise and the effect of the steel insert, the upper and lower 10 % of the dataset is removed. This yields the plot which is shown in figure 3.8. To show, that nothing important is lost when the upper and lower 10 % of the dataset is removed, the raw average strain is given as well.

The temperature graph from figure 3.4 is shown in the figure as well. The temperature data is normalised to fit the range this plot, and is thus presented without a scale.

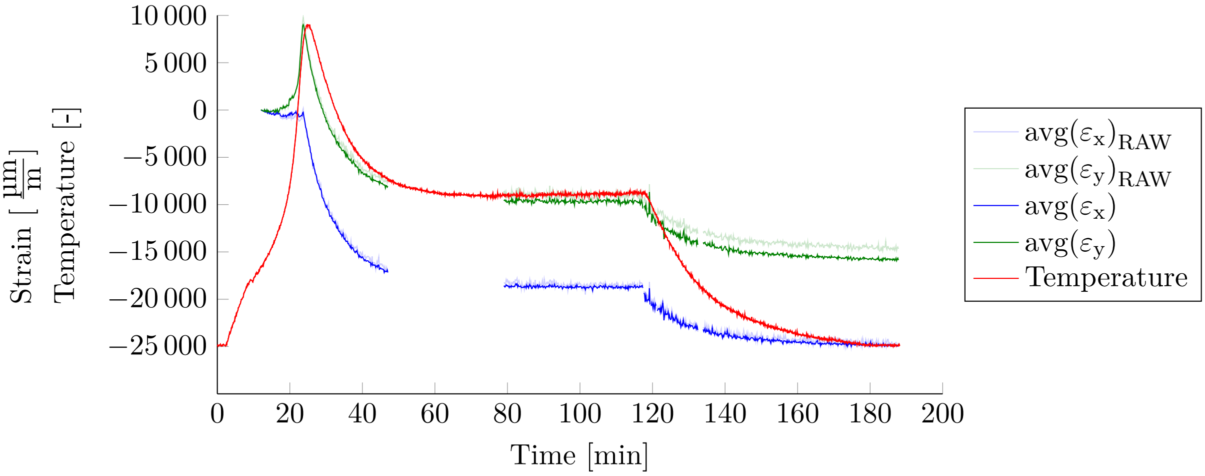

Figure 3.8 Average strain throughout the surface of test specimen, as a function of time.

In figure 3.8 it is seen, that there at first sight is an overall agreement between the strain data and the temperature data. When the temperature increases, the strain increases as well, and vice versa. However, when the figure is examined closer, a disagreement is evident.

Furthermore, the average strain in the x and y direction appear to have an offset. This does not correlate with the expected result, as the thermal expansion and chemical shrinkage is expected to be isotropic, and the geometry is symmetric.

These disagreements are discussed in the following.

Offset in strain

The offset between the average strain in the x and y direction is assessed to be due to an anisotropic strain in the test specimen, before the gel point is reached.

As seen in figure 3.8, a large strain increase is apparent in the y-direction at the start of the process, whereas there is almost no strain in the x-direction. This difference is assessed to cause an offset in the remaining time of the process.

The large strain in the y-direction is assessed to be due to thermal expansion of the silicone mould. Hence, the strain should also be present in the x-direction. However, the surface of expanded perlite does not follow the deformation in the x-direction, because a crack in the surface pattern appears. The crack appears at the left side of the test specimen. This is seen in figure 3.9 and 3.10, where a section of the images from the left camera is shown at the beginning, and 15 min into the DIC measurements.

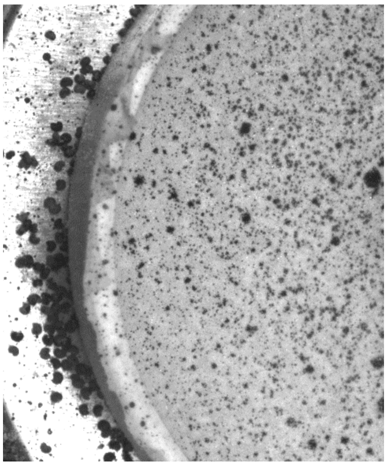

Figure 3.9 Section of the first image of the DIC measurement, from the left camera

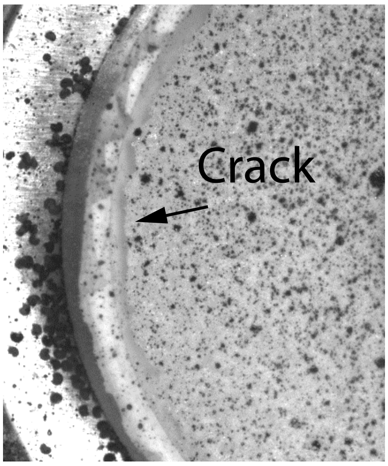

Figure 3.10 Section of image of the DIC measurement, from the left camera, 15 min into the measurement. A crack is apparent in the surface pattern, near the edge of the silicone mould

The surface pattern appears as a skin, on top of the viscous epoxy. When the crack appears, the left part of the surface pattern disengages from the silicone mould. The remaining circumference of the surface pattern is still attached to the silicone mould, and thus follows its deformation.

To compensate for this offset between the average strain in x and y, the strain is calculated w.r.t. the last images. Again the average strain is calculated, and plotted as seen in figure 3.11. This removes the offset between the two strain plots, which are almost equal in most of the time range. The deviation at the first time range is assessed to be because the surface pattern does not follow the deformation of the epoxy resin.

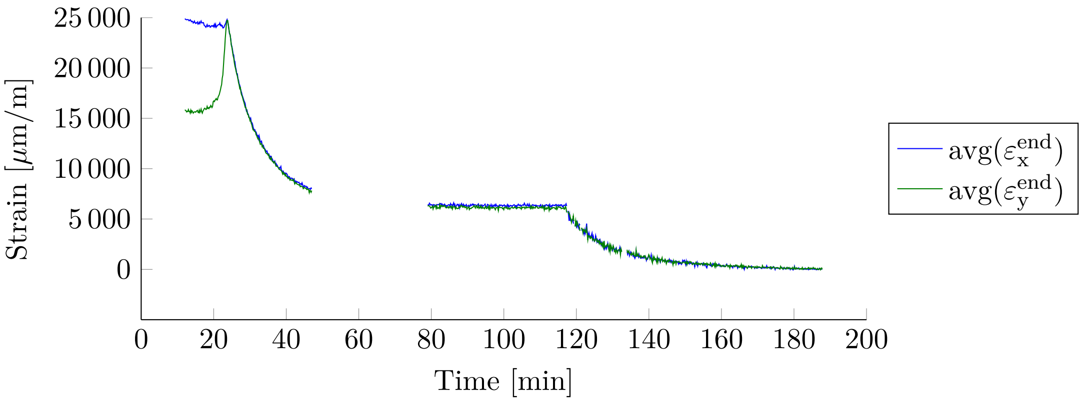

Figure 3.11 Average strain throughout the surface of test specimen, as a function of time, calculated w.r.t. the deformation at the end of the process.

Temperature-strain disagreement

It is seen in figure 3.8, that there is a disagreement between the temperature and strain measurements. E.g. the two dataset does not peak at the same time. The maximum value of avg(ε_x) is at approximately 23 min and 40 s, whereas the maximum temperature measurement is at 24 min and 50 s.

Similarly it is seen, at approximately 120 min, when the oven is turned off, that the strain starts decreasing before the temperature measurement. This difference is enhanced in figure 3.12, where the temperature and average strain measurements are shown for the time range where the oven is turned off. To make comparison possible, the data is normalised.

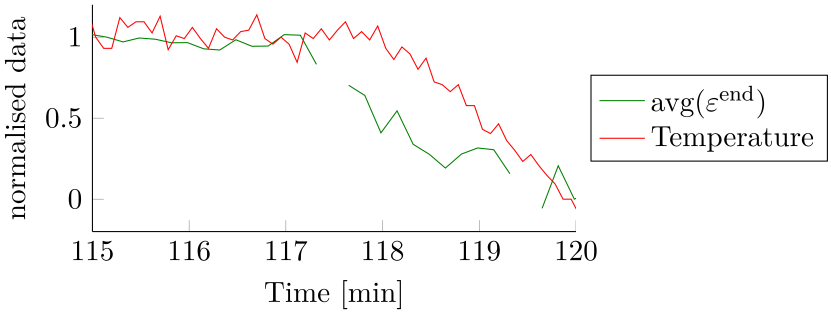

Figure 3.12 Normalised plot of average strain and temperature, when the oven is turned off

Again, it is seen, that there is an offset of approximately 1 min. The average strain starts descending before the temperature measurement.

A possible explanation could be, that the temperature and strain measurements has not been synchronised correctly. However, this is not assessed to be the case. It is rather considered to be due to a temperature variation through the thickness of the test specimen. As the strain is measured at the top of the test specimen, and the thermocouple is at the bottom, this causes a deviation.

When the oven is turned off, the temperature starts descending. This causes the temperature of the test specimen to descend as well, however, due the thickness of the test specimen, the top side will cool faster than the bottom.

This is further confirmed by the experiment with three thermocouples through the thickness, which is described in appendix A. The measurements of the experiment shows that the temperature in the top of the test specimen peaks before the bottom. It is furthermore seen, that the top cools faster than the bottom, when the oven is turned off.

3.3.2 Gel point

The data of the DIC measurements are analysed to identify the gel point. As described in section 1.3, the gel point is the point at which the epoxy transforms from the viscous phase to the rubber phase. Hence, it is presumed that the surface pattern follows the deformation of the test specimen, after the gel point.

It is suggested by Peiris [2008], that the standard deviation of the DIC measurements can be used to identify the gel point. The gel point might be evident from the standard deviation of the strain field for two reasons.

One reason is the Brownian motion. When the epoxy resin is in the viscous phase, Brownian motion is considered to cause a random movement in the test specimen. When gelation occurs, this motion might be limited due to cross-linking in the polymer. However, because the deformation is measured by using DIC, the measurements are averaged over the area of a facet, which is approximately 3x3 mm. Furthermore, as discussed before, the surface pattern appear as a skin on top to the viscous epoxy. This is considered to limit the Brownian motion in the surface.

The other reason why the standard deviation of the strain field might be useful to detect the gel point is, that residual stress builds up, after gelation. Before gelation, the epoxy is viscous. Hence, a stress concentration around the insert is not expected, and thus neither a strain concentration. The volumetric strain is rather considered to cause a strain in the thickness of the test specimen. After gelation, a strain concentration is expected to appear. Even though it is not evident in the strain field of figure 3.7, it might be evident in the standard deviation.

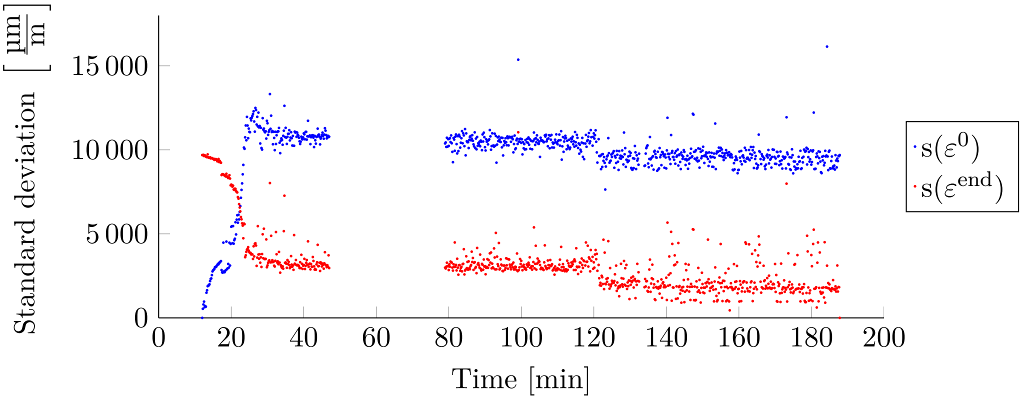

Figure 3.13 Standard deviation of strain as a function of time.

The standard deviation is calculated from a dataset of both ε_x and ε_y at each time step. As shown in section 3.3.1, there is considerable difference between strains which are calculated with respect to the initial deformation state (ε^0) and the final deformation state (ε^{end}). Hence, the standard deviation is calculated from both datasets, as shown in figure 3.13.

From the figure, it is evident that standard deviation changes significantly from approximately 20 to 25 min after the start of the experiment. This might be used to detect the gel point.

However, it appears as the standard deviation in figure 3.13 is affected by temperature variations. At approximately 120 min, there is a drop in the standard deviation. This is assessed to be caused by a temperature change, and thus thermal expansion of the test specimen. In figure 3.3 and 3.11 it is seen, that both temperature and strain decreases at the same time as the standard deviation. This is assessed to be due to the strain gradient around the insert, which affects the standard deviation.

Hence, it is not unambiguous whether the change in standard deviation between 20 and 25 min is due to gelation or due to the temperature change which is evident in figure 3.3. Because of the temperature dependency, it is assessed that the standard deviation of the strain measurements is not a good measure for the gel point, in this case.

Another approach is to consider the difference between the values of avg(ε_x) and avg(ε_y). Because the test specimen is symmetric, the average strain in the x and y direction is expected to be equal. However, as shown in section 3.3.1, they are not. It is considered, that the asymmetric strain occur before the gel point, hence the difference between avg(ε_x) and avg(ε_y) might be used to detect the gel point. The difference is calculated for both ε^0 and ε^{end}, as seen in figure 3.14

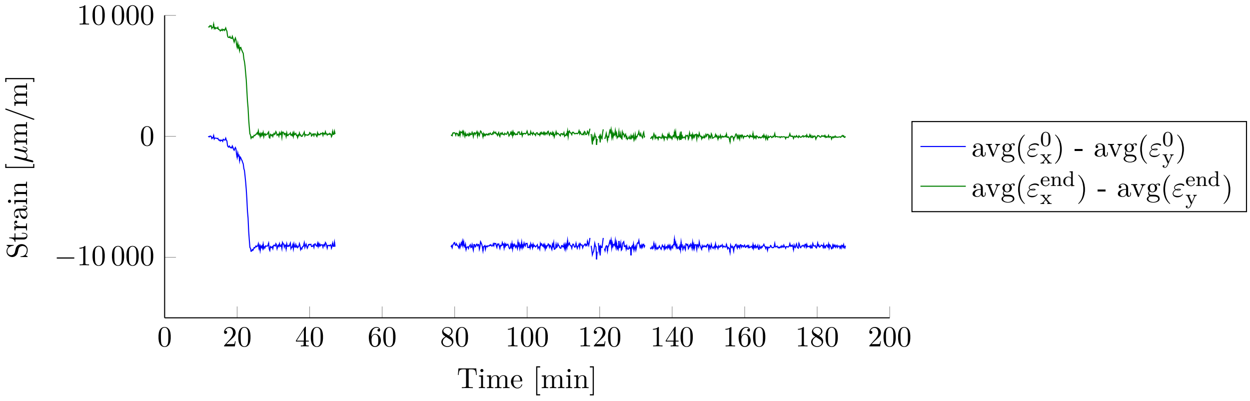

Figure 3.14 Difference between average strain in x- and y-direction, which indicates the gel point.

It is seen in the figure, that both graphs becomes nearly constant at the same time, at 23 min and 31 s. This is considered to be the gel point.

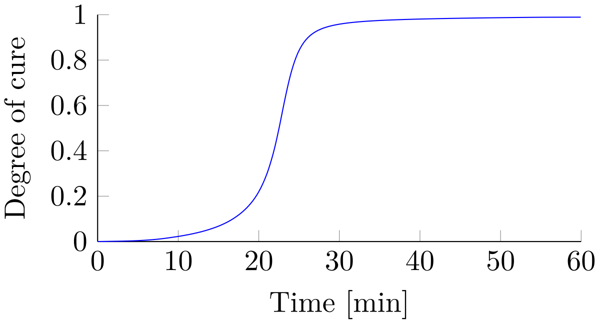

Figure 3.15 Degree of cure, calculated by model described in section 5.2

The gel point, identified from the experiment is compared with the model of the cure kinetics, which is described in section 5.2. By using the model, presented by Jakobsen et al. [2013a], the degree of cure is calculated, based on the temperature shown in figure 3.3. In figure 3.15, the degree of cure is plotted as a function of time.

At 23 min and 31 s, the gel point obtained from figure 3.14, the degree of cure is 0.67. According to Jakobsen et al. [2013b], the gel point occurs when the degree of cure is 0.61. The graph in figure 3.15 crosses 0.61 at 23 min and 8 s, only 23 s before the gel point determined from figure 3.14.

It is hereby proposed, that the difference between the average strains in the x- and y-direction is a good measure for the gel point for this case. If the test specimen was not symmetric, it might not be suitable to use the same approach, as there might be differences between ε_x and ε_y due to the geometry.

3.3.3 Thermal expansion and chemical shrinkage

In this section, the strain data is analysed to evaluate the coefficient of thermal expansion (CTE) and the chemical shrinkage during the cure. It is assumed, that the average of the two graphs in figure 3.11 yields the sum of thermal and chemical strain.

In figure 3.16, the experimental data of the average strain (average of the two graphs in figure 3.11) is plotted as a function of temperature. In the figure, various points of interest are marked as well.

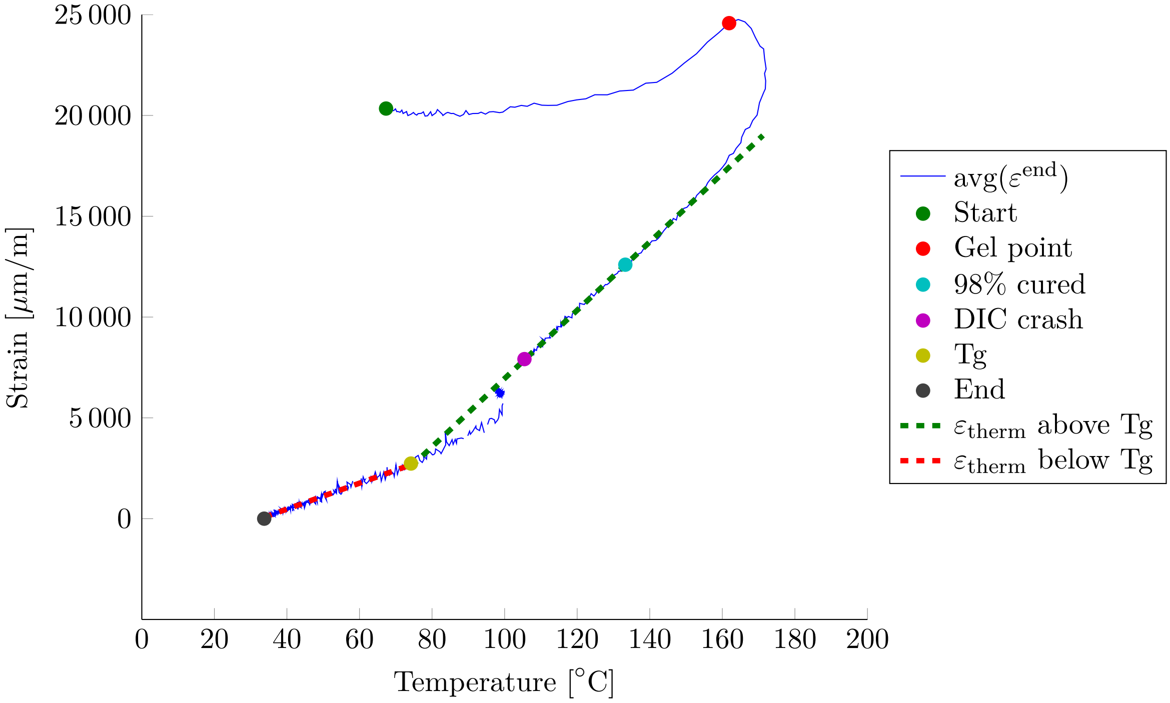

Figure 3.16 Average strain from DIC measurements as a function of time, various points of interest, and linear functions of thermal strain.

The start point is at 12 min and 1 s, when the first set of images is captured. The gel point is at 23 min and 31 s, as described in section 3.3.2. The point "98% cured" marks the point at which figure 3.15 predicts the degree of cure to be 0.98, at 33 min and 11 s. "DIC crash" is the point, at which the DIC system crashed, at 46 min and 51 s. Hence, there is a lack of data after this point. T_g is the point, at which the temperature goes below the glass transition temperature, predicted by the model in equation (5.40), which is presented later in this report. This occur at 126 min and 9 s. End marks the final image capture of the DIC measurement, at 187 min and 48 s.

It is assumed, that the thermal expansion is related to the temperature by a bi-linear relation. Hence, a value of CTE is determined for temperatures above T_g and another for temperatures below.

The average strain, from the time the degree of cure reaches 0.98 to the time where the DIC system crashes is used to calculate CTE above T_g. The point at which the epoxy is fully cured has not been used, because it is too close to "DIC crash". By fitting a linear function to the data, the slope, and thus CTE, is determined to 169 $\frac{\mu\text{m}}{\text{m}^\circ\text{C}}$. In the same way, the data after the temperature goes below T_g, has been used to calculate CTE below T_g to 64.3 $\frac{\mu\text{m}}{\text{m}^\circ\text{C}}$.

The linear functions of thermal strain, used to determine the values of CTE is plotted in figure 3.16 as dashed lines. The function for ε_{therm} above T_g is extrapolated both up and down in temperature. As seen, it cross the strain at T_g very accurate.

Between T_g and "DIC crash" however, there is a deviation. This is assessed to be due to temperature variation through the thickness of the test specimen, as discussed in section 3.3.1. In figure 3.16, this is seen as a nearly vertical decrease of average strain, at a constant temperature of approximately 100 °C.

In the other end of figure 3.16, at high temperature and strain, this effect is present as well. However, the linear thermal strain is assumed to deviate due to chemical shrinkage too. Hence, the chemical shrinkage is considered in the following.

In figure 3.17, the total average strain is plotted together with the thermal strain, as a function of degree of cure.[2]

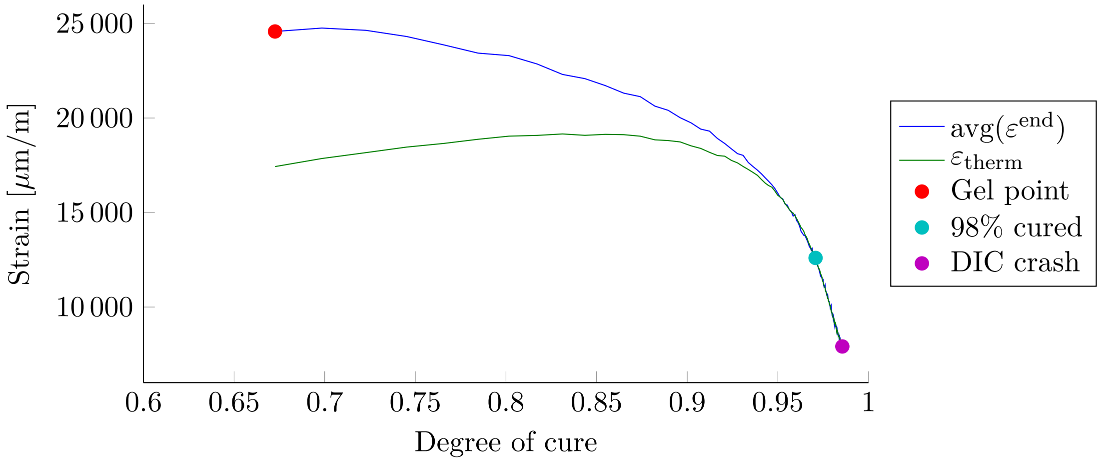

Figure 3.17 Total average strain and thermal strain as a function of degree of cure

The difference between the two graphs is considered to be the chemical strain. The chemical strain is shown in figure 3.18.

---

[2] The thermal strain is evaluated at each data point of the DIC measurement in figure 3.16. Each of these data points is related to a time stamp from the measurement, which is used to obtain the degree of cure from figure 3.15.

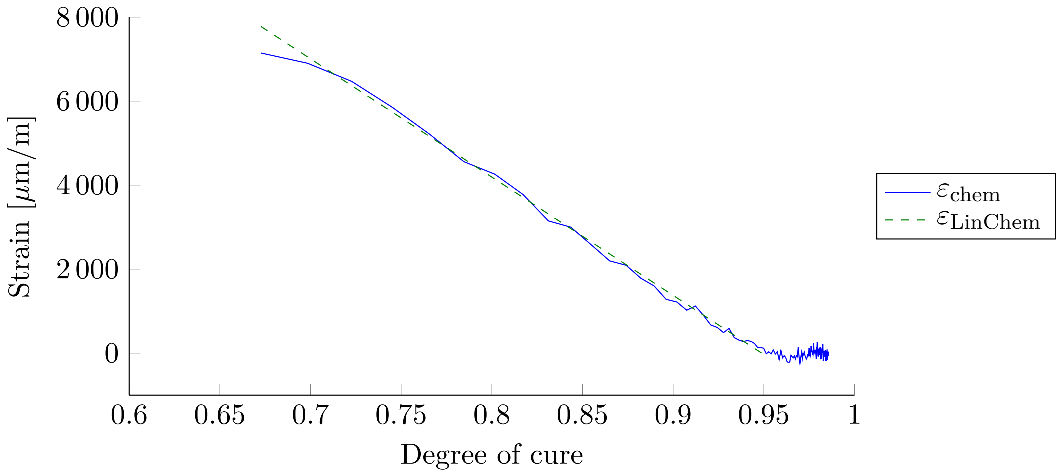

Figure 3.18 Chemical strain as a function of degree of cure

The chemical strain is assumed to be linearly related to the degree of cure. Hence, a linear fit is shown in the figure. The linear graph is fitted to the middle section of the data, where chemical strain appears linear. However there is some non-linearity at the ends. This is assumed to be due to temperature difference between the top and bottom of the test specimen. Another reason could be, that surface pattern affect the result. The addition of expanded perlite to the surface might change the stiffness and the thermal expansion. When the stiffness of the epoxy is low, this might have a significant effect.

However, inaccuracies in the model of the curing kinetics, i.a. caused by the temperature variation through the thickness, might cause deviation too. When the model predict 95 % of conversion, the graph in figure 3.18 appear to level off, which is assessed to indicate completion of the chemical process.

From the data in the linear section, a linear model is fitted. The slope is -28 162 $\frac{\mu\text{m}}{\text{m}}$. The total chemical strain, read from the non-linear curve, is 7 147 $\frac{\mu\text{m}}{\text{m}}$.

3.4 Summary

In this chapter, in-situ DIC measurements are performed, and the results are analysed to determine the gel point, the average strain, the thermal strain, and the chemical strain.

The results are shown in table 3.1, together with results obtained by Jakobsen et al. [2013a].

	DIC measurement	Jakobsen et al. [2013a]	Deviation
Gel point, c_{gel}	0.67	0.61	10.3 %
Gel time, t_{gel}	23 min and 31 s	23 min and 8 s	1.63 %
CTE below T_g, α_{bT_g}	64.3 $\frac{\mu\text{m}}{\text{m}^\circ\text{C}}$	76 $\frac{\mu\text{m}}{\text{m}^\circ\text{C}}$	-15.4 %
CTE above T_g, α_{aT_g}	169 $\frac{\mu\text{m}}{\text{m}^\circ\text{C}}$	175 $\frac{\mu\text{m}}{\text{m}^\circ\text{C}}$	-3.23 %
ε_{chem} after gelation	-7 147 $\frac{\mu\text{m}}{\text{m}}$	-5 000 $\frac{\mu\text{m}}{\text{m}}$	42.9 %
$\frac{\text{d}\varepsilon_{chem}}{\text{dC}}$	-28 162 $\frac{\mu\text{m}}{\text{m}}$	-14 229 $\frac{\mu\text{m}}{\text{m}}$ [3]	97.9 %

Table 3.1 Summary of results from DIC, compared with results obtained by Jakobsen et al. [2013a].

---

[3] [Jakobsen et al., 2013c]

It is assessed, that the values of the chemical strain, the gel point, and the gel time are highly dependent on the accuracy of cure kinetic model. However, it is beyond the scope of the project, to evaluate the accuracy the curing kinetics model.

The values of the thermal strain are affected by the fact, that the strains are measured at the top surface, and the temperature is measured near the bottom. It is noted, that thermal strains are smaller, and the chemical strains are larger, compared to the results obtained by Jakobsen et al. [2013a]. This indicates uncertainty in the separation of thermal and chemical strains.

Furthermore, the DIC and temperature measurements induce uncertainties. As seen in figure 3.13, the standard deviation is up to 16 000 $\frac{\mu m}{m}$ at one point. However, the value of avg(ε^{end}) which is used to evaluate the thermal and chemical strain, the upper and lower 10 % of the data is disregarded. Hence, the maximum standard deviation, after gelation, is less than 1 500 $\frac{\mu m}{m}$. This value is calculated from the results of 778 facets. By assuming, that the strain measurements at these 778 facts follow a normal distribution, the accumulation law can be applied, to evaluate the standard deviation of the average strain. Equation (3.1) is a simplified version of the accumulation law. It yield a standard deviation of 52 $\frac{\mu m}{m}$ on the averaged strain.

$$s(avg(\varepsilon^{end})) = \frac{s(\varepsilon^{end})}{\sqrt{n_{samples}}} \tag{3.1}$$

where: [Mouritsen, 2009]

$s(avg(\varepsilon^{end}))$	Standard deviation of the average strain, [ ]
$s(\varepsilon^{end})$	Standard deviation of the sampled strain, [ ]
$n_{samples}$	Number of samples, [ ]

The uncertainty of the temperature measurement is considered as well. The thermocouple is generally assessed to yield an accurate measurement, however, some noise is apparent in the data. It is assumed, that the uncertainty due to noise can be determined by considering the measurement of the oven in figure 3.4, after 120 min. In this range the temperature is below the minimum temperature which is possible to measure with this set-up. Hence, the variation in the measurement is assumed to be a representative measure of the uncertainty. The standard deviation, calculated from this dataset is 0.26 °C.

It is assessed, that the deviation caused by the uncertainty of the DIC and temperature measurements are small, compared to the error induced by the fact that the temperature is measured at the bottom of the test specimen, and the strain is measured at the top. However, the effect of this error has not been quantified.

Photoelasticity 4

Photoelastic measurements are performed by using a polariscope, to obtain the stress field of the test specimen. The measurements are performed at both room temperature and elevated temperature. As seen in figure 4.1 and 4.2, an oven has been modified by making a window at the back side. Hence, it can be placed between the optical filters of the polariscope.

Figure 4.1 Image of the set-up, with an oven between the filters of the polariscope

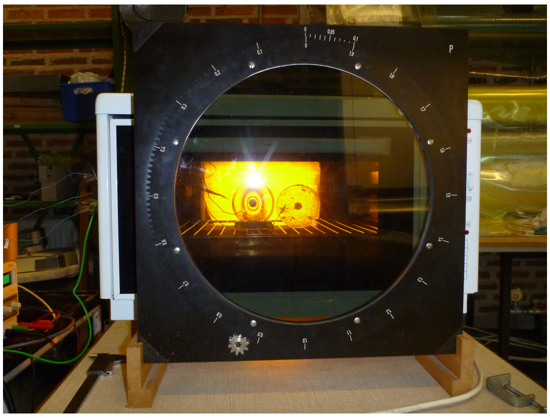

Figure 4.2 View of the test specimens, through the oven

4.1 Circular dark field polariscope

A polariscope can be configured by various combinations of polarisers and wave plates. In this project a setup known as a circular dark field polariscope, as shown in figure 4.3, is used.

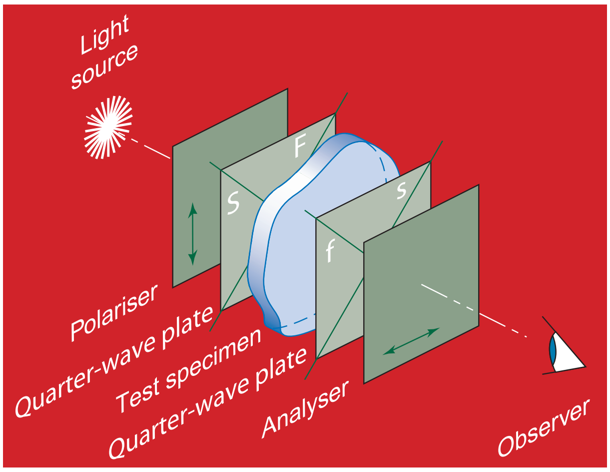

Figure 4.3 Circular dark field polariscope. Illustration from Phillips [1998], which has been modified.

It is beyond the scope of this project to describe the physics of the polariscope in details. In the following, a brief description is given based on Phillips [1998].

The light source in figure 4.3 can be chosen as either white or monochromatic light. In this project, monochromatic light is used. The light source emits light which, at first, travels through a polariser and a quarter-wave plate. This creates light, where the oscillation in one plane has a phase lag of one quarter of the wave length, compared to oscillations in a perpendicular plane. If the oscillations in the two planes are of equal amplitude, this special kind of light is known as circularly polarised light, because the resultant oscillation yield a circular motion. It is illustrated in figure 4.4.

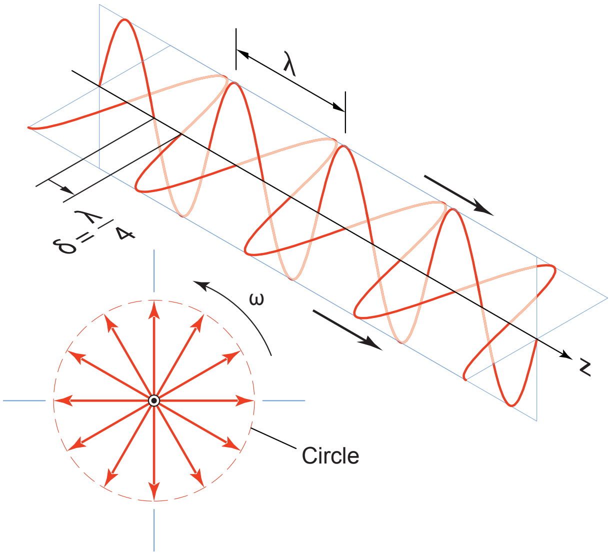

Figure 4.4 Circularly polarised light [Phillips, 1998]

If this light does not pass through the test specimen, the second quarter-wave plate and the analyser does not let any light through. Hence, the polariscope appear dark to the observer.

When the light passes through the test specimen, the speed of light is decreased by a factor reciprocal to the index of refraction. If the in-plane stress field of the test specimen is isotropic, the index of refraction is isotropic too. This causes the waves of light in both planes of figure 4.4 to slow down. When the light leaves the test specimen, it is said to be retarded. However, as the light is retarded in both planes, the relative retardation is zero. Hence, when the light leaves the test specimen, the light is still circularly polarised light, by which no light passes through the second quarter-wave plate and the analyser.

If the in-plane stress field of the test specimen is anisotropic, the index of refraction is anisotropic too. This causes the light waves to propagate with different velocities in the planes normal to the directions of the two principal stresses. Hence, the phase lag between the waves in the two planes of figure 4.4 is changed, by which there is a relative retardation. The relative retardation turns out to be proportional to the principal stress difference in the plane of the test specimen.

If the relative retardation is a multiple of the wave length of the light, the resultant light is still circularly polarised light, which cannot pass through the second quarter-wave plate and the analyser. However, if the relative retardation is not a multiple of the wave length, light passes through to the observer. This causes a fringe pattern as the one seen in figure 4.5.

Figure 4.5 Example of fringe pattern in a stressed test specimen.

When the relative retardation is a multiple of the wave length of the light, a dark fringe appear. The fringes are distinguished by the fringe order, which is the ratio between the relative retardation and the wave length. The fringe order is proportional to the principal stress difference as shown in equation (4.1), which is known as the stress-optical law.

$$\sigma_1 - \sigma_2 = \frac{N f_\sigma}{h} \tag{4.1}$$

where: [Dally and Riley, 1991]

σ_1	First principal stress, [Pa]
σ_2	Second principal stress, [Pa]
N	Fringe order, [ ]
f_σ	Fringe constant, $\left[\frac{\mathrm{N}}{\mathrm{m}}\right]$
h	Height of plane specimen, [m]

The fringe constant, f_σ, is a material constant, which is determined in appendix C for the specific epoxy used in this project. The value which is used throughout this project is $f_\sigma = 18\,616\ \frac{\mathrm{N}}{\mathrm{m}}$.

4.2 Time and temperature dependency

The usual application of photoelasticity is to analyse the stress field of a complex linearly elastic mechanical problem, where the analytical method is cumbersome or impossible. [Doyle and Phillips, 1989] The approach is to make a physical model of the mechanical structure from a photoelastic material. The model is loaded in a polariscope, after which the stress field is determined by the fringes. The stress field of the model is then scaled to determine the stress field of the physical structure. In this case, the photoelastic model is expected to yield linear stress-strain and stress-fringe order relations [Dally and Riley, 1991].

In this project, however, the method is used in a very different application. The method is used to study stresses which are formed over a longer time frame, while the material cures, and while the temperature varies.

The fringe constant, f_σ, is known to change with the temperature. In figure 4.6, a typical relation between f_σ and the temperature is shown for a commonly used epoxy. [Dally and Riley, 1991]

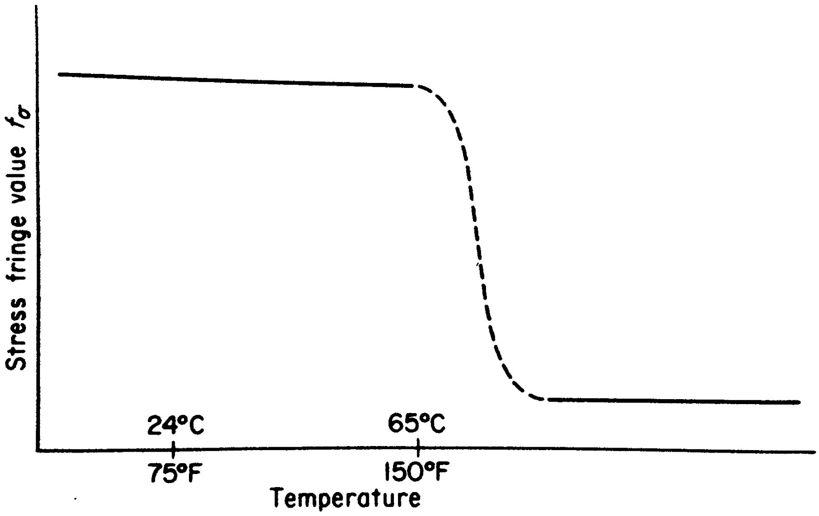

Figure 4.6 Typical cure for f_σ as a function of temperature [Dally and Riley, 1991]

As seen, f_σ decreases slightly with an increase in temperature, at low temperatures. Around the glass transition temperature, T_g, f_σ drops abrupt to a low value. [Burguete and Patterson, 1996]

Furthermore, most polymers has photoviscoelastic behaviour, where f_σ decrease with time, when a load is applied. [Dally and Riley, 1991] This is not a problem in the usual application of photoelasticity, as it is over a short time range, but it might have an effect in the experiments performed in this project.

At last, photoelastic materials exhibit a phenomenon called stress-freezing. If a model is loaded, when the temperature is above a T_g, and the model is cooled down before the load is removed, the fringes will remain in the model, even after the load is applied. [Dally and Riley, 1991] This is considered to be a problem in the experiments performed in this project, as the test specimen is cured above T_g. The residual stress contribution from the chemical strain occur above T_g, and the residual stress contribution from the thermal strain occur partly above T_g.

Generally, the optical behaviour, described in this section, is assessed to exhibit a stress-optical relation which resembles the stress-strain relation of a polymer. Takahashi et al. [1987], who has considered strain freezing and photoplaticity for a polycarbonate material, suggest that the fringe order is relate to the principal strain difference, rather than the principal stress difference. However, this is not considered further in this project.

4.3 Residual stress from insert removal

In this section, an experimental method is described where the residual stress is determined in a test specimen, at the end of the process, by removing the insert. It is furthermore tested whether the cooling rate affects the formation of residual stresses. At high temperature, the epoxy is expected to behave viscoelastic. Hence, the residual stress is expected to be relaxed, to some extent. As the viscoelastic effect is time dependent, it is hypothesized that the residual stress is dependent on the cooling rate.

Due to the effects, which is presented in section 4.2, it is not possible to evaluate the residual stress of a test specimen, by simply evaluating the fringes of the stressed test specimen in a polariscope. Hence, it is evaluated by insert removal. The difference in the fringe patterns, before and after the insert is removed, are considered to evaluate the residual stress.

4.3.1 Insert

To be able to remove the insert of the test specimen, it has been attempted to wind a piece of kapton foil around a cylindrical insert. To keep the kapton foil in place, a piece of tape is added. However, this experiment did not yield good results. This is assessed to be partly due to the softened interface between the insert and the epoxy, because of the foil and the tape. Especially the tape is considered to soften the interface, because the glue layer creep, which reduces the residual stress in the test specimen.

To avoid the kapton foil and the tape, while retaining the possibility of removing the insert, a conic insert is made. The insert is made with the dimensions given in figure 4.7. Before it is casted into the epoxy, it is coated in a release wax.

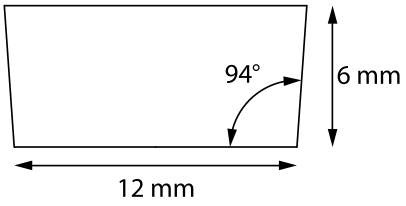

Figure 4.7 Sketch of the conic insert

This is considered to induce some inaccuracy to the result. The inclined edges of the insert might cause out of plane stress and strain.

4.3.2 Temperature and cooling

In figure 4.8, the temperature measurements are shown. The test specimen, which is quenched, has been cooled in water, whereas the other test specimen is left to cool slowly in the oven, after it is turned off.

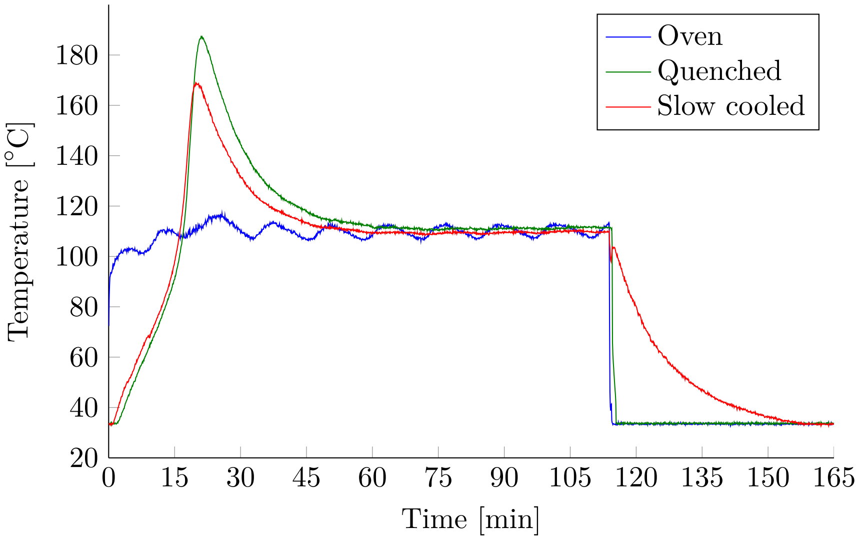

Figure 4.8 Temperature measurements of the test specimens with conic inserts.

There is a distinct difference in the temperature of the two test specimen, even though they are almost identical. The difference is assessed to be due to the position of the thermocouples. As shown in appendix A, the temperature varies through the thickness of the test specimens.

It is assumed primarily to be the cooling rate, before the temperature passes T_g, which influence the residual stress. From the data of figure 4.8, the cooling rate above T_g is approximately -5 $\frac{°\text{C}}{\text{min}}$ for the slowly cooled test specimen, and -270 $\frac{°\text{C}}{\text{min}}$ for the quenched test specimen.

After the test specimens are cooled, they are wet sanded on both sides to obtain an even thickness.

4.3.3 Photoelastic measurements

The test specimens are placed in the circular dark field polariscope. Both test specimen show several fringes. Images are captured before the inserts are removed. As the images are processed semi-manually, two images are captured each time. When the data is processed, the average of the two images is used as the result.

In figure 4.9 and 4.10, images of the fringes in the slowly cooled and quenched test specimens are shown, before the inserts are removed.

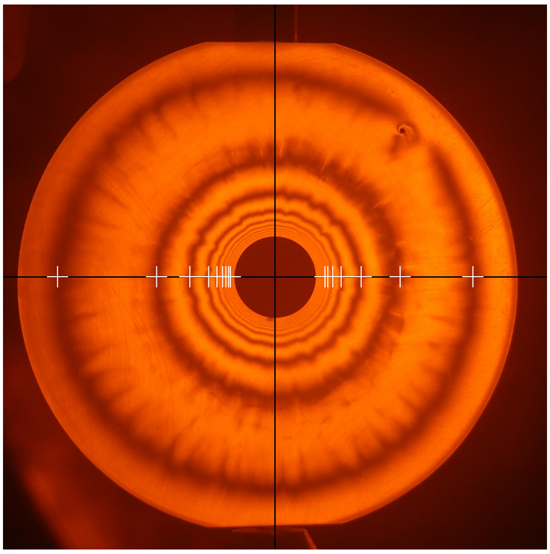

Figure 4.9 Slowly cooled test specimen, before insert is removed, where fringes are marked with white crosses.

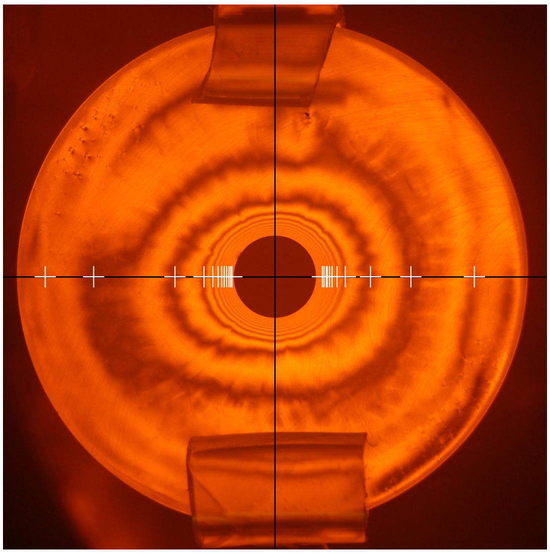

Figure 4.10 Quenched test specimen, before insert is removed, where fringes are marked with white crosses.

In the two images, black horizontal and vertical lines mark the centre of the test specimens. Furthermore, white crosses mark each fringe, along the horizontal line.

Figure 4.9 show a nearly perfectly circular fringe pattern. Figure 4.10, however, shows unsymmetrical fringes. This is assessed to be due to the quenching, which might not cool the test specimen evenly, and due to the handling of the test specimen when it is hot, to move it from the oven to the cold water and to remove it from the silicone mould.

The position of the fringes and the centre of the test specimen are found by analysing the colour intensity along a line, through the centre of the test specimen. It turns out, that the green colour intensity yields good results.

In figure 4.11, a plot of the colour intensity, along the horizontal black line of figure 4.10, is shown. In the plot, the minima of the colour intensity are marked by red crosses. Note that there is more fringes in the test specimen, than those marked in the figure. However, the position of the fringes of higher order cannot be identified with certainty.

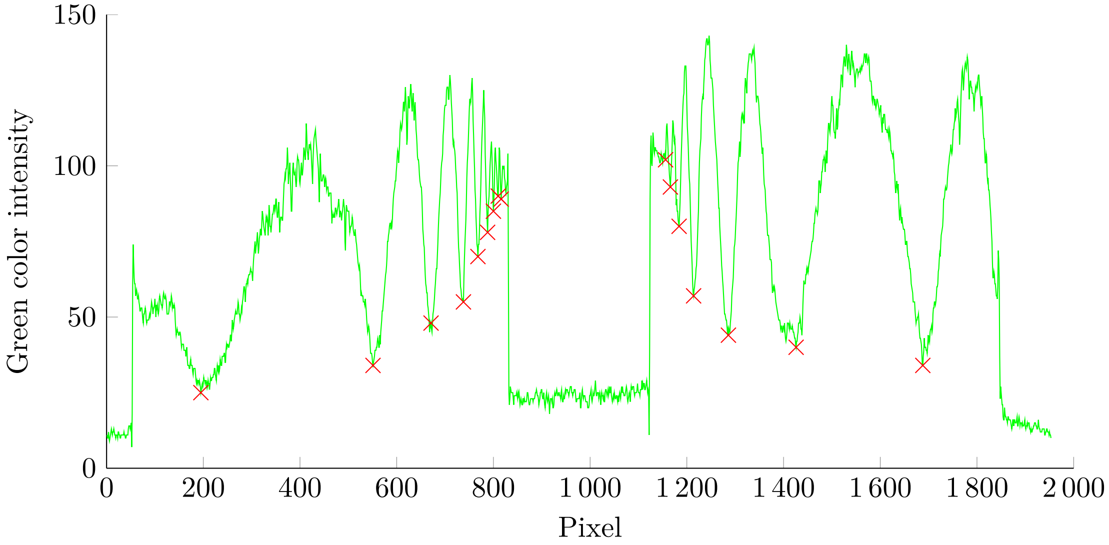

Figure 4.11 Colour intensity along horizontal line of slowly cooled test specimen, before insert removal.

From the plot of the colour intensity, the edges of the insert are visible. In figure 4.11, it is seen at around pixel 830 and 1120. By identifying the position of the insert, in both the horizontal and vertical direction, the black crosses of figure 4.9 and 4.10 are iteratively repositioned.

When the centre has been found, the pixel-position of each fringe and the outer edges of the test specimen is determined. From the difference between the outer edges, and a measured diameter of 76.5 mm for both test specimens, the position of the fringes is determined. The number of pixels between the outer edges varies from image to image, but it is approximately 1800 pixels. The accuracy of the diameter in pixels is assessed to be ±2 pixels. The accuracy of the diameter is assessed to be within ±0.2 mm. This yields an uncertainty of the length per pixel of less than ±0.4 %. The size of one pixel is less than 0.05 mm.

The accuracy of the fringe position, for fringes of 2^{nd} order or higher, is assessed to be ±1 pixel. This corresponds to approximately 0.1 mm.

To take thickness variations into account, the thickness of the test specimen is measured at the middle and at the edges. The thicknesses are given in table 4.1. It is assumed that the thickness throughout the width of the test specimen can be approximated by a liner interpolation.

	Left	**Middle**	**Right**
Slowly cooeld	5.19 mm	5.24 mm	5.14 mm
Quenched	4.90 mm	4.93 mm	4.71 mm

Table 4.1 Thickness of the two test specimens, at different positions.

In figure 4.12, the fringe orders, through the width of the two test specimens are seen.

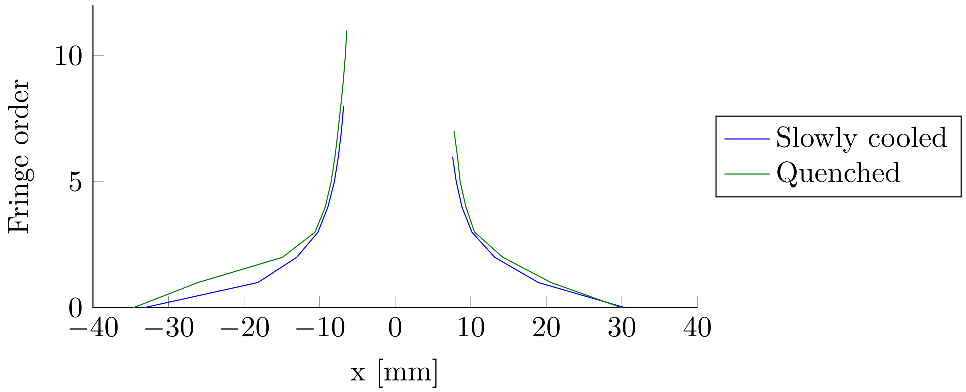

Figure 4.12 Fringe order along the horizontal centre line of the two test specimen, before the insert is removed.

The fact that the graphs in figure 4.12 is asymmetric, is not because the fringe pattern is asymmetric. It is simply because more fringes to the left of the insert were identifiable in the images.

The largest fringe order in figure 4.12 is 11. By using this value, and the stress-optical law in equation (4.1), with f_σ=18 616 $\frac{\text{N}}{\text{m}}$, a principal stress difference of 41.6 MPa is obtained. This, however, is an overestimation of the stress, because equation (4.1) is not valid in this case. As described in section 4.2, the fringes are time, temperature, and history dependent. The large fringe orders are assessed to occur due to creep at elevated temperatures. However, the stress-optical law is considered to be valid in the linearly elastic range only.

It is assumed, that equation (4.1) can be modified, to relate the change in principal stress difference with the change in fringe order, when a load is introduced. This is seen in equation (4.2). If the temperature is kept constant, and the change in fringe order is considered over a short time range, f_σ is assumed to be constant.

$$\Delta(\sigma_1 - \sigma_2) = \frac{\Delta N f_\sigma}{h} \tag{4.2}$$

where:

$\Delta(\sigma_1 - \sigma_2)$	Change in principal stress difference, [Pa]
ΔN	Change in fringe order, [ ]

It is furthermore assumed, that the test specimen is entirely stress-free, when the insert is removed. This assumption requires that the shape of the residual stress field has the same shape as the elastic stress field of a radial expansion of the insert. Thus, equation (4.2) can be used to evaluate the residual stress in the test specimen, by considering the change in fringe order, when the insert is removed.

In figure 4.13 and 4.14, the fringe patterns are seen, when the inserts are removed.

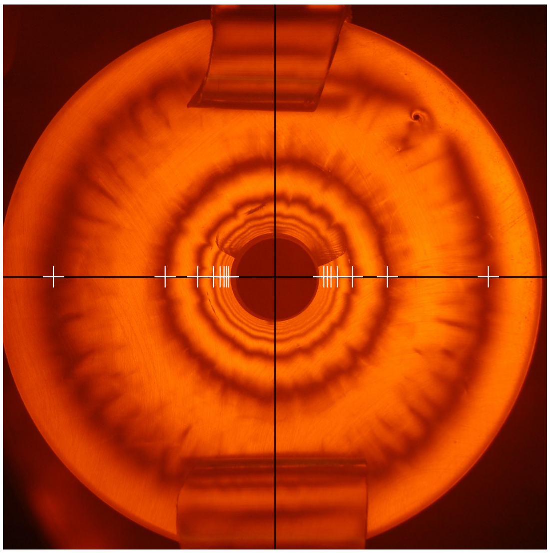

Figure 4.13 Slowly cooled test specimen, after insert is removed, where fringes are marked with white crosses.

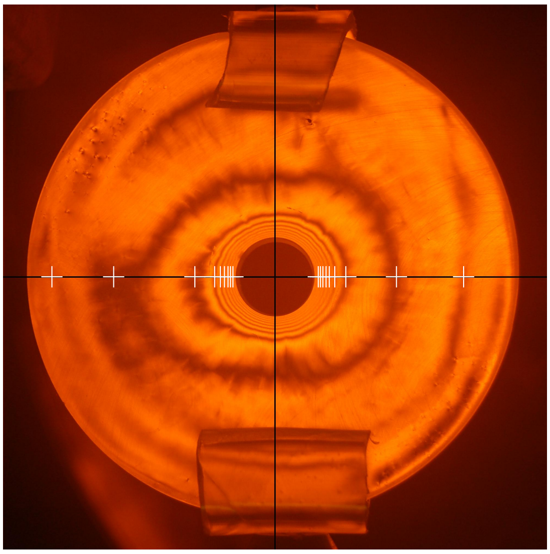

Figure 4.14 Quenched test specimen, after insert is removed, where fringes are marked with white crosses.

The fringes in figure 4.13 and 4.14 are not apparently different from the fringes in figure 4.9 and 4.10. However, by plotting the fringe order as a function of position, a difference is seen. This is shown in figure 4.15 and 4.16.

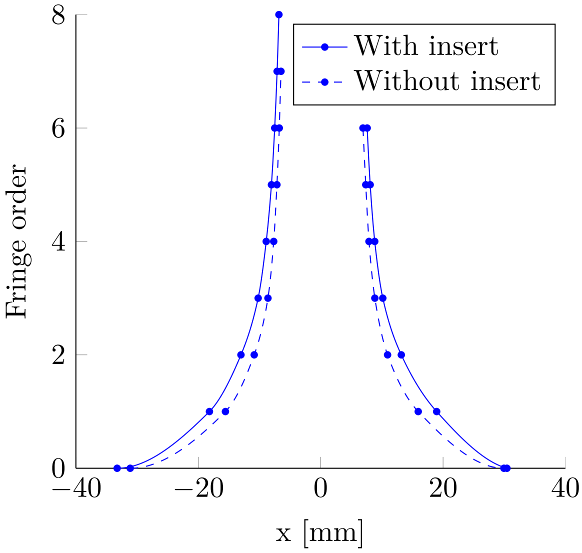

Figure 4.15 Fringe order in the slowly cooled test specimen, before and after the insert is removed.

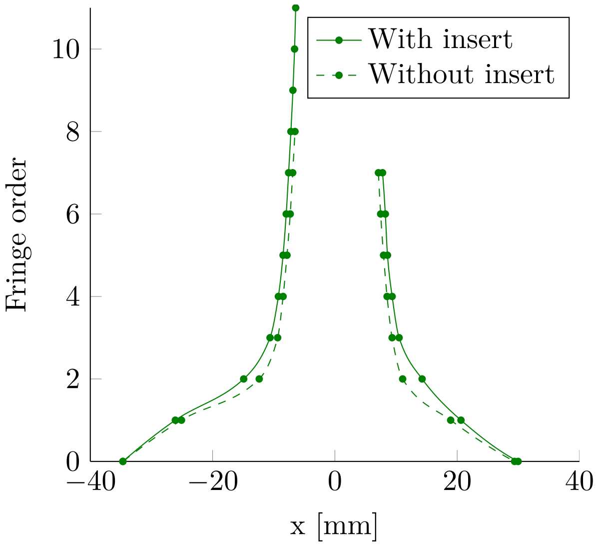

Figure 4.16 Fringe order in the quenched test specimen, before and after the insert is removed.

In the two figure, the maximum slope of the graphs is approximately 5 mm^{-1}. If the accuracy of the fringe position is 0.1 mm, the fringe order is accurate to within a half order.

The curves between the data points are cubic interpolations, to enable subtraction of the data sets. The interpolated curve of fringes without the insert is subtracted from the fringes with the insert. Equation (4.2) is used to calculate the residual stress curves, shown in figure 4.17.

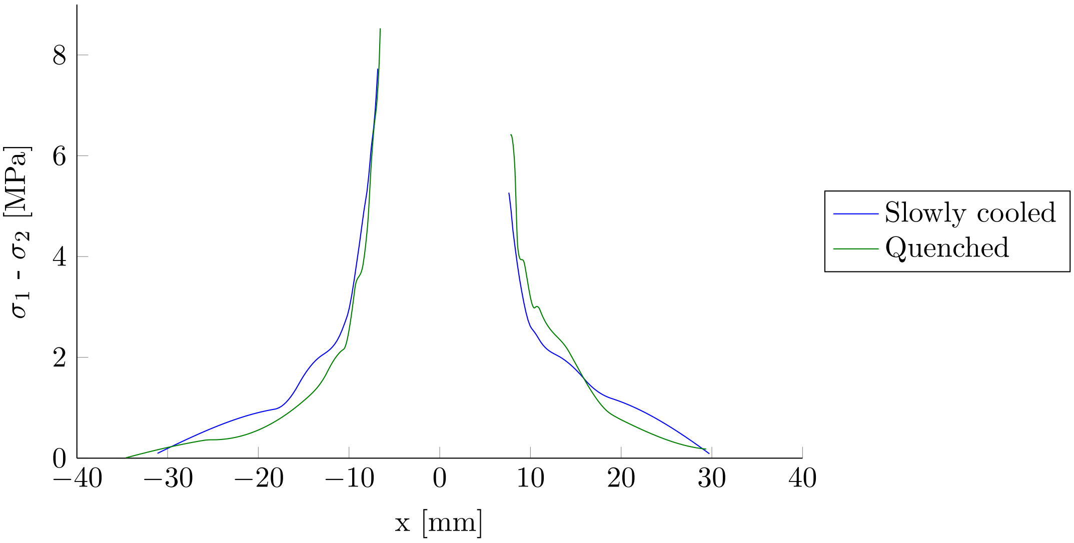

Figure 4.17 Residual stress in the two test specimens

If the uncertainty of the fringe order is up to a half order, the uncertainty of the difference between the fringe orders, before and after the insert is removed, is up to one order. This yields an uncertainty in the principal stress difference of up to 0.4 MPa.

As seen, the graphs are fairly irregular, which is considered to be due to the interpolation between the data points in figure 4.15 and 4.16.

There is only a small difference between the residual stress of test specimen which is slowly cooled and the test specimen which is quenched. Hence, it cannot be concluded, that the residual stress is dependent on the cooling rate. It is possible, that the residual stress is affected by a cooling rate faster than -270 $\frac{°\mathrm{C}}{\mathrm{min}}$, or slower than -5 $\frac{°\mathrm{C}}{\mathrm{min}}$.

4.3.4 Validation of fringe constant

In the previous section, it is assumed that the fringe constant, determined in appendix C can be used in equation (4.2). However, it is possible that f_σ in the calibration disc is different than f_σ in this experiment. It could differ due to differences in the degree of cure, the stress/strain history, or the level of retardation. Hence, an experiment is conducted, based on the same test specimen used in section 4.3.3, to validate f_σ.

A test specimen, where the insert is removed, is considered. A detrimental load is applied to the test specimen, as shown in figure 4.18.

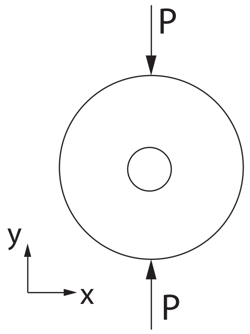

Figure 4.18 Sketch of the test specimen with the applied load

As in appendix C, the stress field from a theoretical method is compared with the fringes obtained in the polariscope.

The theoretical stress field is obtained by using the finite element method (FEM). The finite element code is written in MATLAB, by the author of this project. The code is appended on the appendix CD, appendix I, and the analysis is described in appendix D.

The experiment is conducted, by applying a load of 500 N and 1000 N to the test specimens, by using the same lever arm, described in appendix C. Images are captured of both the fringes of the slowly cooled and the quenched test specimen, with the two loads applied. The images are shown in figure 4.19 to 4.22.

As the edges of the test specimens are slightly inclined, the edge at the top and bottom has been sanded flat to reduce out of plane bending. Furthermore, a piece of a plastic tube is sliced and placed at the edge, to distribute the load better.

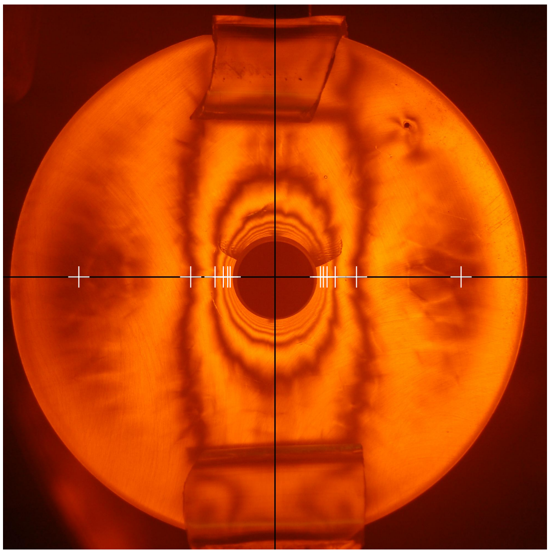

Figure 4.19 Slowly cooled test specimen, after insert is removed, with 500 N detrimental load, where fringes are marked with white crosses.

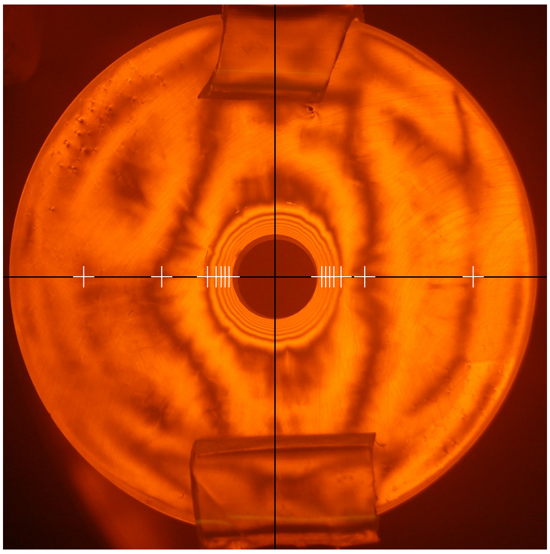

Figure 4.20 Quenched test specimen, after insert is removed, with 500 N detrimental load, where fringes are marked with white crosses.

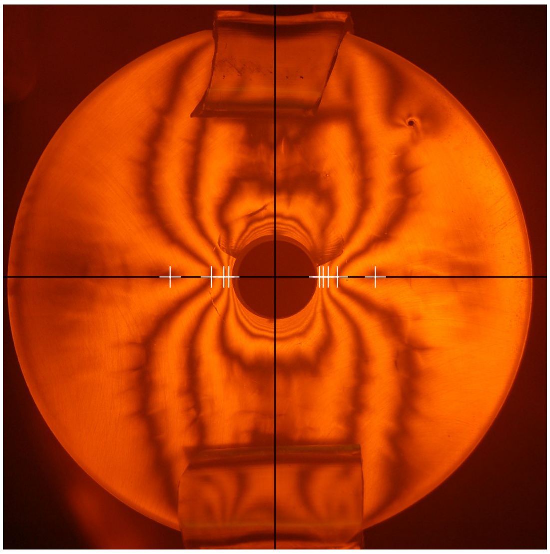

Figure 4.21 Slowly cooled test specimen, after insert is removed, with 1000 N detrimental load, where fringes are marked with white crosses.

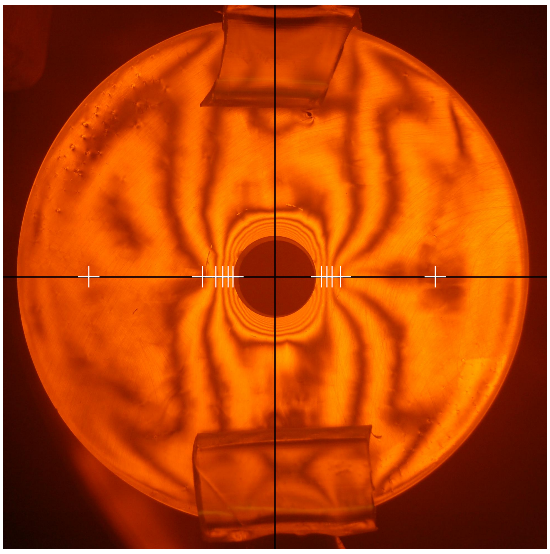

Figure 4.22 Quenched test specimen, after insert is removed, with 1000 N detrimental load, where fringes are marked with white crosses.

The fringes in the images have been analysed in the same way as in section 4.3.3, by use of equation (4.2). In figure 4.23 and 4.24, the stress along the horizontal centreline is shown, relative to the applied load.

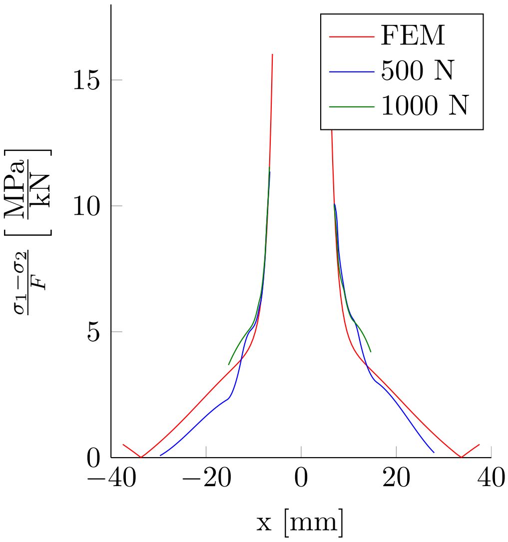

Figure 4.23 Stress, relative to the detrimental load, of the slowly cooled test specimen.

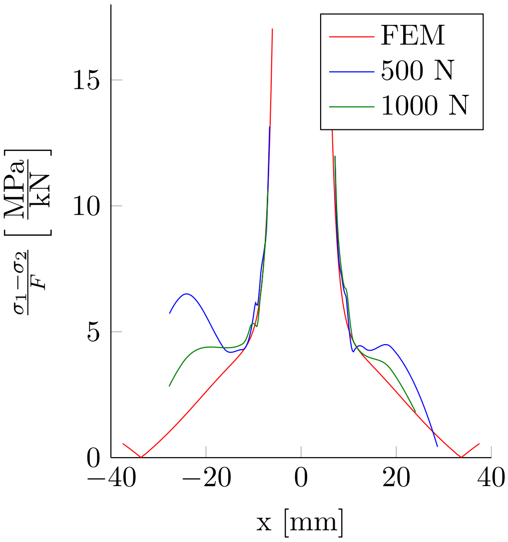

Figure 4.24 Stress, relative to the detrimental load, of the quenched test specimen.

As seen in the figures, there is very good correlation between the theoretical and experimental results for the slowly cooled test specimen. For the quenched test specimen, there is very good correlation near the centre. To the left, there is a significant deviation. However, as seen in figure 4.14, 4.20, and 4.24, the first and second (0^{th} and 1^{st} order) fringes to the left is not that well-defined.

It is assessed, that is a valid assumption to use the fringe constant determined in appendix C, to evaluate the residual stress field in section 4.3.3.

4.4 Photoelasticity at elevated temperature

In this section, in-situ photoelastic measurements are conducted. However, due to the reasons stated in section 4.2, the experimental results cannot be directly related to the stress field. Hence, this is merely a study of the relative retardation.

The test set-up shown in figure 4.1 and 4.2 has been used for the experiment. The test specimens are prepared in a silicone mould, and put in the modified oven. An external temperature controller, which is set for 100 °C is used for the oven. When the epoxy is solid, the silicone mould is removed and the test specimen is placed upright on the edge, by which images of the fringe pattern can be captured.

In figure 4.25, the temperature is shown as a function of time. The red dots mark the time at which an image is captured. Furthermore, the degree of cure is shown in the figure.

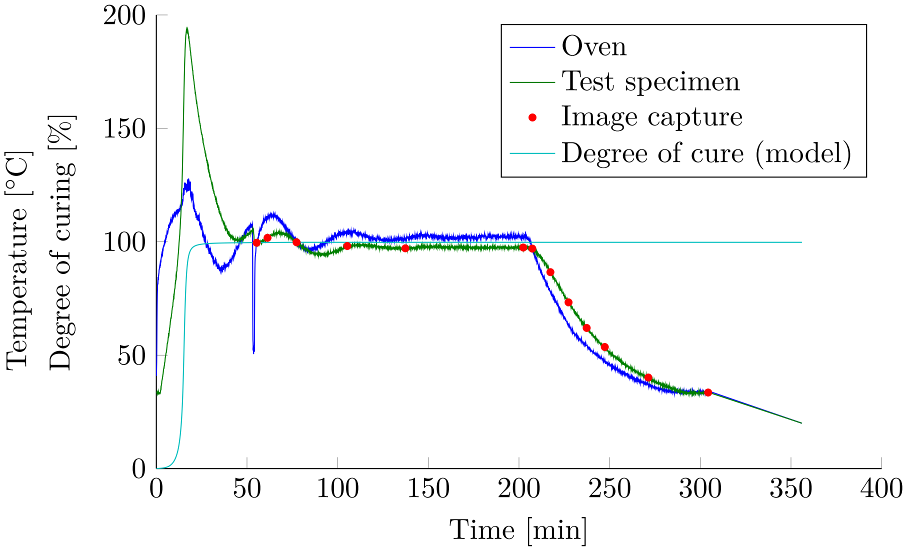

Figure 4.25 Temperatures, time of image capture, and degree of cure

At the time of the first image capture, the epoxy is almost fully cured. Hence, only the effect of time and temperature on the relative retardation can be considered.

The first image, which is captured, is seen in figure 4.26.

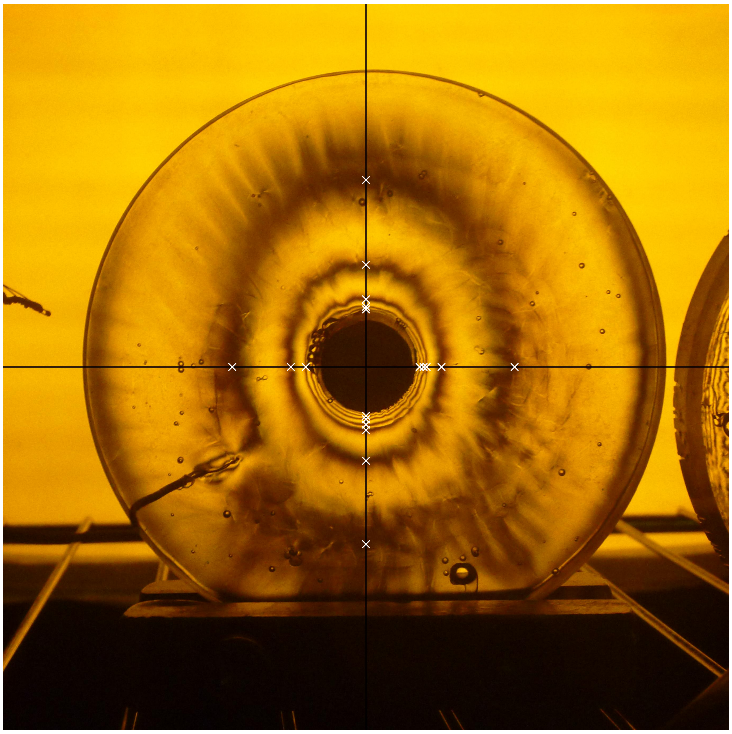

Figure 4.26 The first image of the in-situ photoelasticy experiment

As the test specimen is considered immediately after it is removed from the mould, it has not been sanded. Hence, the thickness of the test specimen is not even. The thickness varies because the mould has not been levelled as the epoxy cured, and because of rises near the edge of the test specimen and near the insert. This is assessed to affect the stress field, but also the fringe pattern, because the stress-optical law is dependent on thickness.

Another problem with the test set-up is the windows of the oven. The glass appears to cause some degree of relative retardation. The outer fringes of figure 4.26 has an elliptical shape. This shape is not due to the relative retardation inside the test specimen, as the elliptical shape remains if the test specimen is rotated.

However, in this experiment, the relative retardation is studied, by considering only the change in fringe order. As the data is not processed into stresses, it is considered that the effect of the varying thickness and the effect of the windows can be disregarded.

The 13 images which have been captured are analysed to obtain the position of the fringes. This is done as described in section 4.3.3, however in this case the fringes are identified along both the horizontal and vertical line, as shown in figure 4.26.

In figure 4.27 to 4.30, the position of the fringes are plotted as a function of time. In the plots, the 1^{st} graph from the top is the position of the 1^{st} order fringe, the 2^{nd} graph is the 2^{nd} order fringe, and so on.

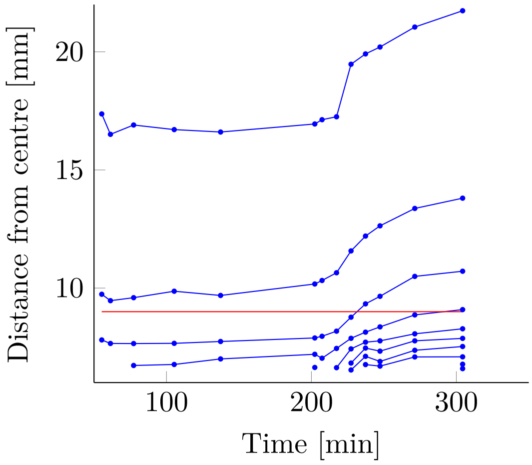

Figure 4.27 Position of fringes at the left part of horizontal centreline, plotted as a function of time

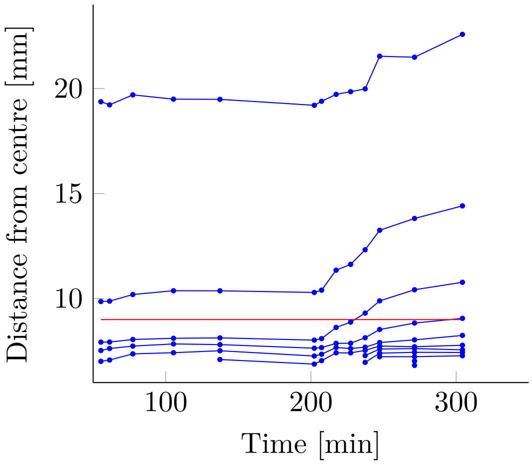

Figure 4.28 Position of fringes at the right part of horizontal centreline, plotted as a function of time

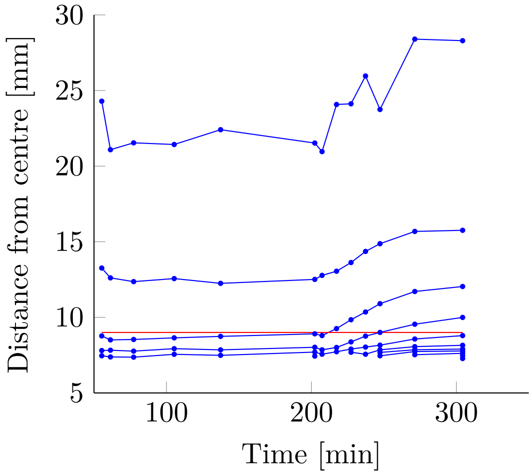

Figure 4.29 Position of fringes at the upper part of vertical centreline, plotted as a function of time

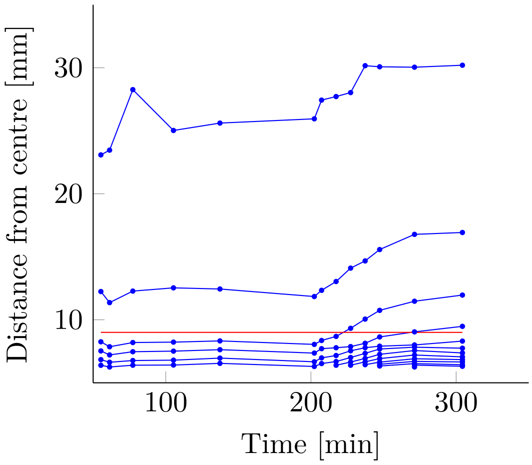

Figure 4.30 Position of fringes at the lower part of vertical centreline, plotted as a function of time

The red lines in figure 4.27 to 4.30 mark a distance of 9 mm from the centre. This distance is chosen as a compromise. It is desired to be near the insert, where the distance between the fringes is small, by which the fringe order can be determined more accurate. But, near the insert there is a change in the thickness, which is to be avoided.

The fringe order has been evaluated at this distance, at every captured image, by using a cubic interpolation between the fringes. The fringe orders are plotted as a function of time in figure 4.31. A normalised plot of the temperature is furthermore shown in the figure.

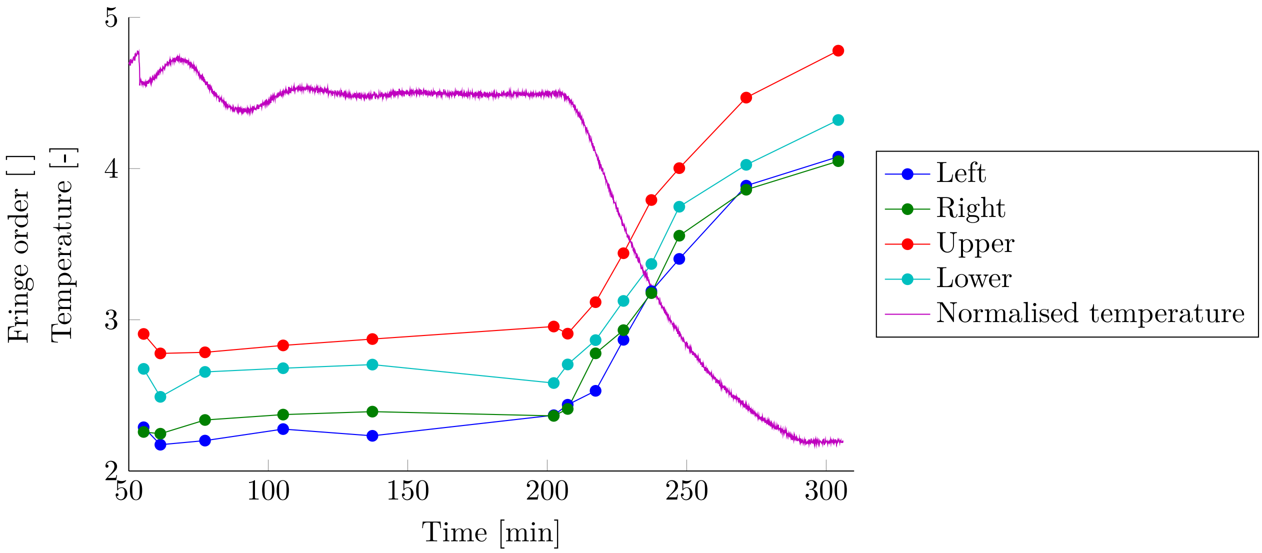

Figure 4.31 Fringe orders as a function of time, at a constant distance of 9 mm from the centre of the test specimen.

As seen in the figure, the fringe order does not vary much until after 200 min, when the oven is turned off. However, a slight increase in the first time range is noticeable. This is assessed to be due to temperature variations in the test specimen. During the time of the first 7 image captures, shown in figure 4.25, a slight decrease in temperature is noticeable as well.

There is an offset between the four graphs of the fringe order. This is assessed to be due to the variations in the thickness, discussed above, and because the image has not been aligned perfectly with the insert.

After approximately 200 min, the fringe orders increase. In figure 4.32, the fringe order is shown as a function of temperature.

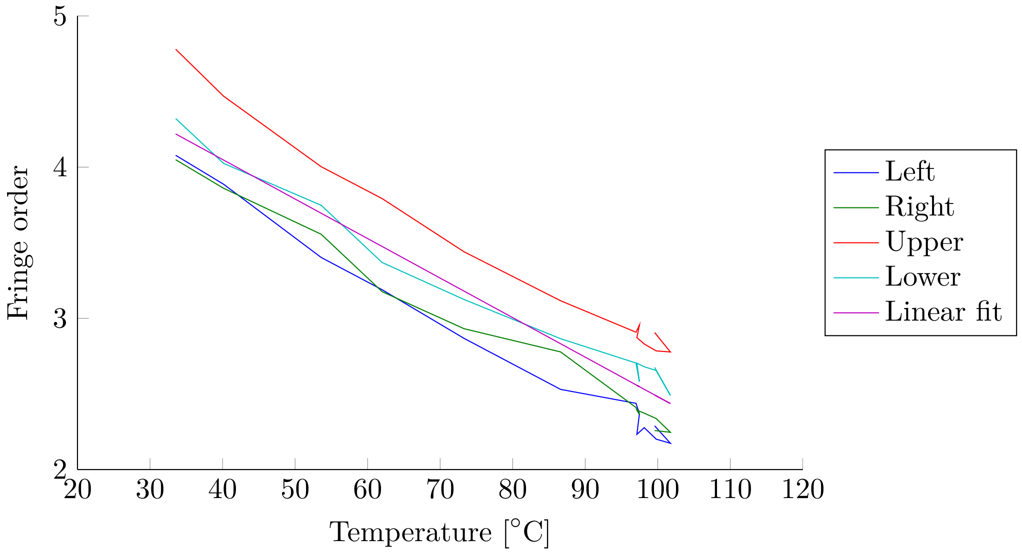

Figure 4.32 Fringe orders as a function of temperature, at a constant distance of 9 mm from the centre of the test specimen.

There is a nearly linear relation between the fringe order and the temperature. However, by comparing the graphs with the linear fit, shown in the figure, there is a tendency that the slope decreases with the temperature. As shown in section 3.3.3, the thermal strains of the test specimen is linearly dependent on the temperature, below T_g. Hence, the non-linearity of figure 4.32 is assessed to be due to temperature dependency of Young's modulus and f_σ.

4.5 Summary

In this chapter, experiments are conducted by using photoelastic measurements. It is determined, that the usual approach for photoelastic measurements cannot be used for determining the residual stress in the test specimen. However, another method has been developed, where the residual stress is determined by considering the change in the fringe pattern, when the insert is removed from the test specimen. It is furthermore determined, that the residual is not different whether the test specimen is quenched in water or slowly cooled.

The uncertainty of the principal stress difference is considered to be less than 0.4 MPa. However, the result is also dependent on the accuracy of f_σ, even though this has not been quantified.

Another experiment is conducted, where the relative retardation is considered at elevated temperature and during cooling. It is seen that there is a nearly linear relation between the relative retardation and the temperature. However, it cannot be conclusively related to the stress field of the test specimen during the process.

Part II

Numerical approach

In this part of the report, the numerical modelling is considered. In chapter 5, the development of the model is described. The model is made in different versions, based on different material models. The material models are either elastic, viscoelastic, or pseudo-viscoelastic models.

In chapter 6, the results which are obtained by the numerical models is shown. The results are furthermore compared with the experimental measurements, described in part I.

Residual stress modelling

5

In this chapter, it is considered how to model the curing process of the test specimen, described in section 1.2, to estimate the residual stress.

Hahn and Pagano [1975] are among the first to present literature of a method for modelling residual stresses in composite laminates. The method is based on the assumption, that the composite is completely stress-free at the temperature of the curing. Hence, the residual stress is solely developed during cooling. The authors assume an elastic material, with Young's modulus and thermal strains which are linearly dependent on the temperature. By using classical laminate theory (CLT), the authors estimate the stress in a symmetric laminate.

White and Hahn [1992a] presents a method, which takes the viscoelastic effect into account, to model the residual stress of a thin laminates of fibre composites. The model, furthermore, includes the chemical shrinkage. It is shown by the experimental validation, that the matrix has a quite significant creep response at low degrees of curing. The strain due to chemical shrinkage is also significant. However it does not contribute much to the residual stress due to the low mechanical properties and the creep response at the time the chemical shrinkage occur. [White and Hahn, 1992b]

Bogetti and Gillespie [1992] presents a one dimensional model, which simulates the residual stress through the thickness of a thick laminate, by including a thermal model. Due to the lack of viscoelastic material behaviour, the model overestimates the deformation early in the process. However, the model includes residual stress due to temperature variation, and degree of curing, through the thickness. This temperature variation is significant in thick laminate composites. This model disagrees with the simple assumption of a stress free temperature, which is used by Hahn and Pagano [1975].

The elastic method is a simple approach, but it is not sophisticated enough to yield good results. [Zobeiry, 2006] However, a viscoelastic method might require a lot of material characterisation and computational time. Zobeiry [2006] has conducted a theoretical comparison of viscoelastic methods, and methods known as pseudo-viscoelastic methods, which shows good agreement. One pseudo-viscoelastic model is the cure hardening instantaneously linear elastic (CHILE) model.

In this project, the finite element method (FEM) is used to simulate the curing process, to obtain the stress and strains as a function of time. Different approaches are used, which are based on elastic, viscoelastic, and pseudo-viscoelastic models, respectively.

To simulate the curing process, the model must include multiple physical effects. Generally the model should include three different physical phenomena: thermal heat transfer, the chemical reaction and the structural deformation due to induced stresses in the material. These are considered in the following sections.

5.1 Thermal model

The thermal model should be used to predict the temperature throughout the test specimen. The uncured test specimen is at room temperature, when it is placed in the preheated oven. Hence, heat is transferred into the test specimen. However, the curing reaction is an exothermic chemical reaction, by which heat is also produced within the test specimen. This causes temperature gradients inside the test specimen, which causes heat transfer by both diffusion and convection.

It is not considered to be a simple task to model such a system. Hence, this project has been delimited from modelling the thermal system. Instead, the temperature is based on actual temperature measurements of the experiments considered in part I. As shown in appendix A, there is difference in temperature through the thickness of the test specimen. However, to simplify the model and the temperature measurements, it is assumed that the temperature is uniform throughout the test specimen.

Because the set-up used for the temperature measurements is not able to measure temperatures below approximately 34 °C, the dataset is modified by including an extra data point at 20 °C.

5.2 Curing model

To take the effects of the cure into account, a model of the curing kinetics is used. The model which is used is presented by Jakobsen et al. [2013a]. It is chosen, because it is based on experimental measurements on the same epoxy resin, which is used for the test specimen in this project. The model is used without modifications of the model or the parameters. However, as the curing model is an essential part of the model, it presented in the following.

The model is based on isothermal differential scanning calorimetry (DSC) measurements in the temperature range from 40 to 120 °C.

In equation (5.1), an expression for the maximum degree of cure is given. It is seen from this model that the temperature must be above 374 K to obtain a complete curing of the epoxy resin.

$$c_{max}(T) = \begin{cases} \sum_{i=1}^{2} 1 - g_{1i}(e^{-g_{2i}T})^{g_{3i}} & \text{if} \quad 300\text{K} < T < 374\text{K} \\ 1 & \text{if} \quad 374\text{K} < T \end{cases} \tag{5.1}$$

where: [Jakobsen et al., 2013a]

c_{max}	Maximum degree of cure at a given temperature, [ ]
g_{ji}	Parameter in the model for c_{max}, [-]
T	Temperature, [K]

The parameters in equation (5.1) has been determined by fitting the model to experimental data. The parametres are given in table 5.1.

	i=1	i=2
g_{1i} [ ]	$2.471\ 10^5$	1.099
g_{2i} [K^{-1}]	0.051	0.039
g_{3i} [ ]	0.873	0.007

Table 5.1 Parameters used in equation (5.1) [Jakobsen et al., 2013a]

In equation (5.2), a model for the curing rate is given. If the degree of cure is greater than the maximum degree of cure, given by equation (5.1), the curing rate is zero.

$$\dot{c}\,(c,T) = \begin{cases} \sum_{i=1}^{3} A_i e^{\left(\frac{-E_i}{RT}\right)} c^{n_i} (c_{max}(T) - c)^{m_i} & \text{if} \quad 0 \le c < c_{max}(T) \\ 0 & \text{else} \end{cases} \tag{5.2}$$

where: [Jakobsen et al., 2013a]

$\dot{c}$	Rate of cure, $\left[s^{-1}\right]$
c	Degree of cure, [ ]
A_i	Parameter in the model for $\dot{c}$, $\left[s^{-1}\right]$
E_i	Parameter in the model for $\dot{c}$, $\left[\frac{\mathrm{J}}{\mathrm{mol}}\right]$
R	Ideal gas constant, $\left[\frac{\mathrm{J}}{\mathrm{mol\,K}}\right]$
n_i	Parameter in the model for $\dot{c}$, [ ]
m_i	Parameter in the model for $\dot{c}$, [ ]

A value of R=8.3144621 is used for the ideal gas constant. [Mohr et al., 2010] The other parameters are given in table 5.2. As the parameters in table 5.1, these are obtained by fitting the model to experimental data from the DSC measurements.

	i=1	i=2	i=3
A_i $[\mathrm{s}^{-1}]$	27 925	171 320	0.479
E_i $[\frac{\mathrm{J}}{\mathrm{mol}}]$	54 293	53 768	21 439
n_i [ ]	0	1.087	1.190
m_i [ ]	1.358	4.016	1.066

Table 5.2 Parameters used in equation (5.2) [Jakobsen et al., 2013a]

From equation (5.2), the degree of cure is calculated by integrating over time, as shown in equation (5.3).

$$c(t) = \int_0^t \dot{c}\,(c(t'), T(t'))\mathrm{d}t' \tag{5.3}$$

where:

t	Time, [s]
t'	Dummy variable of time, [s]

5.3 Mechanical model

As stated before, the mechanical model of the test specimen is based on the finite element method. Four different models are presented, an elastic model, two viscoelastic models, and the CHILE model. These are described in the following.

All the material models are implemented in the same non-linear FEM code, as described in section 5.5. Hence, they are all formulated by the same approach. The model is based on an method presented by Henriksen [1984]. However, it has been modified to be based on other material models, and to include the time and temperature dependent material properties.

The method presented by Henriksen [1984] is derived from a uniaxial integral formulation of the strains, as a function of the creep compliance modulus. The strain formulation is afterwards written in the form:

$$\varepsilon^m(t) = D_I \sigma(t) + \varepsilon^H(t) \tag{5.4}$$

where: [Henriksen, 1984]

ε^m	Mechanical strain, [ ]
D_I	Instantaneous compliance, $\left[\text{Pa}^{-1}\right]$
σ	Stress, [Pa]
ε^H	Hereditary strain, [ ]

In the following sections, formulations of strains are described, for the mechanical models. The mechanical models are formulated from the storage and loss moduli. Models for these are presented in section 5.4.

5.3.1 Elastic model

The elastic model is the simplest approach to the problem. It is assumed that the viscoelastic effect of the epoxy is negligible, by which the system is modelled as elastic. However, it must be taken into account, that the properties of the material are dependent on temperature and the degree of cure.

According to Zobeiry [2006], it is a reversible process, when the temperature is changed in a material with a temperature dependent stiffness. The process is path independent, by which it is only dependent on the initial and final state of the parameters. Therefore, the constitutive relation for a thermoelastic system is written as:

$$\sigma(t) = E(T(t), c(t))\, \varepsilon^m(t) \tag{5.5}$$

where: [Zobeiry, 2006]

E	Young's modulus, [Pa]

However, if the stiffness is changed due the chemical process of curing, the process is irreversible. In that case, the final deformation is history dependent. [Zobeiry, 2006]

In the process considered in this project, the stiffness changes due to both temperature and cure. Hence, Young's modulus should be divided into one part which is path independent, and another part which is path dependent. However, in the model for Young's modulus, presented in section 5.4.3, the temperature dependent contribution is considerably larger than the cure dependent contribution. Hence, the elastic model is considered to be entirely path independent, as shown by equation (5.5).

In the elastic model, Young's modulus is assumed to be equal to the storage modulus. It is modelled as $E'(T(t),c(t))$. Hence, equation (5.5) can be rearrange to yield the strains, as given in equation (5.6).

$$\varepsilon_E(t) = \frac{\sigma(t)}{E'(T(t), c(t))} \tag{5.6}$$

where:

ε_E	Strain from the elastic model, [ ]
E'	Storage modulus, [Pa]

It is seen, that equation (5.6) is in the form of equation (5.4). Hence, the instantaneous compliance and the hereditary strain, for the elastic model, are given as:

$$D_I(t) = \frac{1}{E'(T(t), c(t))} \tag{5.7}$$

$$\varepsilon^H(t) = 0 \tag{5.8}$$

5.3.2 Viscoelastic model

In this section, the viscoelastic models are presented. The viscoelastic models, however, are to be based on the models of the storage modulus and the loss modulus only (presented in section 5.4.3), because no other data is available. Hence, the viscoelastic models must be formulated from material models, dependent on only two parameters. These two parameters are then determined by from the storage modulus and the loss modulus.

Hence, only very simple viscoelastic material models can be used. These are not expected to yield very accurate results, because only the very basic material behaviour can be represented. To apply more advanced material models, additional models of the material properties or experimental material characterisation is required. However this is beyond the scope of this project.

Because the models can only have two parameters, the Maxwell and Kelvin models are considered. These are illustrated in figure 5.1 and 5.2 as simple spring and dashpot models.

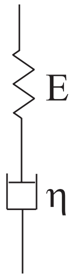

Figure 5.1 Maxwell model, represented as a spring and dashpot model. Illustration from Schjødt-Thomsen [2005], which has been modified.

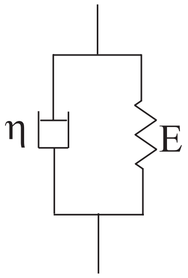

Figure 5.2 Kelvin model, represented as a spring and dashpot model. Illustration from Schjødt-Thomsen [2005], which has been modified.

The strains of the two models are generally expressed by using the Boltzmann superposition integral, given in equation (5.9).

$$\varepsilon(t) = \int_0^t D(t - t', T, c) \frac{\partial \sigma(t')}{\partial t'} \mathrm{d}t' \tag{5.9}$$

[Schjødt-Thomsen, 2005]

Where the compliance moduli, D, for the two models are given in equation (5.10) and (5.11).

$$D_M(t,T,c) = \frac{1}{E(T,c)} + \frac{t}{\eta(T,c)} \tag{5.10}$$

$$D_K(t,T,c) = \frac{1}{E(T,c)} \left(1 - e^{-\left(\frac{E(T,c)}{\eta(T,c)}t\right)}\right) \tag{5.11}$$

where: [Schjødt-Thomsen, 2005]

D_M	Compliance modulus of Maxwell model, $\left[\mathrm{Pa}^{-1}\right]$
D_K	Compliance modulus of Kelvin model, $\left[\mathrm{Pa}^{-1}\right]$
η	Viscosity, $\left[\frac{\mathrm{kg}}{\mathrm{sm}}\right]$

However, because the temperature, T, and the degree of cure, c, are functions of time in this case, this approach is not valid. Thus, the strain is formulated by using the differential equations of the two models.

Zobeiry [2006] discusses the problem, for the Maxwell model. The spring element is considered to behave as the elastic model, where the effect of curing and temperature are treated differently. The dashpot element, however, is considered to be irreversible, and is modelled as equation (5.12).

$$\sigma(t) = \eta(t)\, \dot{\varepsilon}_{dashpot}\,(t) \tag{5.12}$$

where: [Zobeiry, 2006]

$\dot{\varepsilon}_{dashpot}$	Strain rate of dashpot element, $\left[\mathrm{s}^{-1}\right]$

In the model developed in this project, it is assumed that the spring elements in both the Maxwell and Kelvin models behave as the elastic model in section 5.3.1.

In the following, the strain is expressed from the two models, as functions of the storage and loss moduli.

Maxwell

The Maxwell model is based on a differential equation, which takes the thermoelastic effect into account. It is obtained by considering, that the total strain rate is the sum of the strain rates of the spring and dashpot elements, as given by equation (5.13).

$$\dot{\varepsilon} = \dot{\varepsilon}_{spring} + \dot{\varepsilon}_{dashpot} \tag{5.13}$$

where: [Zobeiry, 2006]

$\dot{\varepsilon}$	Strain rate, $\left[\mathrm{s}^{-1}\right]$
$\dot{\varepsilon}_{spring}$	Strain rate of spring element, $\left[\mathrm{s}^{-1}\right]$

$\dot{\varepsilon}_{spring}$ is determined by considering the model of the spring element, equation (5.5). $E(T(t), c(t))$ in equation (5.5) is written as $E(t)$, after which the expression is differentiated w.r.t. time:

$$\frac{\mathrm{d}\sigma(t)}{\mathrm{d}t} = \frac{\mathrm{d}E(t)}{\mathrm{d}t}\varepsilon(t) + E(t)\frac{\mathrm{d}\varepsilon(t)}{\mathrm{d}t} \tag{5.14}$$

[Zobeiry, 2006]

$\varepsilon(t)$ is expressed as $\frac{\sigma(t)}{E(t)}$, after which the expression is solved w.r.t. the time derivative of the strain. This is inserted in equation (5.13) together with $\dot{\varepsilon}_{dashpot}$, determined from the model of the dashpot, equation (5.12). This yield the expression given as equation (5.15).

$$\frac{\mathrm{d}\varepsilon(t)}{\mathrm{d}t} = \frac{1}{E(t)}\frac{\mathrm{d}\sigma(t)}{\mathrm{d}t} - \frac{\sigma(t)}{E(t)^2}\frac{\mathrm{d}E(t)}{\mathrm{d}t} + \frac{\sigma(t)}{\eta(t)} \tag{5.15}$$

[Zobeiry, 2006]

By integration of equation (5.15), the strain is obtained as a function of time, as shown in equation (5.16).

$$\varepsilon(t) = \int_0^t \frac{1}{E(t')}\frac{\mathrm{d}\sigma(t')}{\mathrm{d}t'} - \frac{\sigma(t')}{E(t')^2}\frac{\mathrm{d}E(t')}{\mathrm{d}t'} + \frac{\sigma(t')}{\eta(t')}\mathrm{d}t' \tag{5.16}$$

In appendix F, D_I and ε^H are derived from equation (5.16). This yields the expressions given in equation (5.17) and (5.18).

$$D_I(t_n) = \frac{1}{2E(t_{n-1})} + \frac{1}{2E(t_n)} - \frac{E(t_n) - E(t_{n-1})}{2E(t_n)^2} + \frac{t_n - t_{n-1}}{2\eta(t_n)} \tag{5.17}$$

$$\begin{aligned}\varepsilon^H(t_n) = &\sum_{k=1}^{n-1} \Bigg\{ \left(\frac{1}{2E(t_{k-1})} + \frac{1}{2E(t_k)} - \frac{E(t_k) - E(t_{k-1})}{2E(t_k)^2} + \frac{t_k - t_{k-1}}{2\eta(t_k)} \right) \sigma_{ij}(t_k) \\ &- \left(\frac{1}{2E(t_{k-1})} + \frac{1}{2E(t_k)} + \frac{E(t_k) - E(t_{k-1})}{2E(t_{k-1})^2} - \frac{t_k - t_{k-1}}{2\eta(t_{k-1})} \right) \sigma_{ij}(t_{k-1}) \Bigg\} \\ &- \left(\frac{1}{2E(t_{n-1})} + \frac{1}{2E(t_n)} + \frac{E(t_n) - E(t_{n-1})}{2E(t_{n-1})^2} - \frac{t_n - t_{n-1}}{2\eta(t_{n-1})} \right) \sigma_{ij}(t_{n-1})\end{aligned} \tag{5.18}$$

Equation (5.17) and (5.18) are functions of Young's modulus and the viscosity. Hence, these are determined as a function of the storage and loss modulus.

If the Maxwell model is presented in the complex form, and applied a oscillating load, the storage and loss modulus is related to the E and η, as shown by equation (5.19).

$$E' + iE'' = \frac{\eta^2\omega_{load}^2 E}{\eta^2\omega_{load}^2 + E^2} + i\frac{\eta\omega_{load}E^2}{\eta^2\omega_{load}^2 + E^2} \tag{5.19}$$

where: [Schjødt-Thomsen, 2005]

ω_{load}	Frequency of the applied load, $\left[\mathrm{s}^{-1}\right]$

The models of E' and E'' are based on experiments where the load was applied with a frequency of 2π s^{-1}. Hence, this value is used as ω_{load}.

Equation (5.19) is solved to obtain E and η as a function of time, defined by E' and E''

$$E(t) = \frac{E'(t)^2 + E''(t)^2}{E'(t)} \tag{5.20}$$

$$\eta(t) = \frac{E'(t)^2 + E''(t)^2}{\omega_{load}E''(t)} \tag{5.21}$$

Kelvin

The differential equation of the Kelvin model is given as equation (5.22).

$$\sigma = E\varepsilon + \eta\frac{\mathrm{d}\varepsilon}{\mathrm{d}t} \tag{5.22}$$

[Schjødt-Thomsen, 2005]

This formulation is obtained as the sum of the stress from the spring element and the dashpot, equation (5.5) and (5.12).

Equation (5.22) is solved with respect to ε, as shown in equation (5.23).

$$\varepsilon = \frac{\sigma}{E} - \frac{\eta}{E}\frac{\mathrm{d}\varepsilon}{\mathrm{d}t} \tag{5.23}$$

D_I and ε^H are derived from equation (5.23), as described in appendix F. This yields equation (5.24) and (5.25)

$$D_I(t_n) = \frac{t_n - t_{n-1}}{(E(t_n)(t_n - t_{n-1}) + \eta(t_n))} \tag{5.24}$$

$$\varepsilon^H(t_n) = \frac{\eta(t_n)\varepsilon(t_{n-1})}{(E(t_n)(t_n - t_{n-1}) + \eta(t_n))} \tag{5.25}$$

As for the Maxwell model, the E and η in the Kelvin model can be expressed from the loss and storage modulus.

The complex creep compliances, the storage compliance and the loss compliance, can be related to the parameters of the Kelvin model.

$$D' - iD'' = \frac{E}{E^2 + \omega_{load}^2\eta} - i\frac{\omega_{load}\eta}{E^2 + \omega_{load}^2\eta} \tag{5.26}$$

where: [Schjødt-Thomsen, 2005]

D' | Storage compliance, $\left[\mathrm{Pa}^{-1}\right]$
D'' | Loss compliance, $\left[\mathrm{Pa}^{-1}\right]$

The storage and loss compliances can be related to the storage and loss moduli through equation (5.27).

$$\left(E' + iE''\right)\left(D' - iD''\right) = 1 \tag{5.27}$$

[Schjødt-Thomsen, 2005]

Equation (5.26) and (5.27) are solved to obtain E and η, as seen in equation (5.28) and (5.29).

$$E(t) = E'(t) \tag{5.28}$$

$$\eta(t) = \frac{E''(t)}{\omega_{load}} \tag{5.29}$$

5.3.3 Cure hardening instantaneously linear elastic model

The description of the CHILE model is based on Zobeiry [2006]. However, the expressions presented by Zobeiry [2006] is not used directly, because it is based on the relaxation modulus. Hence, the expressions are reformulated to be based on the compliance modulus, for the use in this project.

The CHILE model is based on the instantaneously linear relation given in equation (5.30).

$$\Delta\varepsilon = D_{CHILE}\Delta\sigma \tag{5.30}$$

where:

$\Delta\varepsilon$	Increment in strain, [ ]
D_{CHILE}	Compliance modulus, used in the CHILE model, $\left[\mathrm{Pa}^{-1}\right]$
$\Delta\sigma$	Increment in stress, [Pa]

The integral form of the CHILE model is given as:

$$\varepsilon(t) = \int_0^t D_{CHILE}(T(t'), c(t'))\frac{\partial\sigma(t')}{\partial t'}\mathrm{d}t' \tag{5.31}$$

As seen, equation (5.31) is very similar to equation (5.9). However, D_{CHILE} is not directly a function of $(t - t')$. But D_{CHILE} is indirectly a function of $(t - t')$. If the inverse storage modulus is used for D_{CHILE}, the model will be in a form known as a ”constant frequency” pseudo-viscoelastic method. In that case, D_{CHILE} will be the viscoelastic creep compliance, evaluated at a constant time, indirectly determined by the frequency ω_{load}. [Zobeiry, 2006]

According to Zobeiry [2006], a low frequency is typically used for, ω_{load}, e.g. 0.1 Hz. However, there are no direct criteria for a good value. In this project, frequency is 1 Hz, because the model of the storage modulus is based on experiments with that frequency.

From equation (5.31), expressions for D_I and ε^H is derived in appendix F. These are given as equation (5.32) and (5.33).

$$D_I(t_n) = \frac{D_{CHILE}(t_n) + D_{CHILE}(t_{n-1})}{2} \tag{5.32}$$

$$\begin{aligned}\varepsilon^H(t_n) = &\sum_{k=1}^{n-1} \frac{(\sigma(t_k) - \sigma(t_{k-1}))\left(D_{CHILE}(t_k) + D_{CHILE}(t_{k-1})\right)}{2} \\ &- \frac{\sigma(t_{n-1})\left(D_{CHILE}(t_n) + D_{CHILE}(t_{n-1})\right)}{2}\end{aligned} \tag{5.33}$$

D_{CHILE} is determined as the inverse of the storage modulus:

$$D_{CHILE}(c(t), T(t)) = \frac{1}{E'(c(t), T(t))} \tag{5.34}$$

5.3.4 2D formulation

In the previous sections, D_I and ε^H are derived for different material models in 1D. In this section, a 2D constitutive relation is formulated from the values of D_I and ε^H.

The mechanical model is formulated in 2D, according to the approach presented by Henriksen [1984]. However, where Henriksen [1984] formulates the model from four components of stresses and strain (three in-plane components and one normal to the plane), the model in this project is formulated from the three in-plane components only, based on the assumption of plane stress.

Equation (5.4) is expanded to 2D by including $[V]$, which is a matrix including Poisson's ratio:

$$\{\varepsilon^m\} = D_I[V]\{\sigma\} + [V]\{\varepsilon^H\} \tag{5.35}$$

where: [Henriksen, 1984]

$\{\varepsilon^m\}$	Vector of mechanical strain, [ ]
$[V]$	Matrix which includes Poisson's ratio, [ ]
$\{\sigma\}$	Vector of stresses, [Pa]
$\{\varepsilon^H\}$	Vector of hereditary strain, [ ]

Where, $\{\varepsilon^m\}$, $\{\sigma\}$, and $\{\varepsilon^H\}$ are defined as:

$$\{\varepsilon^m\} = \begin{Bmatrix} \varepsilon^m_{xx} \\ \varepsilon^m_{yy} \\ \gamma_{xy} \end{Bmatrix} \;,\; \{\sigma\} = \begin{Bmatrix} \sigma_{xx} \\ \sigma_{yy} \\ \sigma_{xy} \end{Bmatrix} \;,\; \{\varepsilon^H\} = \begin{Bmatrix} \varepsilon^H_{xx} \\ \varepsilon^H_{yy} \\ \gamma^H_{xy} \end{Bmatrix} \tag{5.36}$$

$[V]$ is determined from the coefficients of Hook's law for plane stress, obtained from Kildegaard [2012]. If the last term in equation (5.35) is removed, and D_I is replaced with $\frac{1}{E}$, it should resemble Hook's law. The matrix $[V]$ is given in equation (5.37).

$$[V] = \begin{bmatrix} 1 & -\nu & 0 \\ -\nu & 1 & 0 \\ 0 & 0 & 2(1+\nu) \end{bmatrix} \tag{5.37}$$

where:

ν	Poisson's ratio, [ ]

ν is considered to vary through the process. At first, when the epoxy resin is in the viscous phase, it is considered to behave as an incompressible liquid, which has a Poisson's ratio of 0.5. When it is fully cured and at room temperature, it is assessed to be a value of approximately ν=0.37 [Lund, 2013]. However, in this model it is assumed to be independent on time, temperature, or degree of cure. Hence the value ν=0.37 is used throughout the process.

By solving equation (5.35) with respect to $\{\sigma\}$, equation (5.38) is obtained.

$$\{\sigma\} = [M]\{\varepsilon^m\} - \frac{1}{D_I}\{\varepsilon^H\} \tag{5.38}$$

where: [Henriksen, 1984]

$[M]$	Matrix in constitutive relation, $\left[\mathrm{Pa}^{-1}\right]$

The matrix $[M]$ is:

$$[M] = \frac{1}{D_I(1-\nu^2)} \begin{bmatrix} 1 & \nu & 0 \\ \nu & 1 & 0 \\ 0 & 0 & \frac{1-\nu}{2} \end{bmatrix} \tag{5.39}$$

5.4 Material parameters

In this section, it is described how the material properties of the epoxy resin are modelled. Most of the properties vary with temperature and degree of curing, which must be taken into account.

In section 5.3, different material models are presented, however, they are all based on the same material properties.

c_{gel}, the degree of cure at the gel point, is an important parameter for the model of the material properties. In section 3.3.2, c_{gel} was found to be 0.67, from the DIC measurements.

5.4.1 Glass transition temperature

Some properties have a distinct change around the glass transition temperature (T_g). T_g is modelled as a linear function of the degree of cure, as shown in equation (5.40).

$$T_g(c) = 175c + 174 \text{ [K]} \tag{5.40}$$

where: [Jakobsen et al., 2013b]

T_g | Glass transition temperature, [K]
c | Degree of cure, [ ]

The model of T_g is based on data from Dynamic Mechanical Analysis (DMA) measurements. The DMA test are conducted on partially cured samples of fibre composite. [Jakobsen et al., 2013b] Hence, the model is not considered to yield accurate results for low degree of cure. However, the model is used after c_{gel} only, where it is assumed to sufficiently accurate.

5.4.2 Thermal and chemical strains

As shown by the result in section 3.3.3, the test specimen strains both thermally and chemically during the process. Both thermal and chemical strains occur before the gel point of the epoxy. However, when the epoxy is in the viscous phase, it is not considered to sustain any stress, because it requires a strain rate. Hence, the thermal and chemical strain is not expected to yield any in-plane stress or strain. Instead, the strain will cause a change in the thickness of the test specimen. In this project, the test specimen is modelled as a 2D structure, hence the strain before the gel point is disregarded.

The epoxy resin is assumed to have one coefficient of thermal expansion, α, below T_g, and another α above T_g. [Jakobsen et al., 2013a] This is also seen by the DIC measurements, described in section 3.3.3. The thermal expansion is thus assumed to be related to the temperature through a bi-linear relation. Hence, the thermal strain is modelled by equation (5.41).

$$\varepsilon_{therm}(T) = \begin{cases} 0 & \text{if} \quad c < c_{gel} \\ \displaystyle\int_{T_{gel}}^{T} \alpha\,(T, T_g)\mathrm{d}T & \text{if} \quad c \geq c_{gel} \end{cases} \tag{5.41}$$

where:

ε_{therm}	Thermal strain, [ ]
T	Temperature, [K]
T_{gel}	Temperature at which gelation occur, [K]
α	Coefficient of thermal expansion, $\left[\mathrm{K}^{-1}\right]$
T_g	Glass transition temperature, [K]
c_{gel}	Degree of cure at gel point, [ ]

α is given by equation (5.42).

$$\alpha\left(T, T_g\right) = \begin{cases} \alpha_{bT_g} & \text{if} \quad T \leq T_g \\ \alpha_{aT_g} & \text{if} \quad T > T_g \end{cases} \tag{5.42}$$

where:

α_{bT_g}	Coefficient of thermal expansion below T_g, $\left[\mathrm{K}^{-1}\right]$
α_{aT_g}	Coefficient of thermal expansion above T_g, $\left[\mathrm{K}^{-1}\right]$

Thermal mechanical analysis (TMA) has been used by Jakobsen et al. [2013a], to study the dimensional changes of the epoxy. By using the temperature modulation technique, the reversible and irreversible contribution is separated. The irreversible contribution, which is considered to be due to chemical shrinkage, shows a linear relation to the degree of cure. Hence, the chemical strain is assumed to be given by:

$$\varepsilon_{chem} = \begin{cases} 0 & \text{if} \quad c < c_{gel} \\ \beta(c - c_{gel}) & \text{if} \quad c \geq c_{gel} \end{cases} \tag{5.43}$$

where: [Jakobsen et al., 2013a]

ε_{chem}	Chemical strain, [ ]
β	Chemical shrinkage rate parameter, [ ]

The values of α_{bT_g}, α_{aT_g}, and β are given in table 3.1. The values obtained from the DIC measurements have been used in the model.

5.4.3 Young's modulus

The mechanical properties of the epoxy resin are highly dependent on temperature and the degree of cure. At high temperatures or at low degrees of cure, the stiffness is very low compared the fully cured epoxy at room temperature. In this section, it is described how the material properties, throughout the process, are estimated.

The material parameters are used for the elastic, pseudo-viscoelastic, and the full viscoelastic models. The elastic model is based on Young's modulus (E), whereas the viscoelastic models are based on a compliance modulus, described through a storage modulus (E') and a loss modulus (E''). When the storage modulus is small, the storage modulus and Young's modulus are considered to be approximately the same. Hence, in the elastic model, the storage modulus is used as the Young's modulus. The two terms are used interchangeably in the following.

Young's modulus of CSM glass fibre-epoxy composite

There is no model or experimental data available, describing Young's modulus as a function of temperature and degree of cure, for the epoxy system used in this project. However, Jakobsen et al. [2013b] presents a model of Young's modulus for a fibre composite. It is obtained from dynamic mechanical analysis (DMA) measurements on epoxy, reinforced with Chopped Strand Mat (CSM) E-glass fibres with a length of 50 mm. The fibre volume fraction of the samples is 0.25. The measurements are performed as tensile tests, where the distance between the clamps is 16-20 mm. The DMA measurements are conducted at a frequency of 1 Hz. The model of Young's modulus is fitted to the experimental data of isothermal DMA measurements, as a function of the temperature and cure history. [Jakobsen et al., 2013b] In this section, the model of the fibre composite is used to estimate the material properties of the epoxy matrix.

The model is given in equation (5.44).

$$E_{CSM}(c(t),T(t)) = E^0_{CSM} + \int_{t_{gel}}^{t} \frac{\partial E_{CSM}}{\partial t} dt + \int_{T_{gel}}^{T} \frac{\partial E_{CSM}}{\partial T} dT \tag{5.44}$$

where: [Jakobsen et al., 2013b]

E_{CSM}	In-plane Young's modulus for CSM composite, [Pa]
E^0_{CSM}	Initial modulus of CSM composite, before gelation, [Pa]
t_{gel}	Time at which gelation occur, [s]
t	Time, [s]

The derivatives of E_{CSM}, with respect to t and T, respectively, are given in equation (5.45)[1] and (5.46).

$$\frac{\partial E_{CSM}}{\partial t} = \begin{cases} 0 & \text{if} \quad c < c_{gel} \\ D_0 e^{-fT} \left(c - c_{gel}\right)^{b_1} \left(c_{max} - c\right)^{b_2} & \text{if} \quad c_{gel} \leq c \leq c_{max} \\ 0 & \text{if} \quad c_{max} < c \end{cases} \tag{5.45}$$

[Jakobsen et al., 2013b]

$$\frac{\partial E_{CSM}}{\partial T} = \begin{cases} 0 & \text{if} \quad c < c_{gel} \\ \dfrac{-\left(E_{subT_g} - E^0_{CSM}\right)\left(1 - \tanh\left(\omega\left(T - T_g\right)\right)^2\right)\omega}{2} & \text{if} \quad c_{gel} \leq c \end{cases} \tag{5.46}$$

where: [Jakobsen et al., 2013b]

D_0	Parameter in the model for the time derivative of E_{gf}, $\left[\frac{\text{Pa}}{\text{s}}\right]$
f	Parameter in the model for the time derivative of E_{gf}, $\left[\text{K}^{-1}\right]$
b_1	Parameter in the model for the time derivative of E_{gf}, [ ]
b_2	Parameter in the model for the time derivative of E_{gf}, [ ]
E_{subT_g}	Maximum attainable modulus at a given degree of cure, [Pa]
ω	Shaping parameter in the model for the temperature derivative of E_{gf}, [ ]

---

[1] This expression is slightly reformulated, but mathematically equal to the expression presented by Jakobsen et al. [2013b].

E_{subT_g} is the modulus at low temperatures, as a function of the degree of cure. It is given by equation (5.47).

$$E_{subT_g} = \begin{cases} E^0_{CSM} & \text{if} \quad c < c_{gel} \\ \dfrac{\left(E^{ult}_{CSM} - E^0_{CSM}\right)\left(1 + \tanh\left(\theta_{subT_g}\left(c - c_{1/2E_{ult}}\right)\right)\right)}{2} + E^0_{CSM} & \text{if} \quad c_{gel} \leq c \end{cases} \tag{5.47}$$

where: [Jakobsen et al., 2013b]

E^{ult}_{CSM}	Ultimate modulus of CSM composite, [Pa]
θ_{subT_g}	Shaping parameter in the model for E_{subT_g}, [ ]
$c_{1/2E_{ult}}$	Degree of cure at which half of the ultimate modulus has been obtained, [ ]

The parameters used in equation (5.44) to (5.47) are obtain by fitting the model to the experimental data and are given in table 5.3.

Parameter	Value
E^0_{CSM}	200 MPa
D_0	30.3 $\frac{\text{PPa}}{\text{s}}$
f	0.052 K^{-1}
b_1	3.68
b_2	0.78
ω	0.06
E^{ult}_{CSM}	13 GPa [2]
θ_{subT_g}	15
$c_{1/2E_{ult}}$	0.75

Table 5.3 Parameters used in the model for Young's modulus of CSM composite [Jakobsen et al., 2013b]

It is considered, that the model presented above can be used to estimate the mechanical properties of the neat epoxy resin, as a function of temperature and degree of cure. This is considered in the the following section.

Young's modulus of epoxy resin

The mechanical properties of a CSM composite can be expressed from the properties of the fibre and matrix material. If the properties of the composite are known, the expression can be reformulated to express the stiffness of the matrix material. In appendix E, an expression is derived, for Young's modulus of the epoxy matrix, as a function of Young's modulus of the E-glass fibre-epoxy composite, E_{CSM}. In the caluclation, the data given in table 5.4 has been assumed.[3]

---

[2] This value is obtained by reading of the graph in Fig. 3, Jakobsen et al. [2013b]

[3] Note that these data are general material data, they are not obtained by direct measurements on the specific materials of the composite.

Nomenclature	Description	Value
E_f	Young's modulus of E-glass fibre	70 GPa
ν_f	Poisson's ratio of E-glass fibre	0.22
ν_m	Poisson's ratio of epoxy	0.37

Table 5.4 Material properties of E-glass fibre and epoxy [Lund, 2013]

However, if the value of E_{CSM} is E^{ult}_{CSM}, equation (E.19) yields a Young's modulus of the epoxy matrix (E_m) of 6.9 GPa. This is more than twice the value of 3.2 GPa, given by the data sheet of the epoxy resin. [HEXION, 2008] If Young's modulus of the epoxy is assumed to 3.2 GPa, the reciprocal value of equation (E.14) yields E_{CSM}=5.4 GPa. This is far from the value of E^{ult}_{CSM}=13 GPa

Other methods have been attempted, in case the deviation is caused by an error in the equations of appendix E. The modified rule of mixture, equation (5.48), yields E_{CSM}=9.0 GPa.

$$E_{CSM} = \frac{3}{8} V_f E_f + E_m(1 - V_f) \tag{5.48}$$

[Rejab et al., 2008]

If it is solved w.r.t. the matrix modulus, it yields E_m=8.6 GPa.

The method presented by Christensen and Waals [1972] yields E_{CSM}=10 GPa and E_m=5.6 GPa, respectively. Hence, this method yields the best result, of the methods which has been attempted. However, it is not considered to be sufficiently accurate.

Ghosh [2004] presents experimental data of an E-glass CSM-epoxy composite, with a fibre volume fraction of 0.255, and a Young's modulus of 7.6 GPa. Campbell [2010] presents data of an E-glass CSM-epoxy composite as well, with a fibre volume fraction of 0.20, which also has a Young's modulus of approximately 7.6 GPa. However, as the properties of the matrix material in these examples are unknown, not too much should be read into the values.

It is not known for sure, why Young's modulus of the epoxy matrix is overestimated, when it is calculated from the model of E_{CSM}. However, it might be due to the basic assumptions used in appendix E, and the other methods which has been applied, which might not correlate with the experimental set-up, used to obtain the stiffness of the composite.

It might be that the distance between the clamps is too small. If some fibres are fixed by the clamps in both ends, they might form a stiff link between the clamps which is independent on the matrix stiffness. This is implied to have an effect, due to the existence of the parameter E^{0}_{CSM}, which is the initial modulus of the composite, before gelation, when the matrix stiffness is zero. In the case of the theoretical method, the stiffness of the composite is zero, when the matrix stiffness is zero. However, because E^{0}_{CSM} is small compared to E^{ult}_{CSM}, this is not assessed to have a large effect at high moduli.

It could also be due to an uneven fibre distribution through the thickness. If the fibres are clotted together, to form a layer with a higher fibre volume fraction, surrounded by layers with a low volume fraction, the effective stiffness would be increased. However, it is not considered to be likely, that the fibres are clotted together that extensively, to cause the disagreement.

At last, a reason could be a viscoelastic effect. The tests on the CSM fibre composites are conducted at a frequency of 1 Hz. The value which is measured from the experiment is the storage modulus, which is assumed to be equal to the static Young's modulus. If this assumption is invalid, Young's modulus of the composite, predicted by the model, might be too high.

Regardless the reason, the value of E_m, obtained by equation (E.19), is assessed to be overestimated. Hence, it is not used. However, in figure E.2, it is seen that there is a nearly linear relation between E_m and E_{CSM}. This linear relation is assumed to be valid, by which E_m is assumed to be determined by a linear scaling of equation (5.44). Hence, the storage modulus of the epoxy resin is approximated by equation (5.49).

$$E_m(c(t), T(t)) = \frac{E_m^{ult}}{E_{CSM}^{ult}} E_{CSM}(c(t), T(t)) \tag{5.49}$$

where:

E_m	Young's modulus of the matrix material, [Pa]
E_m^{ult}	Ultimate modulus of epoxy matrix, [Pa]

A value of E_m^{ult}=2.75 GPa yields reasonable results in the comparison, presented in the following section. Hence, this value is used in the model.

Comparison of Young's modulus from model and experimental measurements

In the following, Young's modulus predicted by the model is compared with experimental data. The experimental data is obtained by DMA measurements, conducted by Johnny Jakobsen, on a neat epoxy sample.

At first, Young's modulus from the model is compared with DMA measurements of a fully cured epoxy sample, which is subjected to a temperature ramp. The model data is based on equation (5.44) and (5.49), which is applied to a simulated temperature profile of 120 °C for 10 hours, to ensure a complete curing, and afterwards cooled down to 20 °C. The experimental data and the model is compared in figure 5.3, which shows the cool-down only.

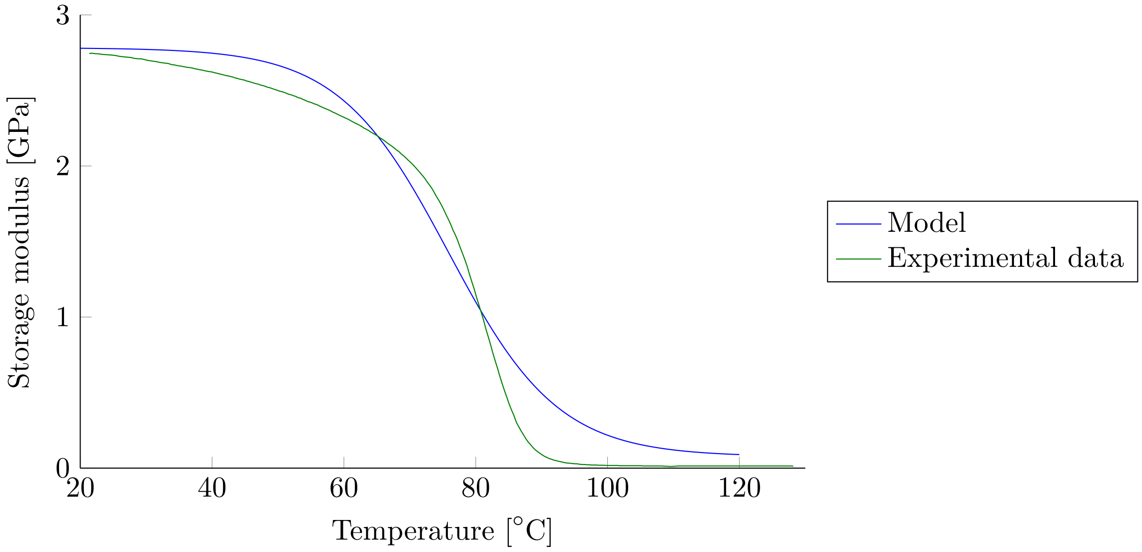

Figure 5.3 Comparison of storage modulus from model and experimental data, for fully cured epoxy.

Next, Young's modulus from the model is compared with experimental data of an epoxy sample which is considered during the cure. The experimental data is obtained by DMA measurements on an an uncured epoxy sample, which is kept at a constant temperature of 80 °C. The modelled data is obtained by calculating the degree of cure according to equation (5.3), which is applied in equation (5.44) and (5.49). In figure 5.4 the experimental and modelled data is compared. As seen, there are two experimental datasets. These are based on the same process parameters.

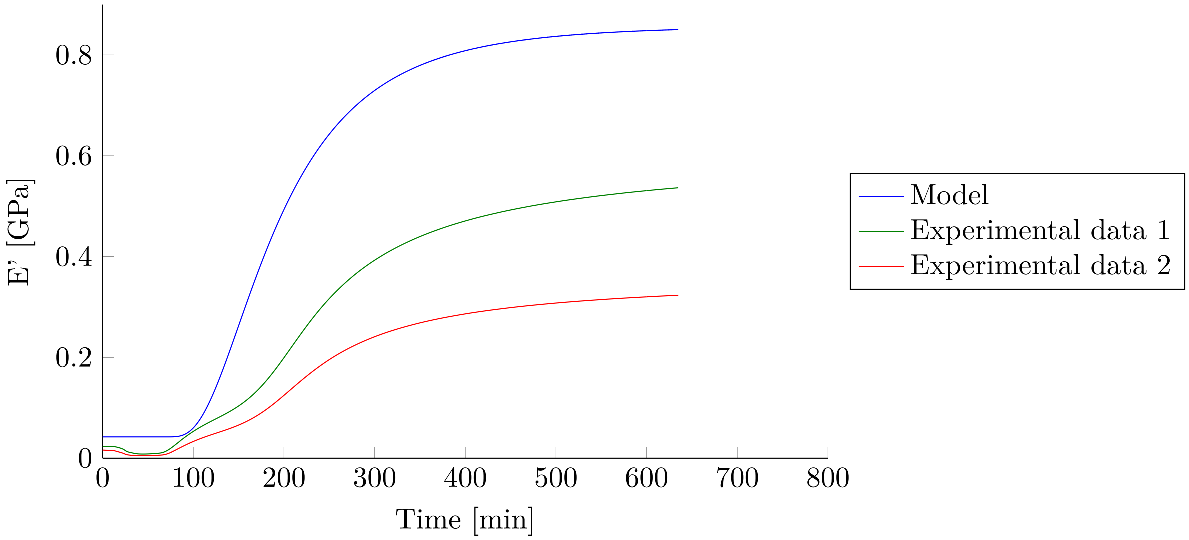

Figure 5.4 Comparison of storage modulus during the cure at constant temperature of 80 °C, from model and experimental data.

As seen above, there is reasonable correlation in figure 5.3. However, in figure 5.4, there is not good correlation. Even in the two experimental datasets, which are supposed to be equal, there is inconsistency. It is assessed that the model deviates from the experimental data, because T_g of the material approach the curing temperature. Because the modulus is highly temperature dependent, near T_g, small inaccuracies yield large deviation. As seen in figure 5.3, there is a large slope in this temperature range, hence the value of Young's modulus is assessed to be highly sensitive to inaccuracies in the model.

In spite of the deviation, it is assessed that the model is applicable in the model for the test specimen, considered in this project.

Loss modulus of epoxy resin

There is no model available for the loss modulus of either the CSM composite or the epoxy resin. However, from the DMA measurements, conducted by Johnny Jakobsen, on the fully cured epoxy sample (experimental data in figure 5.3), both the storage and loss modulus are determined. These are shown in figure 5.5.

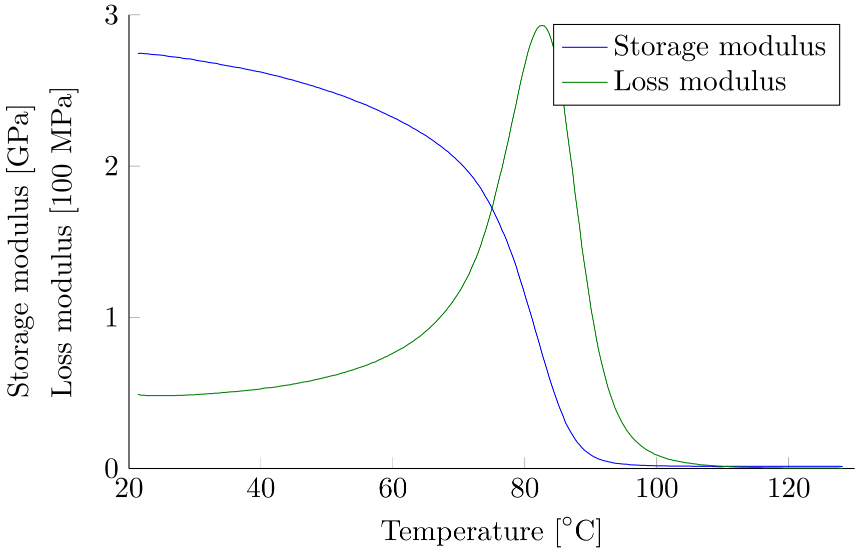

Figure 5.5 Experimental data of storage and loss modulus of fully cured neat epoxy as a function of temperature.

In figure 5.6, the loss modulus is plotted as a function of the storage modulus.

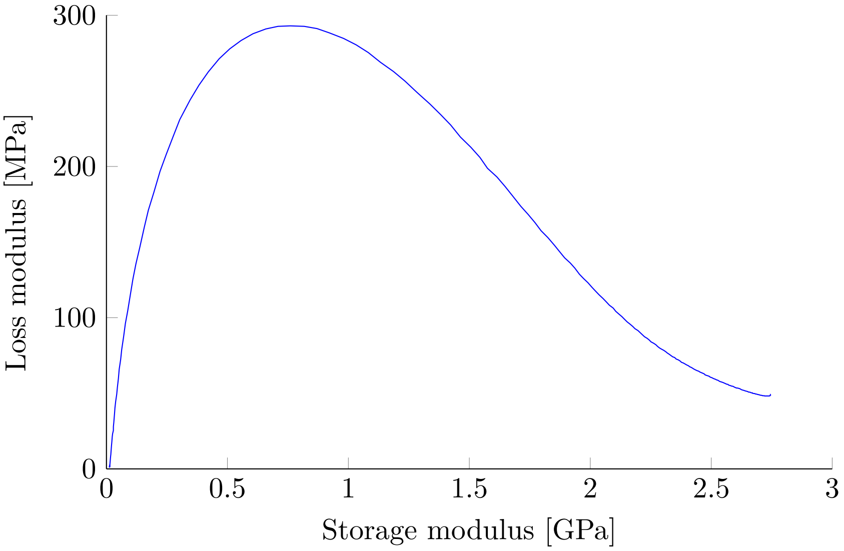

Figure 5.6 Loss modulus as a function of the storage modulus, from the experimental data in figure 5.5.

It is assumed, that the relation between the loss and storage modulus, shown in figure 5.6 is applicable for the epoxy resin, throughout the curing process. Hence, the graph in figure 5.6 is combined with the model of the storage modulus, to obtain a model of the loss modulus.

In figure 5.7, the model of the loss modulus is compared with the experimental data, from the measurements on the fully cured sample.

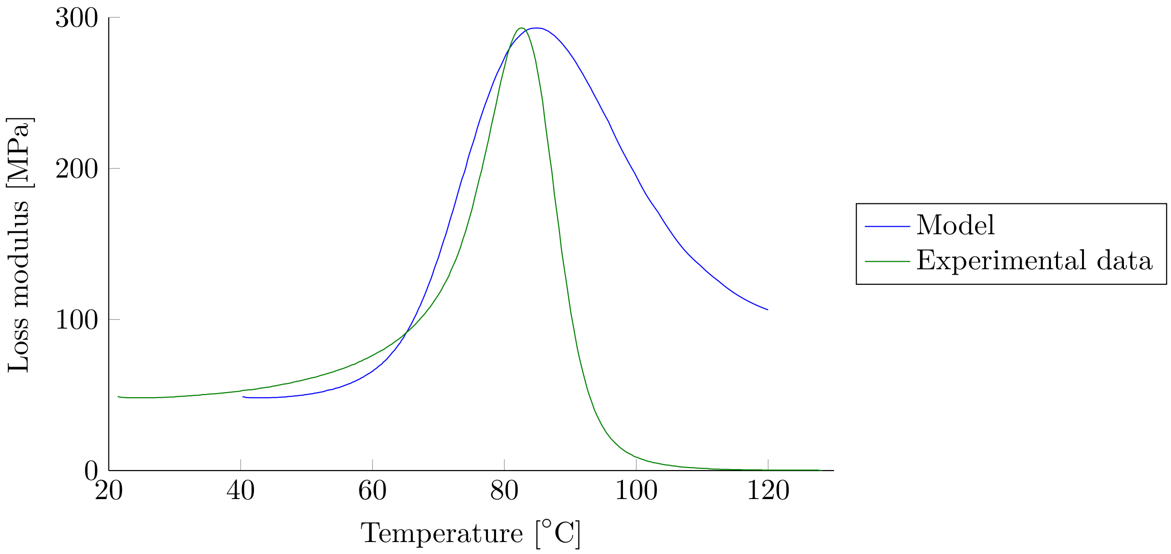

Figure 5.7 Comparison of loss modulus from model and experimental data, at constant degree of cure.

In figure 5.8, the model is compared with the experimental data, from the measurements on the sample during curing.

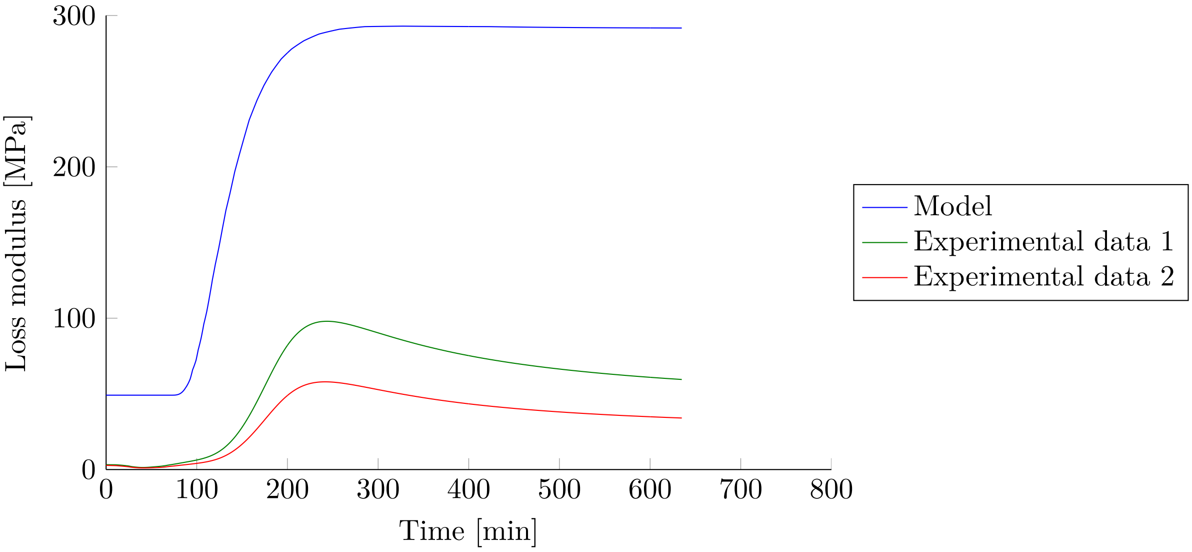

Figure 5.8 Comparison of loss modulus from model and experimental data, at a constant temperature of 80 °C.

As with the storage modulus, there is a fair correlation between the model, and the experimental data of the fully cured sample, shown in figure 5.7. However, there is not good correlation with the experimental data of the sample at constant temperature, shown in figure 5.8.

5.5 Pseudo code of implementation

In this section, it is described how the entire model is implemented, by presenting a pseudo code. The entire FEM model is coded in MATLAB, by the author of this project. The code is appended on the appendix CD, appendix I.

The model is based on 4-node, isoparametric elements with full integration. The elements are formulated according to according to Cook et al. [2001] chapter 6. To take the instantaneous compliance into account, $[M]$ (equation (5.39)) is used as the constitutive relation. Hence, the tangent stiffness matrix is obtained.

At first the geometry is discretised by defining the mesh. In figure 5.9, the meshed geometry is seen.

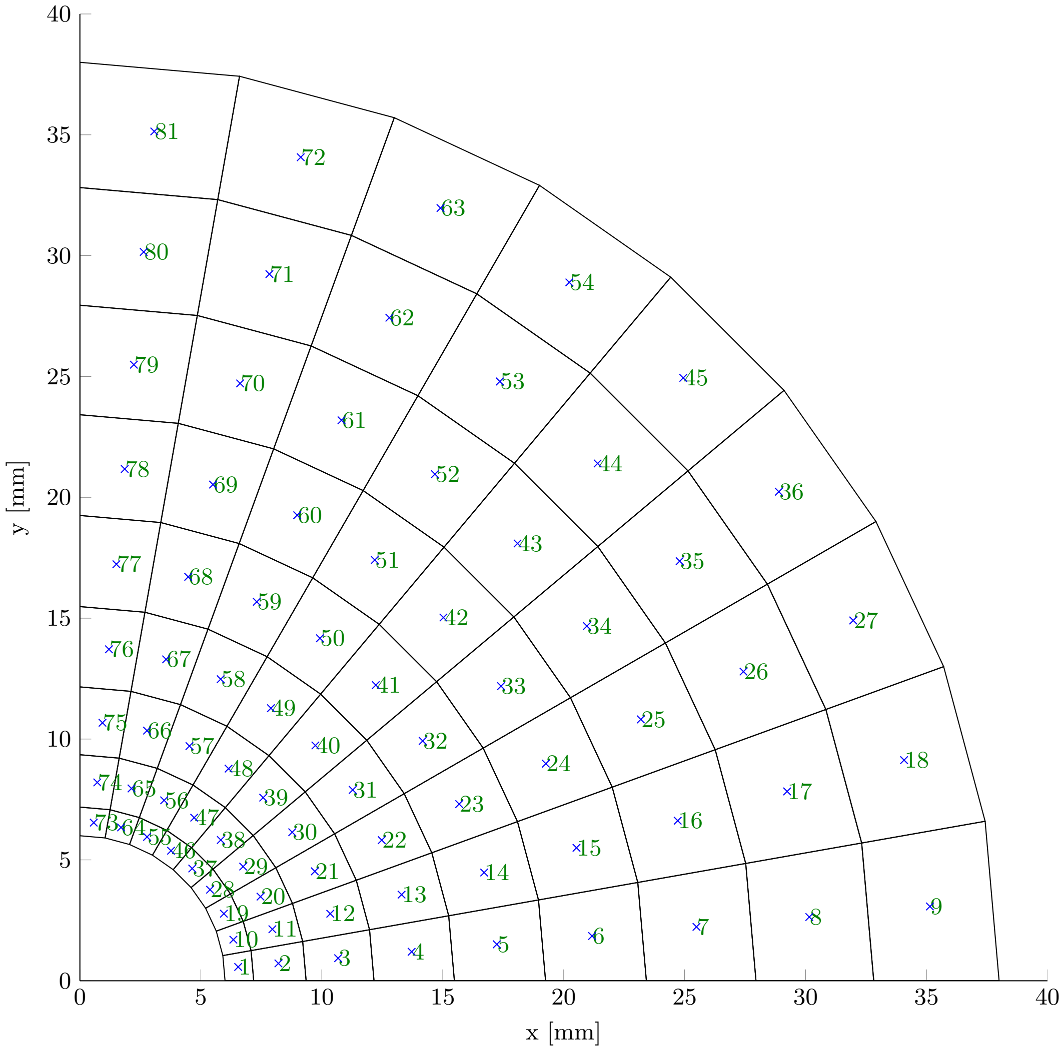

Figure 5.9 Meshed geometry with element numbers

Because the stress gradient is greater near the insert, the mesh is made finer in this area. This is assessed to cause a more accurate result with fewer elements, and thus less computational time.

Only a quarter of the geometry is modelled. Hence, symmetry boundary conditions are applied at the left and lower boundaries. The boundary at the insert is prescribed a displacement, due to the thermal expansion of the steel insert. A coefficient of thermal expansion of 11.7 $\frac{\mu\mathrm{m}}{\mathrm{mK}}$ for carbon steel is used [Andersen et al., 2007].

The time is discretised into a number of time steps of equal size. It is assessed, that an uneven time discretisation, with small time steps at large temperature gradients, would improve the efficiency of the model. However, it is considered to be beyond the scope of this project. The time range is determined by the data from the temperature measurements.

The number of elements and time steps are determined through at convergence study. As shown in appendix G, 9x9 elements and 1000 time steps yields a reasonable result.

The variables which are used are initialised, after which the model iterates over each time step.

```
Loop over each time step
  • Temperature at current time step is defined by interpolation of the temperature measurements (figure 3.3 or 4.8)
  • The degree of cure is estimated according to equation (5.3).
  • If $c > c_{gel}$
      – Calculate chemical strain according to equation (5.43)
      – Calculate thermal strain according to equation (5.41)
  • Calculate instantaneous compliance, $D_I$, according to equation (5.7), (5.17), (5.24), or (5.32)
  • The matrix $[M]$ is calculated according to equation (5.39)
  • Loop over each element to obtain tangent stiffness matrix
      – Calculate hereditary strain, $\varepsilon^H$ according to equation (5.8), (5.18), (5.25), or (5.33)
      – Calculated element tangent stiffness matrix.
      – Include element matrix in global tangent stiffness matrix, $[K_t]$
  • If $c > c_{gel}$ [4]
      – Apply displacement to boundary at insert, due to thermal expansion of the steel.
  • Initialise nodal displacement as $\{u_i\} = \{u_{i-1}\}$
  • Iterate to solve for displacements, while $\frac{||\{\Delta u_i\}||}{||\{u_i\}||} > \mathrm{TOL}$ [Henriksen, 1984]
      – Loop over each element to obtain nodal load vector
          ∗ Calculate mechanical strain, $\{\varepsilon^m\}$. Total strain is calculated from $\{u_i\}$, according to Cook et al. [2001] chapter 6, and subtracted $\varepsilon_{therm}$ and $\varepsilon_{chem}$ to obtain $\varepsilon^m$.
          ∗ Calculate $\sigma$ according to equation (5.38)
          ∗ Calculate nodal loads, $\{R\}$, from $\{\sigma\}$, according to Cook et al. [2001] chapter 6.
      – Calculate increment in nodal displacement $\{\Delta u_i\} = -[K_t]\backslash\{R\}$
      – Update nodal displacement vector $\{u_{i+1}\} = \{u_i\} + \{\Delta u_i\}$
```

---

[4] It is assumed that any displacement of the boundary before the gel point causes viscous flow only, and hence no mechanical strain or stress.

Part III

Results and Conclusion

In chapter 6, in this part, the results of the numerical model, described in part II, are presented. The experiments, presented in part I, based on digital image correlation (DIC) and photoelasticity are simulated, using the numerical model. The experiments are simulated, using the different material model, and compared with the experimental results.

Future work is discussed in chapter 7 and in the end, the project is concluded in chapter 8.

Results 6

In this chapter, the simulated results, from the models described in chapter 5, are presented. The results are furthermore compared with the results obtained by DIC measurements and photoelastic experiments, as described in part I.

6.1 Average strain

At first, the model is evaluated to consider the strain results. Hence, the temperature measurements from the DIC experiment, seen in figure 3.4, are used as the temperature profile.

All four models, which are considered, yield almost the exact same strain result. This is assessed to be because the model is loaded by prescribed volumetric strains and displacements of the boundary, only.

In figure 6.1, the average strain from the model and the experimental data from the DIC measurements (section 3.3.1) is shown. The strain from the experimental data is calculated w.r.t. to the deformation state at the gel point.

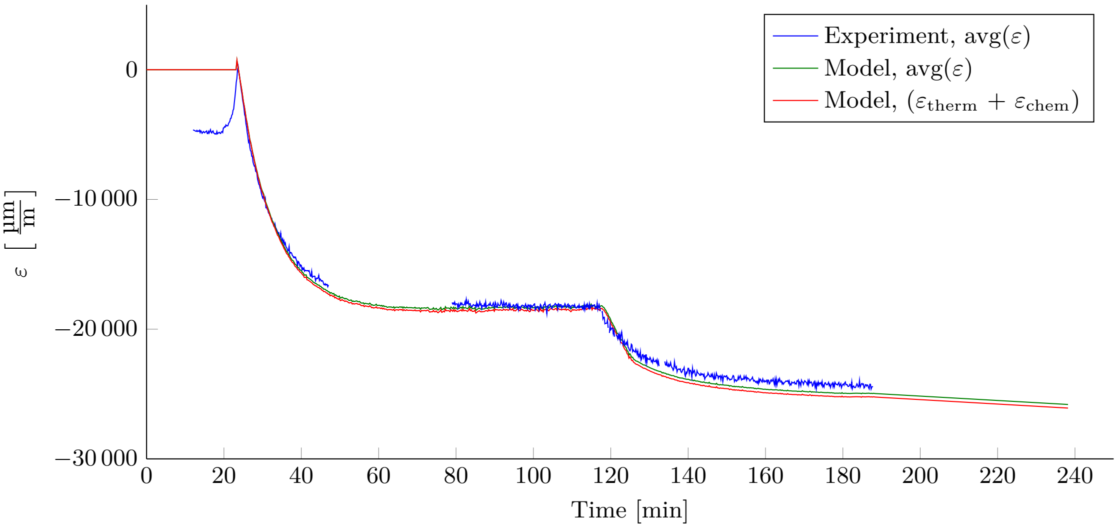

Figure 6.1 Comparison of average strain from experimental data and model

In the figure, the modelled data is given as the average of the total strain, and as the sum of thermal and chemical strain. As seen, there is very little difference. From this, it is concluded, that the mechanical strain has little influence on the average strain. Hence, the assumption used in section 3.3.3, that the average strain is the sum of chemical and thermal strain, is considered to be valid.

It is seen in figure 6.1, that there is very good correlation between the experimental data and the model. Thus, the model is capable of modelling the average strain accurately.

For comparison, the process has been simulated, using the parameters from Jakobsen et al. [2013a] in table 3.1. The result is compared with the experimental data in figure 6.2.

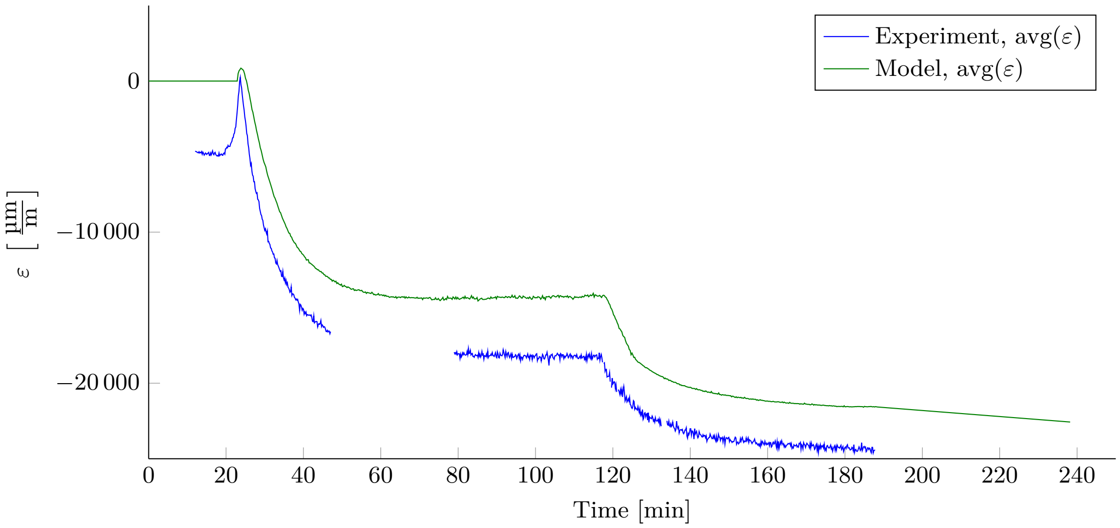

Figure 6.2 Comparison of average strain from experimental data and model, where the model is based on parameters from Jakobsen et al. [2013a]

As seen, these parameters do not yield as good correlation with the experimental data. The deviation is primarily caused by the model of the chemical shrinkage. This is shown in figure 6.3, where the thermal, chemical, and average mechanical strain is shown, for simulations based on the parameters obtain from the DIC measurements, and those presented by Jakobsen et al. [2013a].

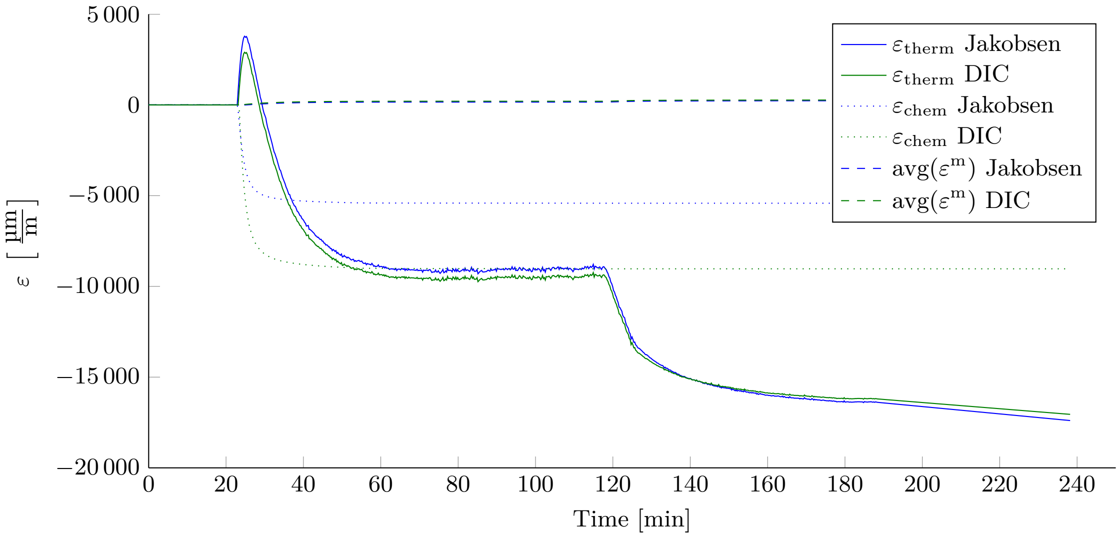

Figure 6.3 Comparison of thermal, chemical, and mechanical strain, based on parameters from DIC measurements and Jakobsen et al. [2013a], respectively.

However, the parameters of the model based on DIC are obtained from the same experimental dataset, as the model is compared with. This might be the reason, why it yields better correlation with the experimental data. It might be that that the inconsistency in the temperature measurement is indirectly taken into account by the model of the chemical strain.

6.2 Stress

In the following, the stress results are considered. Hence, the model is based on the temperature measurements of the photoelastic experiment. The temperature profile is for the slowly cooled test specimen, seen in figure 4.8.

In figure 6.4, the principal stress difference due to residual stress at the end of the process, is given for the four models. Furthermore, the experimental result is given, from the slowly cooled test specimen in figure 4.17.

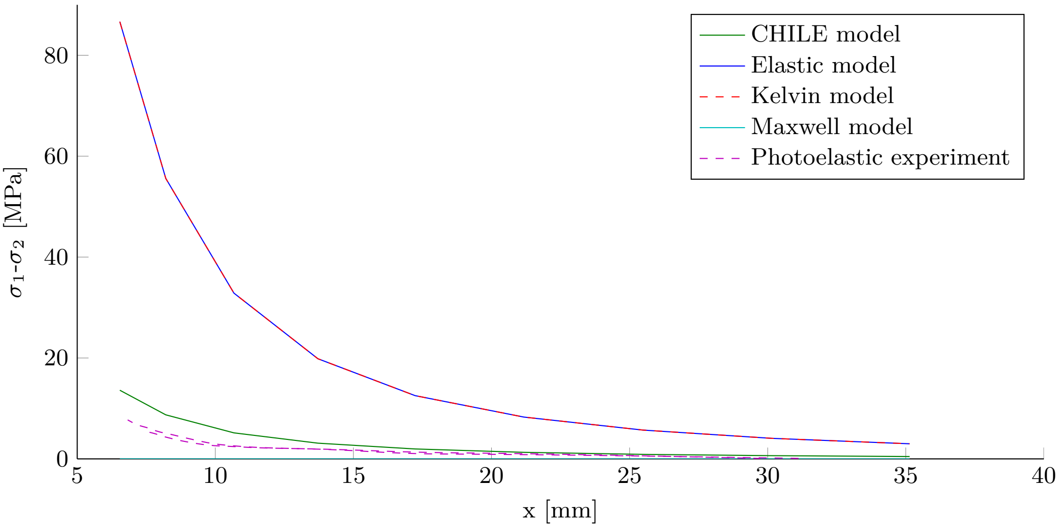

Figure 6.4 Principal stress difference, from four different models and photoelastic experiment, along radial line

As seen, only the stress field on the right side of the test specimen is shown. Hence, the experimental data from the left side has been mirrored, and is shown in the same plot.

The elastic and the Kelvin model yield almost exactly the same stress, however, both overestimates the experimental data by far. As seen in equation (5.5) and (5.22), the only difference is the strain rate depend term in the Kelvin model. At the end of the process, the test specimen reaches a steady state, where the strain rate is zero. Hence, the two models yield the same result.

The Maxwell model yields a very low stress. It is approximately a thousandth of the experimental result. When a 1D model of a Maxwell material is applied a step input on strain at t=0, the stress is relaxed as seen in equation (6.1).

$$\sigma(t) = \varepsilon E e^{-\frac{E}{\eta}t} \tag{6.1}$$

where: [Schjødt-Thomsen, 2005]

σ	Stress, [Pa]
t	Time, [s]
ε	Strain, [ ]
E	Young's modulus, [Pa]
η	Viscosity, $\left[\frac{\text{kg}}{\text{sm}}\right]$

At $t = 0$, this yields the elastic solution. The time at which the stress is reduced to half of that is solved from equation (6.1) and is given in equation (6.2).

$$t_{\frac{1}{2}} = \frac{\eta \ln\left(\frac{1}{2}\right)}{E} \tag{6.2}$$

E and η is determined from equation (5.20) and (5.21), where the storage and loss modulus is read off figure 5.5 at room temperature to 2.75 GPa and 48.6 MPa respectively. This yield a time of $t_{\frac{1}{2}} = 6.2\,\text{s}$. This mean, that the stress is reduced to half every 6.2 s, even at low temperatures. Considering the time range of the experiment, it is understandable why this model yields very low stresses.[1] However, it is not considered to be the correct representation of the material.

The elastic and the Kelvin models are assessed to overestimate the stress, because they do not take the viscoelastic effect into account, to a sufficient extent. The Maxwell model is assessed to underestimate the stress, because it allows the material to relax too fast, at room temperature.

The CHILE model, on the other hand, yields results in the right order of magnitude. In figure 6.5, the result of the CHILE model and the photoelastic experiment is repeated, with a more suitable scale. Furthermore, the relative deviation is evaluated, at the element centres, w.r.t. the average of the two graphs of experimental results.

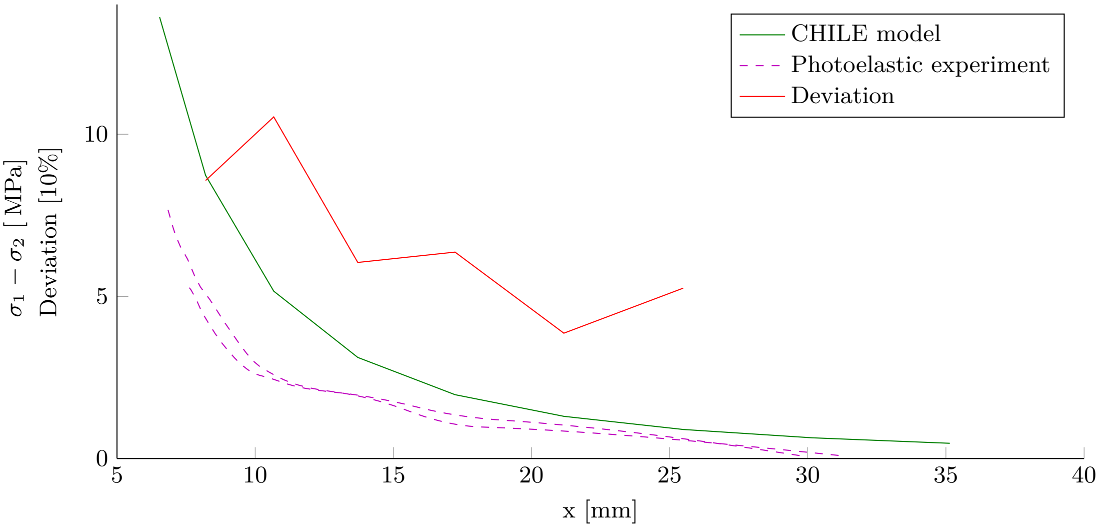

Figure 6.5 Principal stress difference, from CHILE model and photoelastic experiment, along radial line. Furthermore, the relative deviation is shown.

It is seen, that there is a fair correlation between the two dataset, with a relative deviation of 105 %, at most. The relative deviation appears to be larger at higher levels of stress. Hence, the disagreement cannot be explained by the value on D_{CHILE} alone. It might be because the stress is relaxed at a higher rate, at higher stress levels, which the model does not take into account. Or it could be due to the assumption of an even temperature throughout the test specimen. Furthermore, the deviation could be due to the assumption of plane stress, which is not valid at the boundary of the insert. However, this is only assessed to have a significant effect near the insert. At last, the deviation could simply be due to inaccuracies in the photoelastic measurements.

---

[1] Furthermore, it is suspected, that there might be an implementation error, because the model tend to yield unstable stress results.

However, the result of the CHILE model is dependent on the frequency, at which the instantaneous compliance, D_{CHILE}, is obtained. In this case, it is obtained at a frequency of 1 Hz. According to Zobeiry [2006], the frequency should be ”relatively low”, e.g. 0.1 Hz. It is considered that D_{CHILE} would decrease, and hence improve the accuracy of the model, if the frequency is decreased, however, the extend is unknown.

6.3 Stress-free temperature

According to the early methods, used to model process residual stress in composites, e.g. Hahn and Pagano [1975], the structure is completely stress-free at the temperature of curing. Hence, the elastic model is combined with this assumption. It is implemented, by disregarding every stress and strain occurring before a certain time in the process[2]. By assuming the test specimen to be stress-free at 63 °C and 82 °C, the elastic model agrees with the experimental data and the CHILE model, respectively. This is shown in figure 6.6.

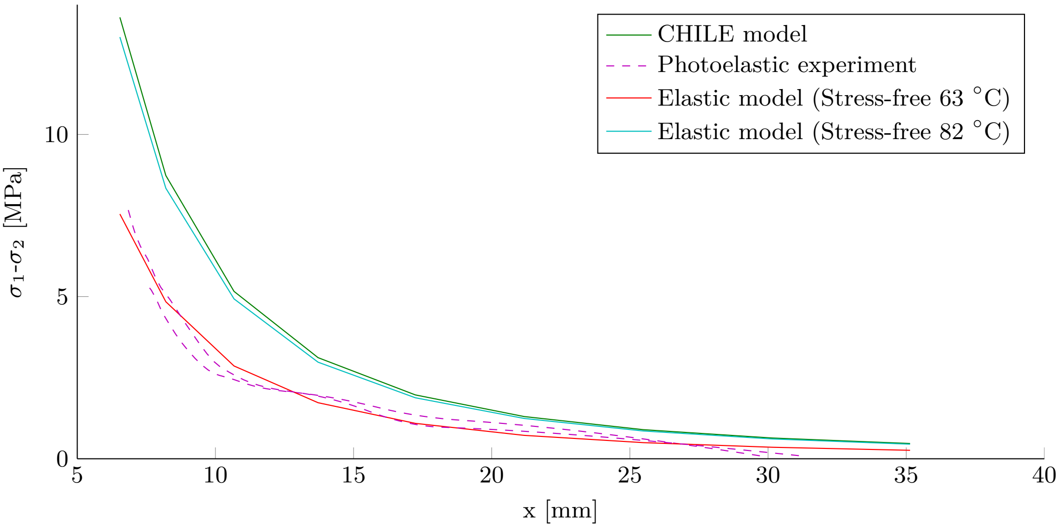

Figure 6.6 Principal stress difference photoelastic experiment, along radial line, compared with elastic model, where a stress free temperature is assumed.

The assumptions of the two different stress-free temperatures yields a very good fit to the experimental data and the CHILE model. However, the stress-free temperatures are not based on a physical consideration, it is merely a ”curve fit”. The temperatures of 63 °C and 82 °C are both well below the process temperature of approximately 100 °C, as seen in figure 4.8.

However, the temperatures are on either side of the glass transition temperature, which is 76 °C for fully cured epoxy, according to equation (5.40). Hence, it is plausible that there is a relation between the residual stress and T_g, by which the stress can be modelled by assuming a stress-free temperature. This hypothesis could be tested by conducting the experiment at different temperatures. Hence, it can be studied whether the residual stress is independent on the process temperature.

---

[2] It is not physically accurate, that no strain occur before this certain time, however, it is considered to be the simplest way to implement the assumption of a stress-free temperature.

6.4 In-situ stress

In figure 6.7, the principal stress difference is shown as a function of time, evaluated at an element at the boundary of the insert. The stress is obtained by using the CHILE model, the elastic model, and the elastic model with two different assumptions of stress-free temperatures.

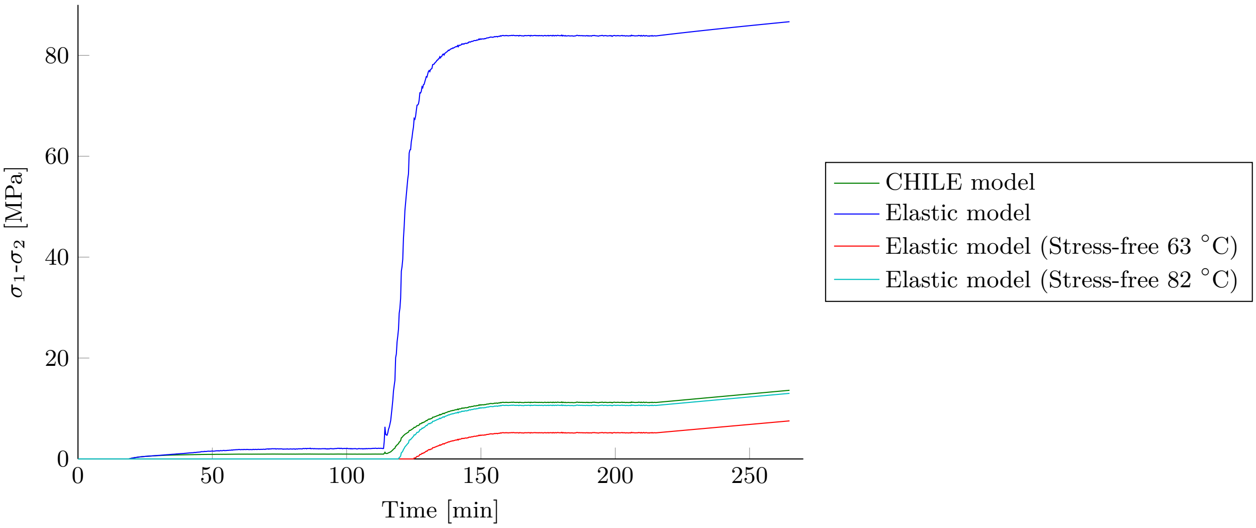

Figure 6.7 Principal stress difference at an element near the insert as a function of time, according to four different models.

As seen, the elastic model has a significant increase in the stress level at approximately 115 min. This is considered to be primarily due the change in Young's modulus. According to the elastic model, strains occurring early in the process, when Young's modulus is low, yield stresses when test specimen cools. This is not the case with the other models in figure 6.7.

In figure 6.8, the data of figure 6.7 is shown as a function of temperature.

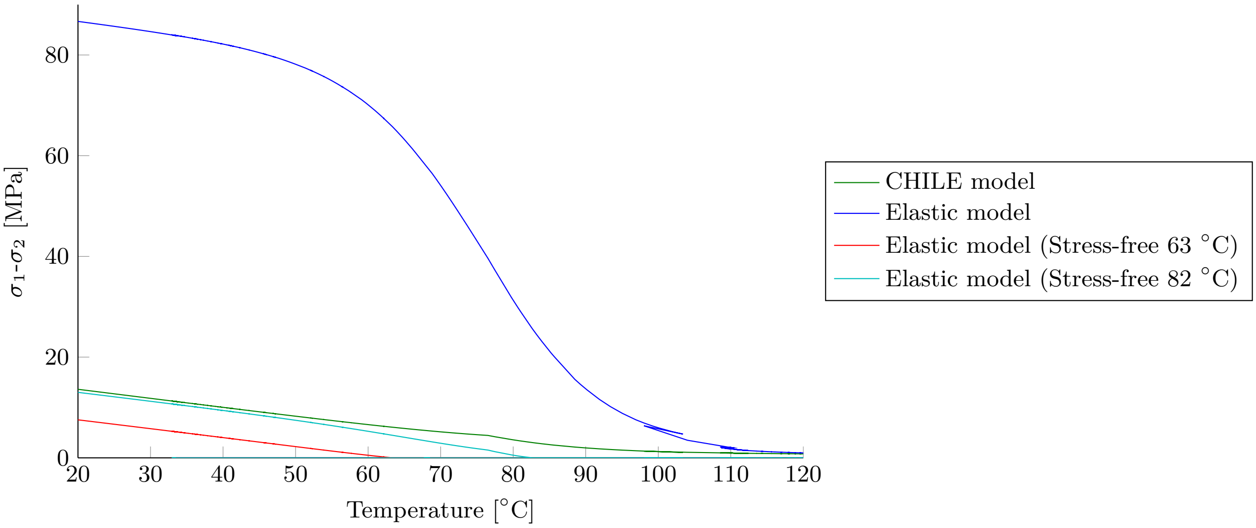

Figure 6.8 Principal stress difference at an element near the insert as a function of temperature, according to four different models.

There is a noticable similarity between the CHILE model, the models with a stress-free temperature in figure 6.8, and the experimental data of the fringe order during cool down in figure 4.32.

As illustrated in figure 4.6, the fringe constant is nearly constant at temperatures below T_g. Hence, there is expected to be a nearly linear relation between the graphs of figure 4.32 and the principal stress difference, by which the principal stress difference is expected to be approximately linearly dependent on the temperature. In figure 6.8 it is seen, that the CHILE model and the two models with the assumptions of a stress-free temperature yields a nearly linear relation between the stress and temperature, below T_g. The elastic model however, yields a non-linear relation.

6.5 Summary

All four material models, which have been implemented in the model, yield almost exactly the same strain result. The results have a very good correlation with the experimental DIC measurements. It is furthermore shown, that the parameters obtained through the DIC measurements, given in table 3.1, yields better results than the parameters obtained from Jakobsen et al. [2013a]. This is primarily due to the modelling of the chemical strain.

There is a large difference in the accuracy of the modelled stresses. The elastic model overestimates the stress considerably. This is because the model does not include the viscoelastic effects, which are assessed to have great influence at elevated temperatures. However, the two viscoelastic models do not yield better results. The Kelvin model yields almost the exact same result as the elastic model, and the Maxwell model yields a very low stress level. It is considered that both the Kelvin model and the Maxwell model are too simple to model the system. It is furthermore considered, that more experimental material characterising is necessary.

The CHILE model yields very promising results. It has a deviation of approximately 100 %, w.r.t. the experimental result. It is considered, that the accuracy can be improved by basing it on DMA measurements at lower frequency.

By combining the elastic method with the assumption of a stress-free temperature, good results are obtained. However, it is considered that stress-free temperature is rather the glass transition temperature than the process temperature, as e.g. Hahn and Pagano [1975] suggest. This, however, requires more experiment to conclude.

Future work 7

In this project, a very simple test specimen is considered. To be able to use the numerical model for designing actual structures, it must be further developed.

It is considered, that the model should be expanded to 3D, for most practical purposes. This is considered to be fairly simple. The present model is based on uni-axial material models, which are expanded to 2D as described in section 5.3.4. By replacing $[V]$ in equation (5.35), with the full 6x6 matrix, which can be obtained from Hook's law, the material model can be expanded to 3D. Furthermore, it is required to implement a 3D solid element in the finite element code.

In the model, the temperature is assumed to be the same, throughout the test specimen. This assumption is considered to be rather doubtful, because the experiment presented in appendix A shows a temperature variation through the thickness. If the model were to be used on a structure, such as the root section of a wind turbine blade, as seen in figure 1.1, the assumption would be too crude. Hence, it is considered necessary to include a model of the thermal heat flow in the system, to predict the temperature distribution. This model should, apart from the internal heat flow, include heat from the exothermic chemical reaction of curing and heat flow through the boundaries of the model.

By including the thermal model, the degree of cure, the instantaneous compliance, and the volumetric strain can be calculated at each element in the model.

To simulate the root section in figure 1.1, it is furthermore necessary to include the effect of fibres in the model. It is considered, that the approach of this project can be used to model the epoxy resin, after which it can be included in a micro mechanical model to include the fibres. However, this requires some further study.

It is considered, that the model cannot only be used to improve the mechanical design of a structure, but also the manufacturing process. By conducting simulations with various temperature profiles, the effect on the residual stress and mechanical properties can be studied. E.g. by curing at a lower temperature, the process requires more time, and the epoxy might not be fully cured and obtain the potential mechanical properties. However, if it yields less residual stress, the overall load carrying capabilities of the structure might be improved.

Even though the CHILE model yields reasonable results, it is required to conduct more experiments, to validate the model. Alternatively, the viscoelastic properties of the epoxy resin can be characterised further through an experimental study. From this, it might be possible to obtain a more accurate visoelastic model, which can be used to simulate the system.

Conclusion 8

In this project, process induced residual stress is considered for a thermosetting polymer test specimen with a metallic insert. The stress and strain is considered, during the process, by using experimental and numerical methods.

The test specimen, which is considered throughout the project, is a circular disc of epoxy resin with a cylindrical steel insert in the centre. The test specimen is cast in a silicone mould, which is designed to be very compliant. Hence, the test specimen is considered to have free boundary condition throughout the process.

Experimental measurements of the in-situ strain field in the top surface of the test specimen are conducted, by using digital image correlation (DIC). Hence, a method for applying an adequate surface pattern to the uncured epoxy test specimen has been developed. Several approaches have been tested, where a surface pattern based on expanded perlite with speckle of black spray paint yields reasonable results.

The in-situ DIC measurements are conducted, by placing the uncured test specimen in an oven, with a transparent lid. Hence, the cameras of the DIC system can capture the deformation of the test specimen, during the process. However, the measurements are not sufficient to obtain the local strain field around the insert. Hence, only the average strain throughout the surface of the test specimen is considered.

The difference between the average strain in the x and y direction yield a good measure for detecting gelation of the test specimen. When the difference between the two components of the strain becomes constant, the test specimen is considered to have reached the gel point. However, this approach is only considered to be valid because the test specimen has two symmetry planes.

The DIC measurements of the average strain in the test specimen are considered to resemble the sum of thermal and chemical strain. By combing this data with temperature measurements and the model for the degree of cure, the average strain is separated into the thermal and chemical contribution. From this, the coefficient of thermal expansion is determined for temperatures below the glass transition temperature, T_g, and for temperatures above T_g. Furthermore, the chemical strain rate, w.r.t. the degree of cure is determined.

However, because the temperature is measured at the bottom of the test specimen, whereas the strain is measured at the top, a significant error is introduced. However, the influence of this error has not been quantified.

Photoelasticity has been applied to evaluate the residual stress field of the test specimen. However, the stress-optical law turns out not to be valid, because the structure is loaded, while the temperature is above T_g.

To determine the residual stress, a method is developed which is based on insert removal. By considering the difference in the optical fringe pattern in the test specimen, before and after the insert is removed, the difference in principal stress difference is determined. Because the test specimen is considered to be stress-free, after the insert is removed, the difference in stress is considered as the process induced residual stress. This method is considered to be a good approach for measuring the residual stress, in the test specimen considered in this project.

Furthermore, photoelasticity is used to study the test specimen during the process. It is determined, that the fringe order is nearly linearly dependent on the temperature, during cooling. However, because the stress-optical law is not valid for this case, the measurements are not processed into stresses.

A numerical analysis is conducted on the stress and strain in the test specimen. The numerical model is a non-linear multi physical model, based on the finite element method (FEM). The model includes the chemical reaction, when the epoxy resin cures, and the structural deformation and stress in the test specimen, due to process induced volumetric changes. The physical problem furthermore includes thermal heat transfer, however, this has not been included in the model.

The numerical model is made in different versions, based on elastic, viscoelastic, or pesudo-viscoelastic material models. The models are implemented in non-linear FEM code, which is written in MATLAB during this project.

The model is based on the material properties of the epoxy resin, formulated as the storage modulus (E') and the loss modulus (E''). E' and E'' are modelled as a function of the temperature and cure history. The model of E' is based on an existing model of the storage modulus for a chopped strand mat (CSM) E-glass epoxy composite, which is modified to yield E' for the neat epoxy. The relation between E' and E'' is established from experimental data of an dynamic mechanical analysis (DMA).

Four different material models have been applied. The elastic model, which is based on thermoelastic considerations, predicts considerably larger stress than the photoelastic experiment. This model is considered to be too simple, to predict the stress field of this system. However, by combining the elastic model with the assumption of a stress-free temperature, the stress field can be fitted to the experimental data. It is hypothesised, that the stress-free temperature is related to T_g, however it requires more experimental data to conclude.

The Kelvin model, one of the viscoelastic models, yields a stress field which is almost equal to the stress field of the elastic model.

The other viscoelastic model, the Maxwell model, yields almost no stress. Even at room temperature, this model predicts a high degree of relaxation.

It is concluded, that neither of the viscoelastic modes are sufficient to model the viscoelastic behaviour of the test specimen.

The pseudo-viscoelastic model, which is considered in this project, is the cure hardening instantaneously linear elastic (CHILE) model. It yields results, which deviates 105 % from the photoelastic measurements, where the deviation is largest. This is considered to be a good result in proportion to the simplicity of the model.

All four material models yield very similar strain results. The averages strain is clearly dominated by the thermal and chemical strain, and yield very good correlation with the DIC measurements. This might be because the parameters obtained from the DIC measurements are used in the model. However, it is concluded, that the model is capable of modelling the physical effect of thermal expansion and chemical shrinkage.

It is in general concluded, that the experimental method for determining the residual stress field from photoelastic measurements, based on insert removal, is good. Likewise, it is concluded that the experimental approach for determining the average strain, thermal expansion and chemical shrinkage, using in-situ DIC measurements, is good. However, the latter require elimination of the error introduced by the position of the temperature measurement. It is furthermore concluded, that the numerical model, based on the CHILE material model, can predict the stress and strain of the test specimen with a reasonably accuracy.

Bibliography

Abou-Msallem, et al., 2010. Y. Abou-Msallem, H. Kassem, F. Jacquemin, and A. Poitou. *Experimental Study of the Induced Residual Stresses During the Manufacturing Process of an Aeronautic Composite Material* , 2010.

Analog Devices, 1999. Analog Devices. *Monolithic Thermocouple Amplifiers with Cold Junction Compensation*, 1999. Datasheet for AD594/AD595.

Andersen, et al., 2007. Erik Strandgaard Andersen, Paul Jespersgaard, and Ove Grønbæk Østergaard. *Databog fysik kemi*, 2007. ISBN: 978-87-87229-61-6.

Black, June 2013. Sara Black. *Fair winds for Offshore Wind Farms - Innovations in blades, turbines and foundations are helping spur growth in a very big way.* Composites Technology, June 2013. URL: `http://ct.epubxp.com/i/132116/36`.

Bogetti and Gillespie, 1992. Travis A. Bogetti and John W. Gillespie. *Process-Induced Stress and Deformation in Thick-Section Thermset Composite Laminates*, 1992.

Burguete and Patterson, 1996. R. L. Burguete and E. A. Patterson. *Photomechanical Properties of Some Birefringent Polymers around Their Glass Transition Temperatures*, 1996.

Campbell, 2010. F. C. Campbell. *Structural Composite materials*, 2010. ISBN: 978-1-61503-037-8.

Chemrocks Cryogenics UK, N/A. Chemrocks Cryogenics UK. *Perlite*, N/A. URL: `http://www.dicalite-europe.com/chemrock.htm`.

Christensen and Waals, 1972. R. M. Christensen and F. M. Waals. *Effective Stiffness of Randomly Oriented Fibre Composites*, 1972.

Cook, et al., 2001. Robert D. Cook, David S. Malkus, Michael E. Plesha, and Robert J. Witt. *Concepts and Applications of Finite Element Analysis*, 2001. ISBN: 968-0-471-35605-9.

Dally and Riley, 1991. James W. Dally and William F. Riley. *Experimental Stress Analysis*, 1991.

Doyle and Phillips, 1989. James F. Doyle and James W. Phillips. *Manual on Experimental Stress Analysis.* Society for Experimental Mechanics, 5^{th} edition, 1989.

Fuhong, et al., 2007. Dai Fuhong, Zhang Boming, and Du Shanyi. *A Three-Dimensional Finite Element Analysis of Process-Induced Residual Stress in Resin Transfer Molding Process*, 2007.

Gardiner, 2012. Ginger Gardiner. *Big parts? Big tooling breakthrough.* High Performance Composites, 2012. URL: `http://www.compositesworld.com/articles/big-parts-big-tooling-breakthrough`.

Garvey, **2010**. Brian Garvey. *Carbon Fibre pushrod, a closer look.* f1technical.net, 2010. URL:
`http://www.f1technical.net/forum/viewtopic.php?f=6&t=11557&p=295751#p295751`.

Ghosh, **2004**. Premamoy Ghosh. *Fibre Science and Technology*, 2004. ISBN: 978-0-07-052803-1.

GOM mbH, **2007**. GOM mbH. *Aramis User Information - Hardware*, 2007.

Hahn and Pagano, **1975**. H. T. Hahn and N. J. Pagano. *Curing Stresses in Composite Laminates*, 1975.

Hamilton, **2011**. Andrew Hamilton. *Introduction to Digital Image Correlation (DIC)*, 2011. Lecture in the course "Måleteknik og dataopsamling".

Henriksen, **1984**. Mogens Henriksen. *Nonlinear Viscoelastic Stress Analysis - A Finite Element Approach*, 1984.

HEXION, **2008**. HEXION. *EPIKOTE Resin MGS RIM 035 - Technical Information*, 2008.

Jakobsen, et al., **2013a**. J. Jakobsen, M. Jensen, and J. H. Andreasen. *Thermo-mechanical characterisation of in-plane properties for CSM E-glass epoxy polymer composite materials – Part 1: Thermal and chemical strain*, 2013.

Jakobsen, et al., **2013b**. J. Jakobsen, M. Jensen, and J. H. Andreasen. *Thermo-mechanical characterisation of in-plane properties for CSM E-glass epoxy polymer composite materials – Part 2: Young's modulus*, 2013.

Jakobsen, et al., **2013c**. Johnny Jakobsen, Jens H. Andreassen, Erik Appel Jensen, and Ole T. Thomsen. *Shrinkage and Thermal Expansion Model for a Glass/Epoxy Laminate*, 2013. Poster, presented at CompTest 2013 - 6^{th} International Conference on Composite Testing and Model Identification.

Johnston, et al., **2001**. Andrew Johnston, Reza Vaziri, and Anoush Poursartip. *A Plane Strain Model for Process-Induced Deformation of Laminated Composite Structures*, 2001.

Jones, **1999**. Robert M. Jones. *Mechanics of Composite Materials*, 1999. ISBN: 978-1-56032-712-7.

Juliano, et al., **2007**. T. F. Juliano, M. R. VanLandingham, C. A. Tweedie, and K. J. Van Vliet. *Multiscale Creep Compliance of Epoxy Networks at Elevated Temperatures*, 2007.

Kildegaard, **1985**. Arne Kildegaard. *Handwritten note of lever arm calculations*, 1985.

Kildegaard, **2012**. Arne Kildegaard. *Elasticitetsteori*, 5^{th} edition, 2012.

Kim and Daniel, **2002**. Yeong K. Kim and Isaac M. Daniel. *Cure Cycle Effect on Composite Structures Manufactured by Resin Transfer Molding*, 2002.

Lin and Yi, **1990**. Kuen Y. Lin and Sung Yi. *Analysis of interlaminar stresses in viscoelastic composites*, 1990.

Liu and Lovato, **2008**. C. Liu and M. L. Lovato. *Elastic Constants Determination and Deformation Observation Using Brazilian Disk Geometry*, 2008.

Lund, **2013**. Erik Lund. *Mechanics of Composite Materials and Structures*, 2013. Lecture 1 - Introduction.

Mohr, et al., **2010**. Peter J. Mohr, Barry N. Taylor, and David B. Newell. *CODATA Recommended Values of the Fundamental Physical Constants: 2010*, 2010.

Mouritsen, **2009**. Ole Ø. Mouritsen. *Usikkerhedsvurdering - ved måling med strain gauges*, 2009.

Nairn and Zoller, **1985**. John A. Nairn and Paul Zoller. *Matrix solidification and the resulting residual thermal stresses in composites*, 1985.

Osswald and Menges, **2003**. Tim A. Osswald and Georg Menges. *Materials Science of Polymers for Engineers*, 2^{nd} edition, 2003.

Parlevliet, et al., **2007**. Patrica P. Parlevliet, Harald E.N. Bersee, and Adriaan Beukers. *Residual stresses in thermoplastic composites - A study of the literature - Part II: Experimental techniques*, 2007.

Peiris, **2008**. Thelge Chaminda Peiris. *In-situ cure monitoring and shrinkage analysis of epoxy resin*, 2008.

Phillips, **1998**. James W. Phillips. *Experimental Stress Analysis - 6. Photoelasticity*, 1998.

Rejab, et al., **2008**. M. R. M. Rejab, C. W. Theng, M. M. Rahman, M. M. Noor, and A. N. M. Rose. *An Investigation into the Effects of Fibre Volume Fraction on GFRP Plate*, 2008.

Ruiz and Trochu, **2005**. Edu Ruiz and Francois Trochu. *Numerical analysis of cure temperature and internal stresses in thin and thick RTM parts*, 2005.

Schjødt-Thomsen, **2005**. Jan Schjødt-Thomsen. *Lecture Notes on: Continuum Mechanics - Selected Topics*, 2005. Lecture notes from the course "Solid mechanics with microstructure and Continuum mechanics".

Takahashi, et al., **1987**. Susumu Takahashi, Masahiro Suetsugu, and Akira Shimamoto. *A Basic Study of Plastic Strain Freezing by Photoplastic Experiment*, 1987.

Wacker Silicones, **2013**. Wacker Silicones. *ELASTOSIL® M 4511 - RTV-2 silicone rubber / mold making*, 2013. Product data sheet.

White and Hahn, **1992a**. S. R. White and H. T. Hahn. *Process Modeling of Composite Materials: Residual Stress Development during Cure. Part I. Model Formulation*, 1992.

White and Hahn, **1992b**. S. R. White and H. T. Hahn. *Process Modeling of Composite Materials: Residual Stress Development during Cure. Part II. Experimental Validation*, 1992.

White and Kim, **1998**. Scott R. White and Yeong K. Kim. *Process-Induced Residual Stress Analysis of AS4/3501-6 Composite Material*, 1998.

Winter, 1987. H. H. Winter. *Can the Gel Point of a Cross-linking Polymer Be Detected by the G' - G" Crossover?*, 1987.

Zobeiry, 2006. Nima Zobeiry. *Viscoelastic constitutive models for evaluation of residual stresses in thermoset composites during cure*, 2006.

Part IV

Appendix

A Temperature variation through thickness

An experiment is conducted, where multiple thermocouples is placed in two test specimen, to evaluate the temperature gradient through the thickness. One of the two test specimens is quenched and the other is slowly cooled, to study the effect on the temperature variation.

Two test specimens are prepared, where uncured epoxy is poured into a silicone mould with a steel insert, as described in section 1.2. As seen in figure A.1, three thermocouples are placed in each test specimen. The thermocouples are placed with one near the surface, one near the bottom, and one near the middle.

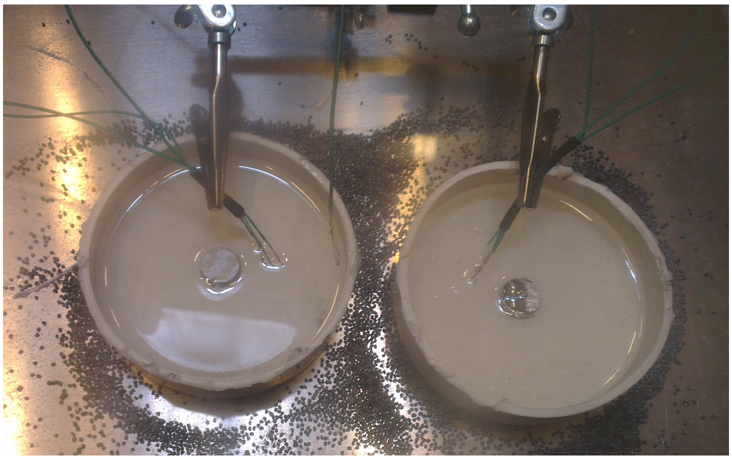

Figure A.1 Image of the two test specimens, with three thermocouples in each.

The test specimens are placed in the oven, at approximately 100 °C. After about three hours, the oven is turned off. One test specimen is quenched in water, and one remains in the oven for slow cooling.

In figure A.2, the temperature from the three thermocouples in the slowly cooled test specimen is shown. Furthermore, the degree of cure is calculated, based on the three different temperatures. The degree of cure is shown as dashed lines.

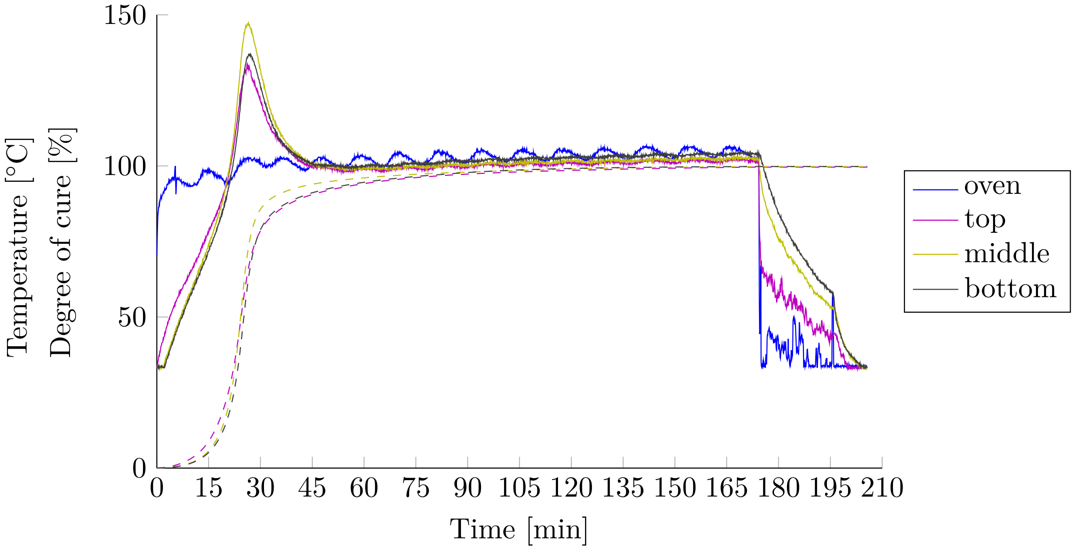

Figure A.2 Temperature and degree of cure at three different positions of the slowly cooled test specimen.

In figure A.3, the temperature and the degree of cure, from the three thermocouples in the quenched test specimen is shown.

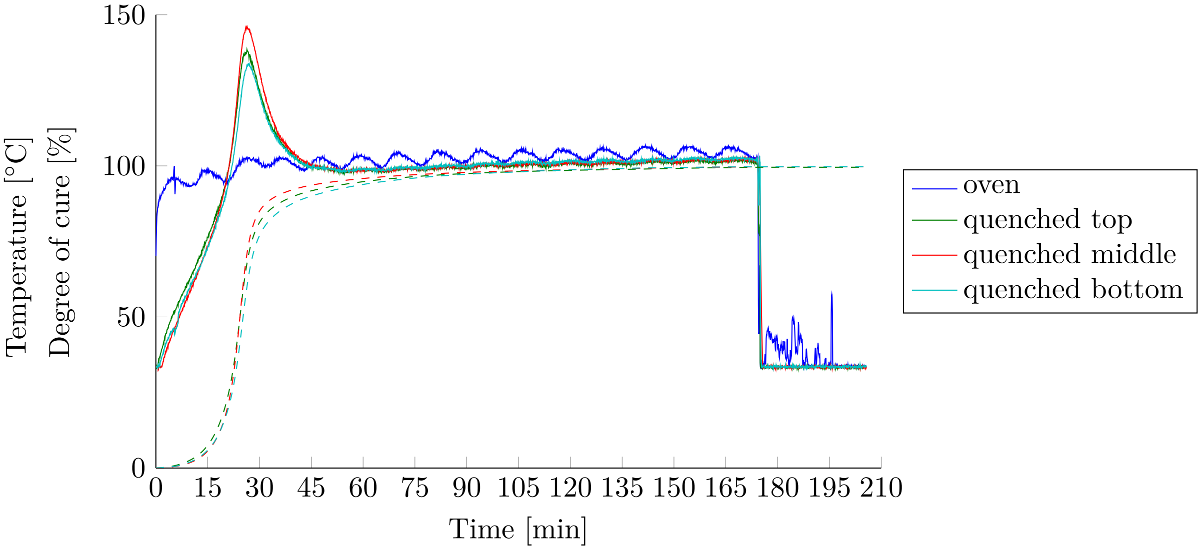

Figure A.3 Temperature and degree of cure at three different positions of the quenched test specimen.

As seen, there is a difference in temperature through the thickness of the test specimens. There is a distinct difference between the maximum temperature of the various thermocouples. Furthermore, there is a difference between the time of the maximum temperatures. The value and the time of the maximum temperatures are given in table A.1 for the thermocouples in both test specimen.

	Temperature		**Time**	
	Quenched	Slowly cooled	Quenched	Slowly cooled
Top	138 °C	134 °C	26 min and 22 s	26 min and 12 s
Middle	146 °C	147 °C	26 min and 27 s	26 min and 32 s
Bottom	134 °C	137 °C	26 min and 47 s	26 min and 57 s

Table A.1 Temperature and time of the maximum temperature of each thermocouple in both test specimen.

As seen in the table, there is a difference in temperature of up to 13 °C, through the thickness of the test specimens. It is also seen, that the temperature peaks first at the top, and last a the bottom.

During the cool down, the temperature difference is even more distinct. In figure A.4 and A.5, the temperature during cool down from figure A.2 and A.3 respectively is shown.

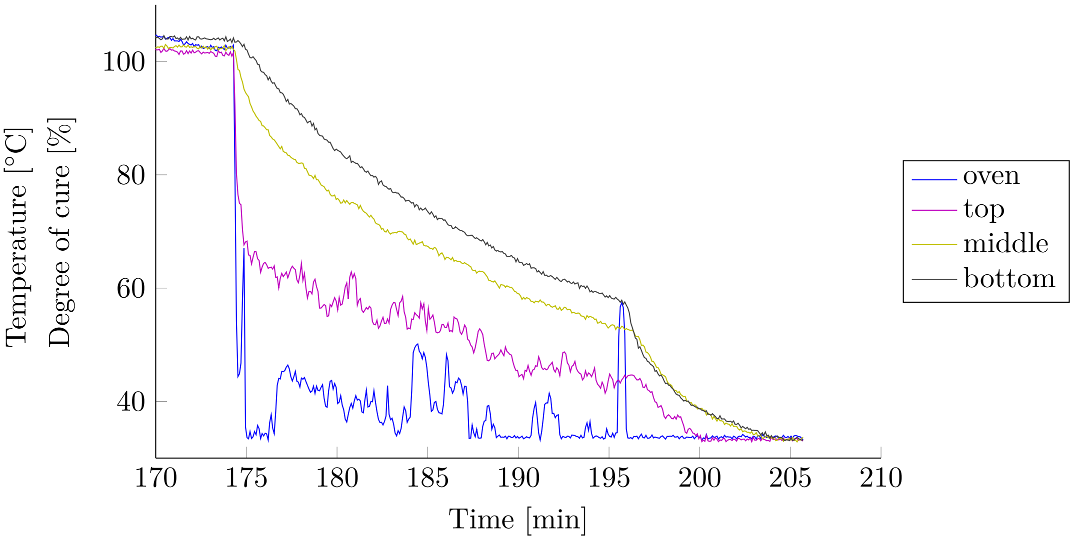

Figure A.4 Temperature at different positions of slowly cooled test specimen, during cooling.

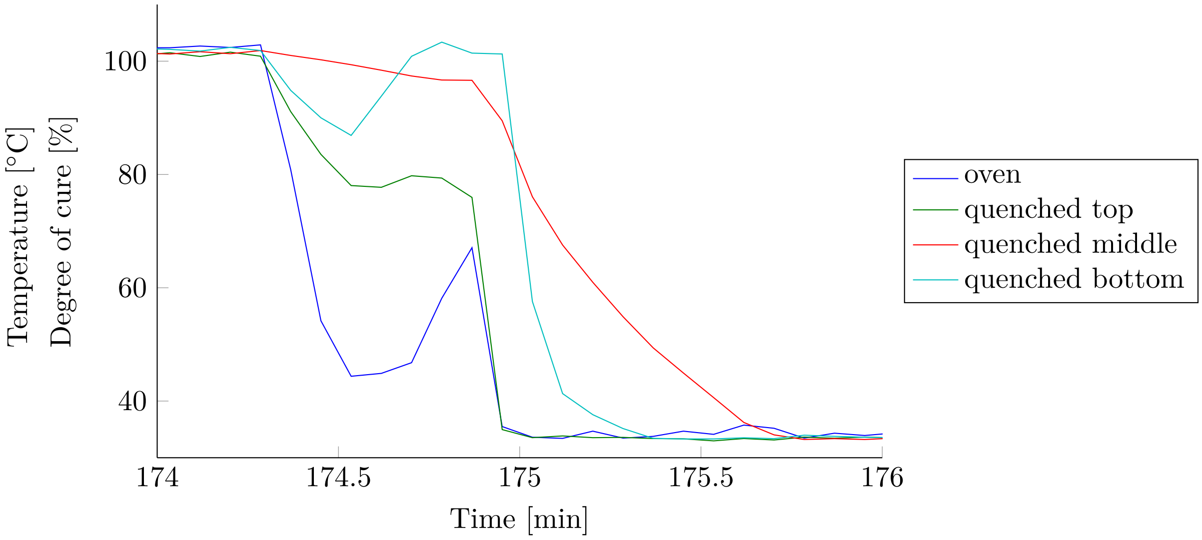

Figure A.5 Temperature at different positions of quenched test specimen, during cooling.

The cooling rate of figure A.4 changes at about 196 min, because the lid of the oven is removed.

The cooling rate of the quenched test specimen is very uneven. This is because, the test specimen is put in water while in the silicone mould. Shortly after, it is taken out of the water to remove the silicone mould, after which it is put back in the water.

Stochastic pattern on surface of test specimens

B

In this appendix it is described how a pattern on surface of the test specimen, which can be used for the digital image correlation (DIC) measurements, is obtained. The pattern must be stochastic and have distinct contrast differences for the DIC system to identify unique patters which can be tracked. Furthermore the pattern must be obtained in a way which does not affect the properties of the epoxy resin significantly, and it must be possible to apply the pattern before gelation occurs in the epoxy resin.

On solid test specimens, the pattern is usually obtained by spray painting with both black and white paint. This has been attempted on the uncured epoxy resin, with the results shown in figure B.1 to B.5. These test specimens has been cured in an oven at 60 °C. In test 1, 2, and 3, white paint has been applied first, after which black drops are sprayed on top. In these test various amounts of white paint were applied, least in test 1 and most in test 3. However, in all three tests the surface separated as the black paint were applied.

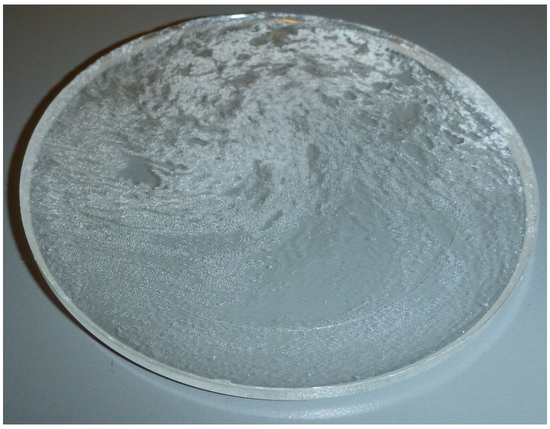

Figure B.1 Surface pattern test 1, spray paint

Figure B.2 Surface pattern test 2, spray paint

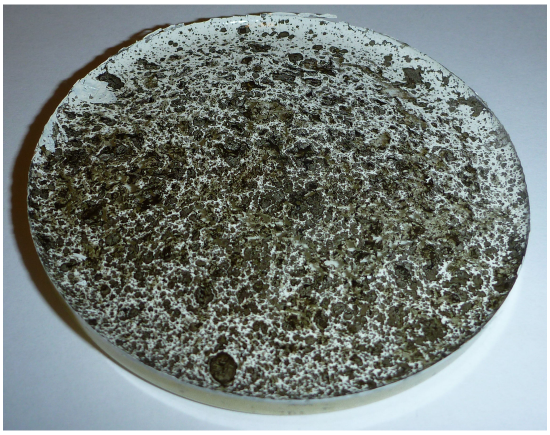

Figure B.3 Surface pattern test 3, spray paint

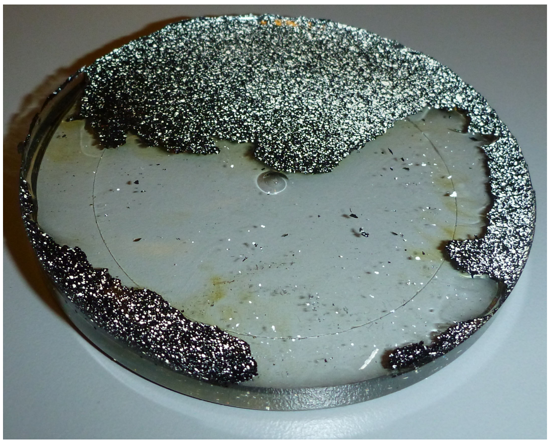

Figure B.4 Surface pattern test 4, spray paint

Figure B.5 Surface pattern test 5, spray paint

In test 4 and 5, black paint were applied first. As seen in figure B.4 and B.5, this surface separates in a different way. However, none of the surfaces patterns are useful for the DIC measurements.

It is possible to spray paint a surface of uncured epoxy resin, as it has been done by Peiris [2008]. However, the specific epoxy resin and spray paint used in this project seems to be incompatible.

Another approach has been to use a kind of powder which is sprinkled on top of the surface. Several different kinds of powder, which appears to be light, have been attempted. These are shown in figure B.6 to B.13. These test specimens has been cured in an oven at 100 °C. Test 6 to 10 is made with: graphite powder, milled carbon fibre, sanding dust of PVC foam and wood, and black pepper. In all of these cases, most of the powder settles at the bottom of the test specimen, even though all of these appear to be light powders. The powders appear light because the bulk density is low. However, the buoyancy is governed by the actual material density, which apparently is too high in these cases.

In the case of the wood sanding dust and the black pepper, the lack of buoyancy might also be due to absorption of the epoxy resin, which could increase the density.

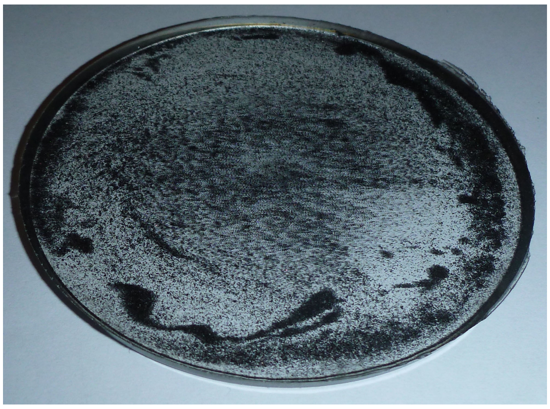

Figure B.6 Surface pattern test 6, graphite powder

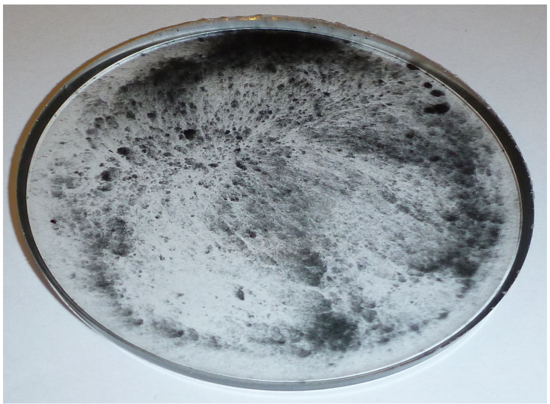

Figure B.7 Surface pattern test 7, milled carbon fibre

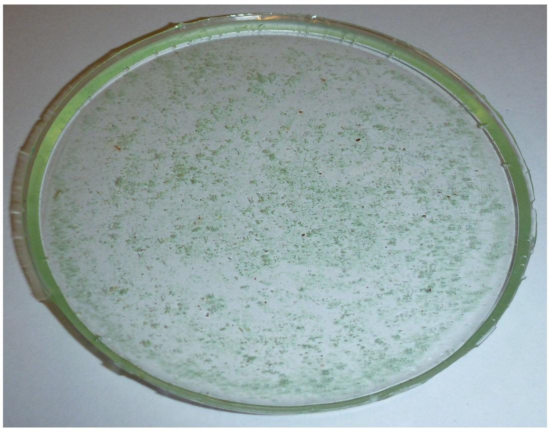

Figure B.8 Surface pattern test 8, PVC foam sanding dust

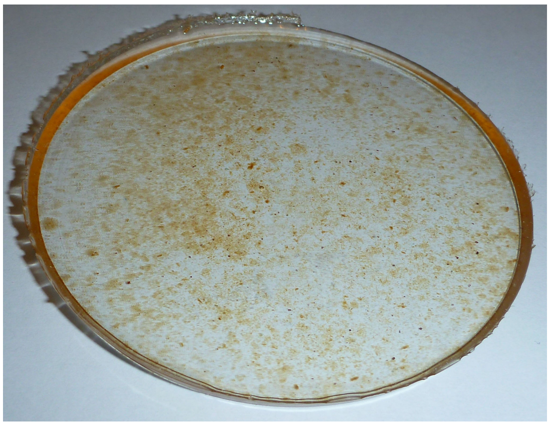

Figure B.9 Surface pattern test 9, wood sanding dust

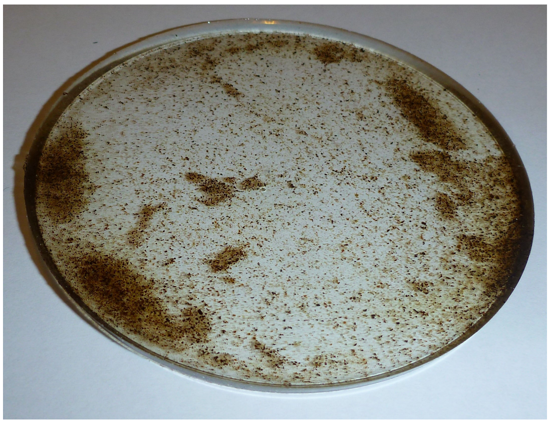

Figure B.10 Surface pattern test 10, black pepper

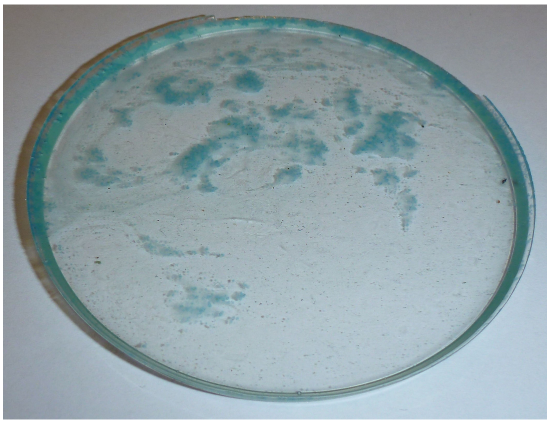

Figure B.11 Surface pattern test 11, blue polystyrene foam sanding dust

Test 11 and 12 consist of two different kind of polystyrene foam sanding dust. Both materials remains buoyant, however, the polystyrene appear do dissolve. This might be because of some kind of solvent in the resin, or because of the high temperature.

In test 13, expanded perlite has been used. Expanded perlite has a closed cellular structure, which causes a very low density. [Chemrocks Cryogenics UK, N/A] Hence, it remains buoyant during the curing process.

Figure B.12 Surface pattern test 12, yellow polystyrene foam sanding dust

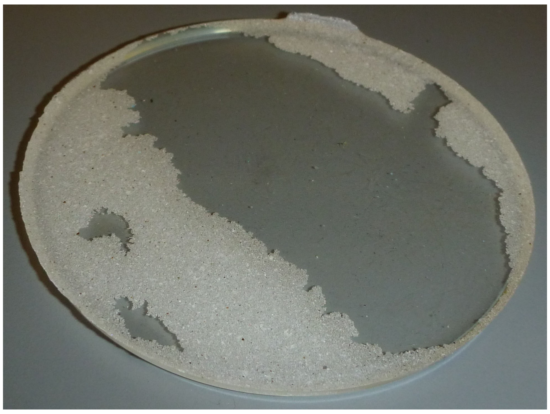

Figure B.13 Surface pattern test 13, expanded perlite

Due to the buoyancy of expanded perlite, it might be possible to use it for the stochastic surface pattern. However, there are two problems: because perlite is white, the surface pattern does not have distinct contrast differences, and as seen in figure B.13, the material seems to drift to the edge of the test specimen.

From the result of test 6 to 13, it is concluded that a material with a closed cellular structure, such as expanded perlite, might be suitable. However, the material should yield more distinct contrast differences. Hence, it is attempted to sprinkle black puppy seeds on the test specimen, which is shown in figure B.14.

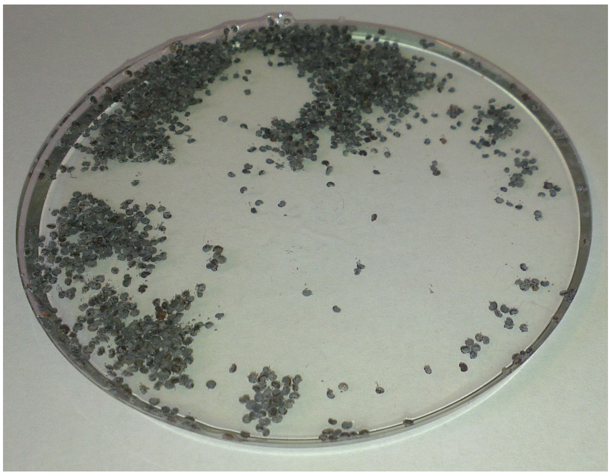

Figure B.14 Surface pattern test 14, black puppy seeds

In test 14, most of the puppy seeds remain buoyant, even though some settle at the bottom. Furthermore, the puppy seeds appear to have a better pattern for the DIC measurements, especially if the black puppy seeds are mixed with white puppy seeds. However, as the expanded perlite, the puppy seeds seem to drift to the edge of the test specimen.

All of the test specimens which are shown above, the pattern has been applied to the surface of the uncured epoxy resin at room temperature, after which the test specimens are placed in a preheated oven. This might be the reason why the material drifts to the edge. By closely inspecting the surface of the test specimens, it is seen that there are small ripples on the surface. This indicates that there is some level of convection in the epoxy resin as it cures, which is assessed to cause the drifting.

To limit the drift, is has been tried to heat the test specimen slowly, to limit the level of convection. This has been done by placing the test specimen with expanded perlite in an oven at room temperature, after which the temperature is ramped to 100 °C over a duration of 60 min. This limits the ripples on the surface, but does not prevent the material from drifting to the edge.

Another test has been performed, where the test specimens are placed in an oven at 100 °C, and black puppy seeds are added at three different stages of the process. In the first specimen, puppy seeds is added before it is placed in the oven. Seconds after it is placed in the oven, the puppy seeds quickly drift towards the edge, probably due to changes in the surface tension. Shortly after that, convection is apparent in the test specimens. As this settles, after 2-3 minutes in the oven, when the epoxy resin is at 40 °C, puppy seeds is added to test number two. After a little while, convection starts again, which causes the puppy seeds to drifts towards the edge. After a total of 8 minutes in the oven, when the epoxy resin is at 60 °C, the convection is settled again. At this time, puppy seeds are added to test number three. These appear to be steady until the epoxy resin is cured.

Hence, it is concluded that the surface pattern can be obtained by sprinkling a material with a closed cellular structure onto uncured epoxy resin, which is preheated to approximately 60 °C. By covering the entire surface with black puppy seeds, as shown in figure B.15, an acceptable surface pattern is obtained. However, due to the size of the puppy seeds (in the order of one millimetre) the seeds might affect the properties of the epoxy resin.

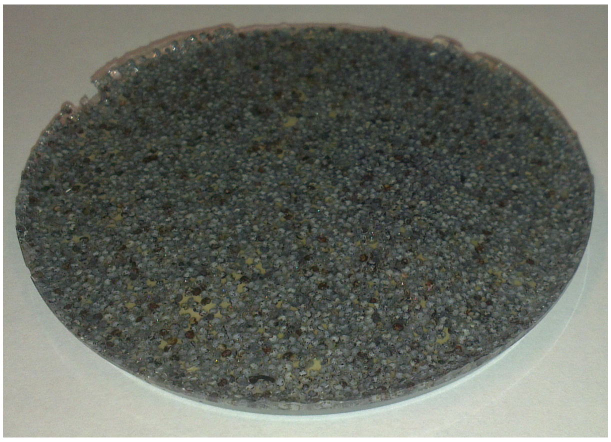

Figure B.15 Surface pattern test 15, black puppy seeds

By using the expanded perlite as it is, it is not possible to obtain a adequate surface pattern. It has been attempted to dye some of the expanded perlite, and sprinkling it on top of undyed expanded perlite. This might be a feasible method, however it is hard to sprinkle the a dyed perlite in a good pattern. As seen in figure B.16, some areas has a lot of dyed perlite, and some areas has not.

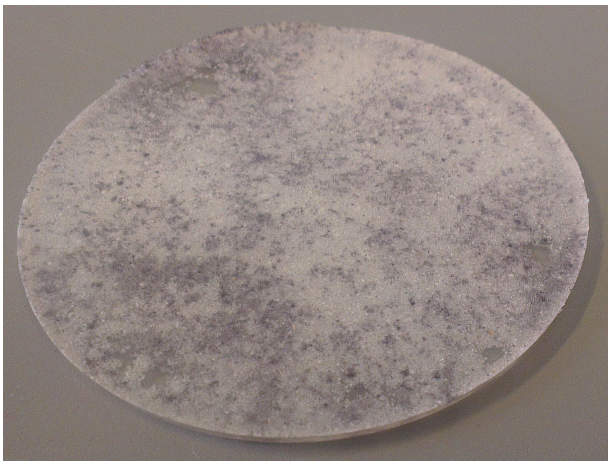

Figure B.16 Surface pattern test 16, dyed perlite on top of undyed perlite

The final pattern, which is used for the DIC measurements is shown in figure B.17. It is obtained by sprinkling a layer of expanded perlite, which is afterwards applied a speckle of black spray paint.

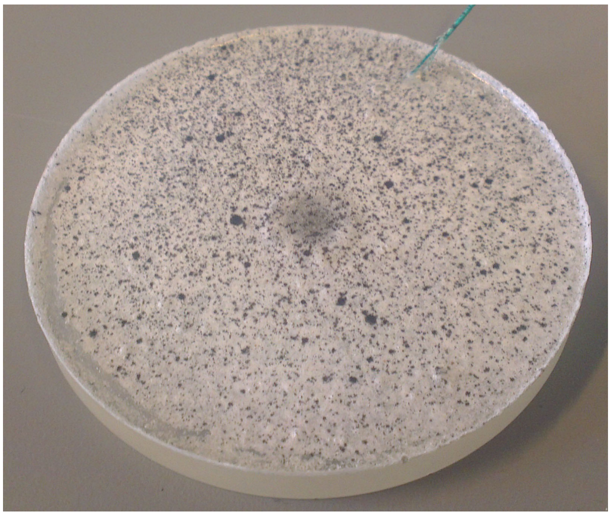

Figure B.17 Surface pattern test 17, expanded perlite, applied a speckle of black spray paint.

Determining of the fringe constant C

To be able to relate the results from the polariscope with the stress field in the test specimen, the fringe constant, f_σ is to be determined. f_σ is related to the difference in principal stress as shown in equation (C.1).

$$\sigma_1 - \sigma_2 = \frac{N f_\sigma}{h} \tag{C.1}$$

where: [Dally and Riley, 1991]

σ_1	First principal stress, [Pa]
σ_2	Second principal stress, [Pa]
N	Fringe order, [ ]
f_σ	Fringe constant, $\left[\frac{\mathrm{N}}{\mathrm{m}}\right]$
h	Height of plane specimen, [m]

f_σ is dependent on the material, and the colour of light used in the polariscope. Hence, an experiment with the specific epoxy system and polariscope, used in this project, is conducted. The test specimen used for determining f_σ is a flat circular disc, known as a Brazilian disc. It is applied a known compressive load at two points, across the diameter of the disc, as shown in figure C.1.

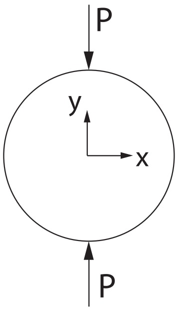

Figure C.1 Sketch of the brazilian disc with the applied load

C.1 Test specimen

The test specimen is cast in an open silicone mould. To reduce the amount of residual stress in the specimen, it is cured at 60 °C for four hours, after which it is cooled slowly by leaving it in the oven to the next day.[1]

The test specimen is wet sanded on both sides to obtain a even thickness, and small irregularities on the edge is removed.

---

[1] By using equation (5.1), the maximum degree of cure is calculated to 0.91 at 60 °C. However, as the experiment is conducted below T_g it is assessed not to affect the result. Furthermore, f_σ is validated in section 4.3.4.

The dimensions of the test specimen are measured with a calliper. The diameter is 58.1±0.3 mm and the thickness is 4.95±0.15 mm. Generally the specimen is thickest at the centre and thinnest at the edges.

C.2 Test set-up

The test set-up is shown in figure C.2

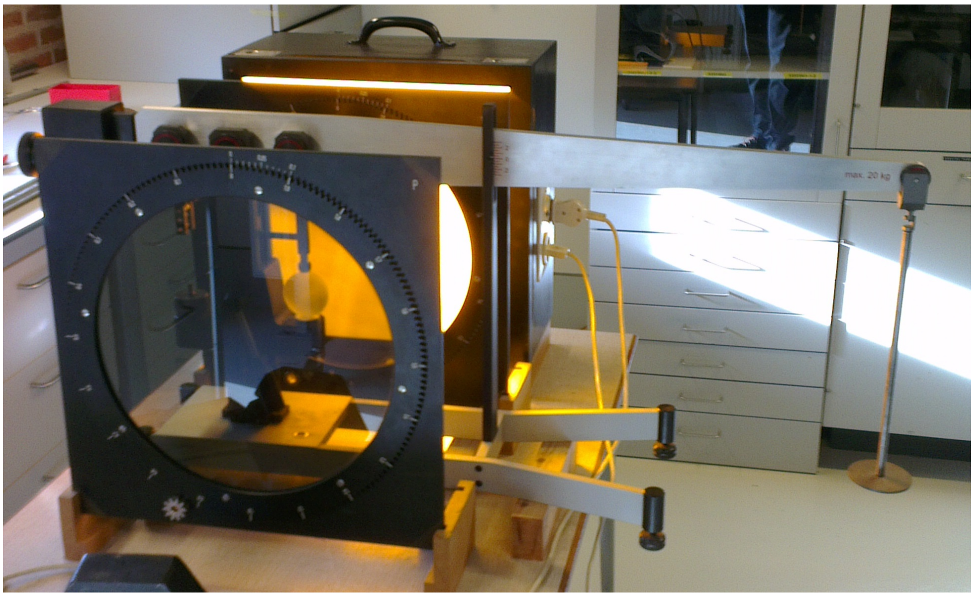

Figure C.2 Test set-up

The load is applied to the specimen by a lever arm, which is placed between the polariser and the analyser.

The lever arm is applied weights on the plate, seen to the right in figure C.2. The lever ratio is matched to the gravitational acceleration, so a mass of 1 kg at the end of the lever cause a force of 100 N on the test specimen [Kildegaard, 1985].

The polariser and the analyser is arranged as a dark field, circular polariscope. Hence, the fringe order is related to the difference in principal stress as shown by equation (C.1).

The test is carried out with various loads, and with either white or monochromatic light[2]. The best result is obtained with monochromatic light and a load of 1000 N. The fringes in the test specimen were captured with a camera.

C.3 Results

The fringes which are captured from the polariscope is shown in figure C.3.

---

[2] Another test specimen, with a thickness of approximately 2 mm, was also used. However, it could not withstand the necessary load without buckling.

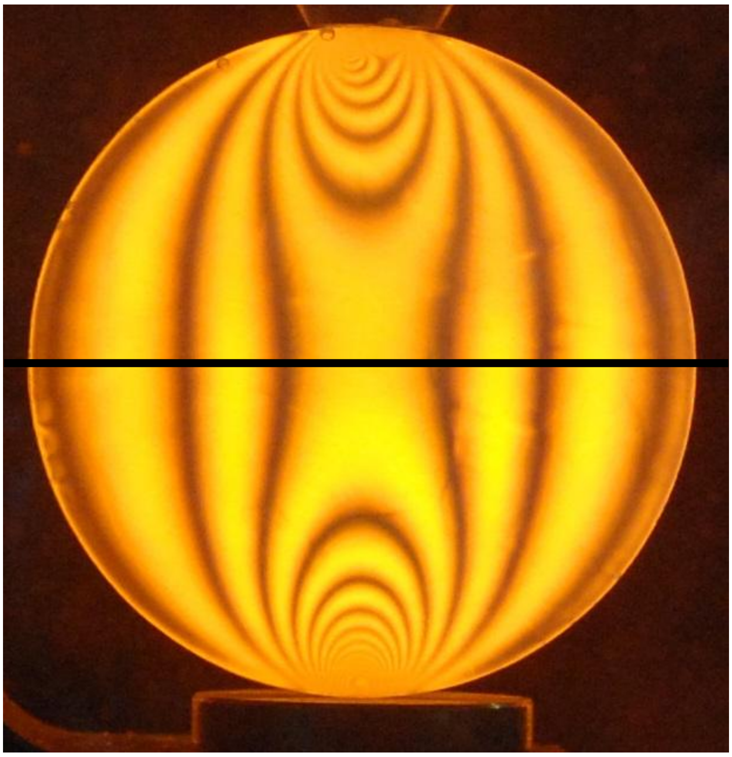

Figure C.3 Fringes in the disc, when a load of 1000 N is applied. The black line mark the horizontal centreline at which the fringes are evaluated.

The fringes are analysed along the horizontal centreline. The RGB-colour levels are plotted separately in figure C.4.

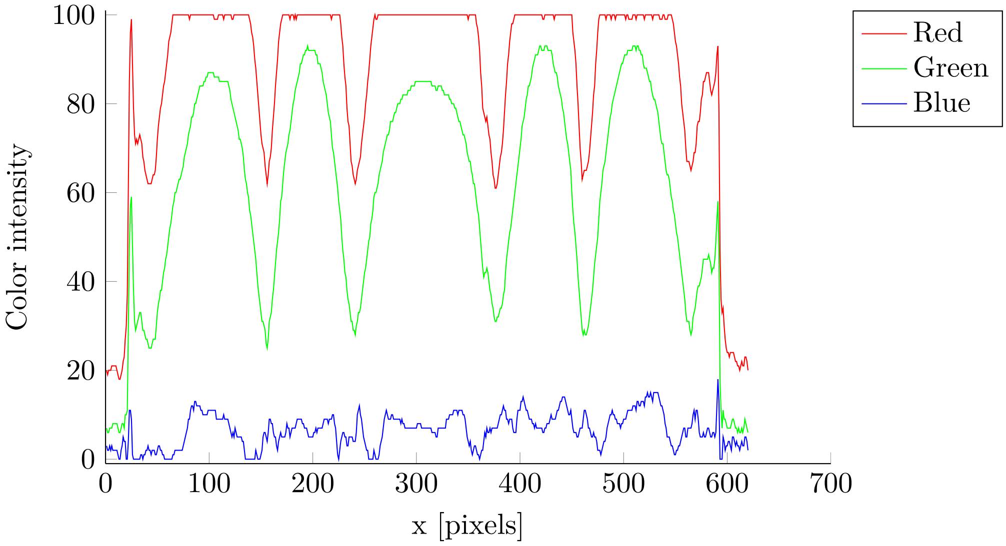

Figure C.4 Colour levels of the picture in figure C.3, along the horizontal centre line of the disc, w.r.t. the position in pixels.

It is assessed that the green and red colour levels are sufficient to determine the location of the fringes. As seen in figure C.4, there are distinct minimums at the centre of each fringe. Furthermore, the edge of the disc is visible from the curves.

It is chosen to use the data from the green colour level, as this is neither over- nor under saturated. The edge of the disc is assumed to be the first pixel, where the colour level exceeds 20 %. From that, the x-axis is scaled to the size of the disc, by which figure C.5 is obtained.

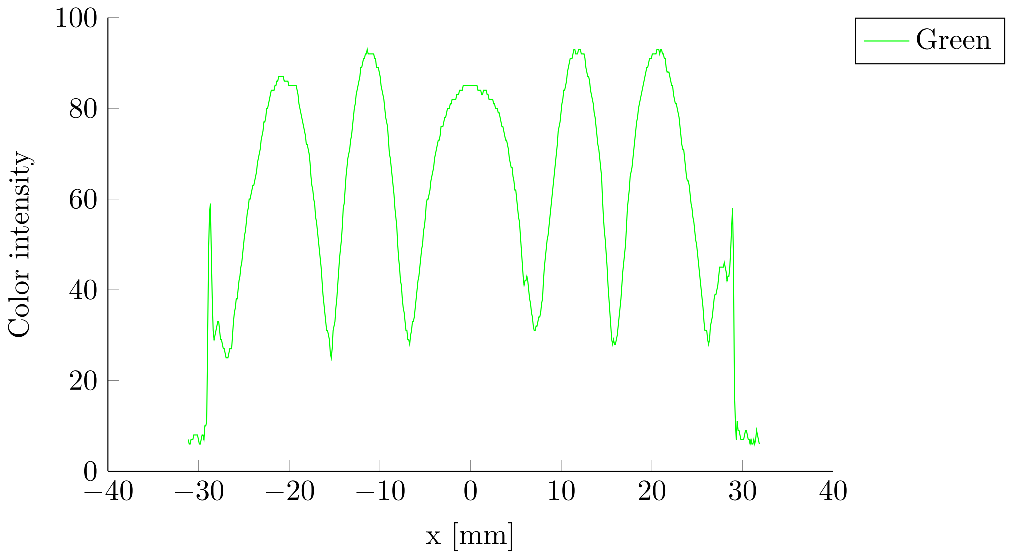

Figure C.5 Green colour levels, along the horizontal centre line of the disc, w.r.t. the position in millimetres.

The location of the fringes is determined as the location of each minimum on the graph. The location and fringe orders of each fringe is given in table C.1.

Location	**Order**
-26.9 mm	0
-15.4 mm	1
-6.7 mm	2
7.1 mm	2
15.9 mm	1
26.3 mm	0

Table C.1 Location and order of each fringe along the horizontal centre line.

C.4 Analytical solution

The analytical solution for the stress field in the brazilian disc is given in equation (C.2) to (C.4).

$$\sigma_x(x,y) = -\frac{2P}{h\pi}\left(\frac{x^2\left(R-y\right)}{\left(R^2+x^2-2Ry+y^2\right)^2} + \frac{x^2\left(R+y\right)}{\left(R^2+x^2+2Ry+y^2\right)^2}\right) + \frac{P}{h\pi R} \tag{C.2}$$

$$\sigma_y(x,y) = -\frac{2P}{h\pi}\left(\frac{\left(R-y\right)^3}{\left(R^2+x^2-2Ry+y^2\right)^2} + \frac{\left(R+y\right)^3}{\left(R^2+x^2+2Ry+y^2\right)^2}\right) + \frac{P}{h\pi R} \tag{C.3}$$

$$\tau_{xy}(x,y) = \frac{8PRxy\left(R^2-y^2-x^2\right)\left(R^2-y^2+x^2\right)}{h\pi\left(R^2+x^2-2Ry+y^2\right)^2\left(R^2+x^2+2Ry+y^2\right)^2} \tag{C.4}$$

where: [Liu and Lovato, 2008]

σ_x	Stress in the x-direction, [Pa]
σ_y	Stress in the y-direction, [Pa]
τ_{xy}	Shear stress w.r.t. the x and y axes, [Pa]
P	Force, [N]
h	Height of plane specimen, [m]
R	Ideal gas constant, $\left[\frac{\mathrm{J}}{\mathrm{mol\,K}}\right]$

At the horizontal centre line, where $y = 0$, the analytical solution reduces to equation (C.5) to (C.7).

$$\sigma_x(x) = \frac{P\left(R^2 - x^2\right)^2}{\pi R h \left(R^2 + x^2\right)^2} \tag{C.5}$$

$$\sigma_y(x) = \frac{P\left(2R^2x^2 - 3R^2 + x^4\right)}{\pi R h \left(R^2 + x^2\right)^2} \tag{C.6}$$

$$\tau_{xy}(x) = 0 \tag{C.7}$$

The stress distribution is plotted in figure C.6.

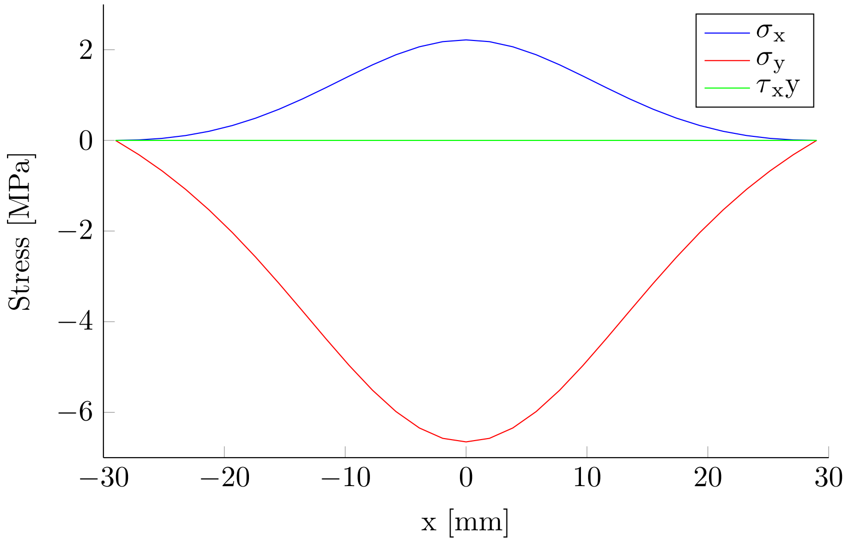

Figure C.6 Distribution of each component of the stress, along the horizontal centre line of the disc.

C.5 Fringe constant

From the location of each fringe, given in table C.1, and the analytical stress field, shown in figure C.6, the fringe constant is determined. Equation (C.1) is solved w.r.t. f_σ, where σ_x and σ_y is inserted as the principal stresses:

$$f_\sigma = \frac{h\left(\sigma_x - \sigma_y\right)}{N} \tag{C.8}$$

Equation (C.8) is evaluated for the location of each fringe. The results is given in table C.2.

Location	**Order**	σ_1-σ_2	f_σ
-26.9 mm	0	0.36 MPa	-
-15.4 mm	1	3.89 MPa	19 253 $\frac{\text{N}}{\text{m}}$
-6.7 mm	2	7.56 MPa	18 714 $\frac{\text{N}}{\text{m}}$
7.1 mm	2	7.43 MPa	18 394 $\frac{\text{N}}{\text{m}}$
15.9 mm	1	3.66 MPa	18 103 $\frac{\text{N}}{\text{m}}$
26.3 mm	0	0.48 MPa	-

Table C.2 Location and order of each fringe along the horizontal centre line.

The average value of the fringe constants, presented in table C.2 is f_σ=18 616 $\frac{\text{N}}{\text{m}}$. The principal stress difference is evaluated at each fringe by using the averaged value of f_σ in equation (C.1). This is compared with the analytical solution in figure C.7.

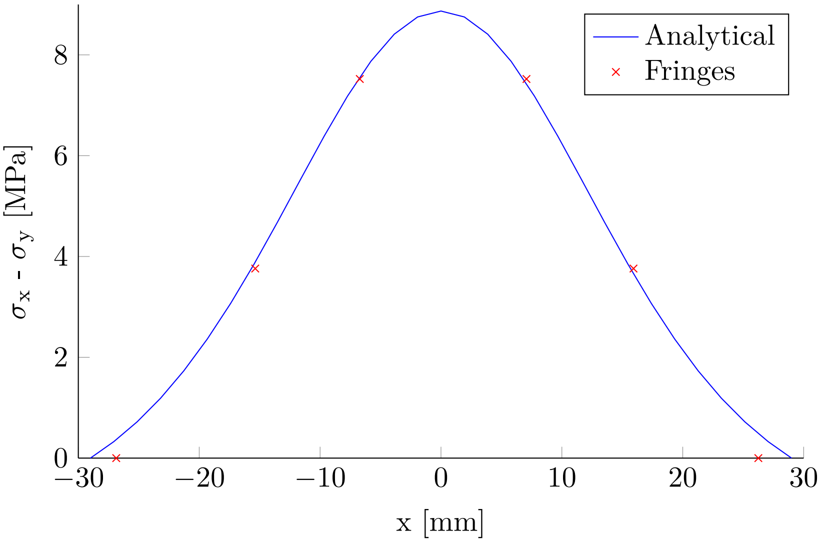

Figure C.7 Distribution of each component of the stress, along the horizontal centre line of the disc.

As seen in figure C.7, there is good correlation at the fringes of 1^{st} and 2^{nd} order. The fringes of order 0 should be located at the edge of the disc. However, they are located a few millimetres from the edge. This is probably due to residual stresses in the test specimen. Even though there might be residual stress throughout the specimen, there is only expected to be a difference in principal stresses close to the edges. Hence, at the fringes of 1^{st} and 2^{nd} , the photoelastic measurements are not expected to be affected by these. It is furthermore seen, that the position of the fringes appear to be offset slightly to the right. This, however, is not considered to affect value of f_σ, because it is determined as the average of the values in figure C.7.

Hence, the value f_σ=18 616 $\frac{\text{N}}{\text{m}}$, is used as the fringe constant throughout this project.

Finite element analysis of test specimen without insert, with detrimental load

D

In this appendix, it is described how finite element analysis (FEA) is conducted, to validate the fringe constant, as described in section 4.3.4. The FEM model is coded in MATLAB, during this project, and is appended on the CD, appendix I.

Due to symmetry, only a quarter of the geometry is considered. As seen in figure D.1, the left and lower boundaries are applied symmetry conditions.

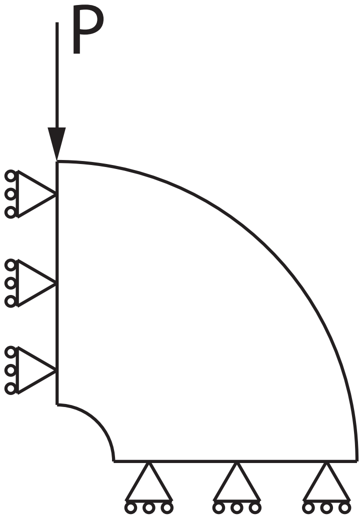

Figure D.1 Load and boundary conditions of FEM

The geometry is considered with a unit thickness and afterwards divided with the average thickness of each of the test specimens.

In appendix I, the stress field is compared with the experimental data, as the stress relative to the load. Hence the simulation is conducted with a unit load. Due to the symmetry, only $\frac{1}{2}$ N is applied.

The model consist of isoparametric 4 node elements, which are formulated according to Cook et al. [2001], chapter 6. The geometry is meshed as seen in figure D.2.

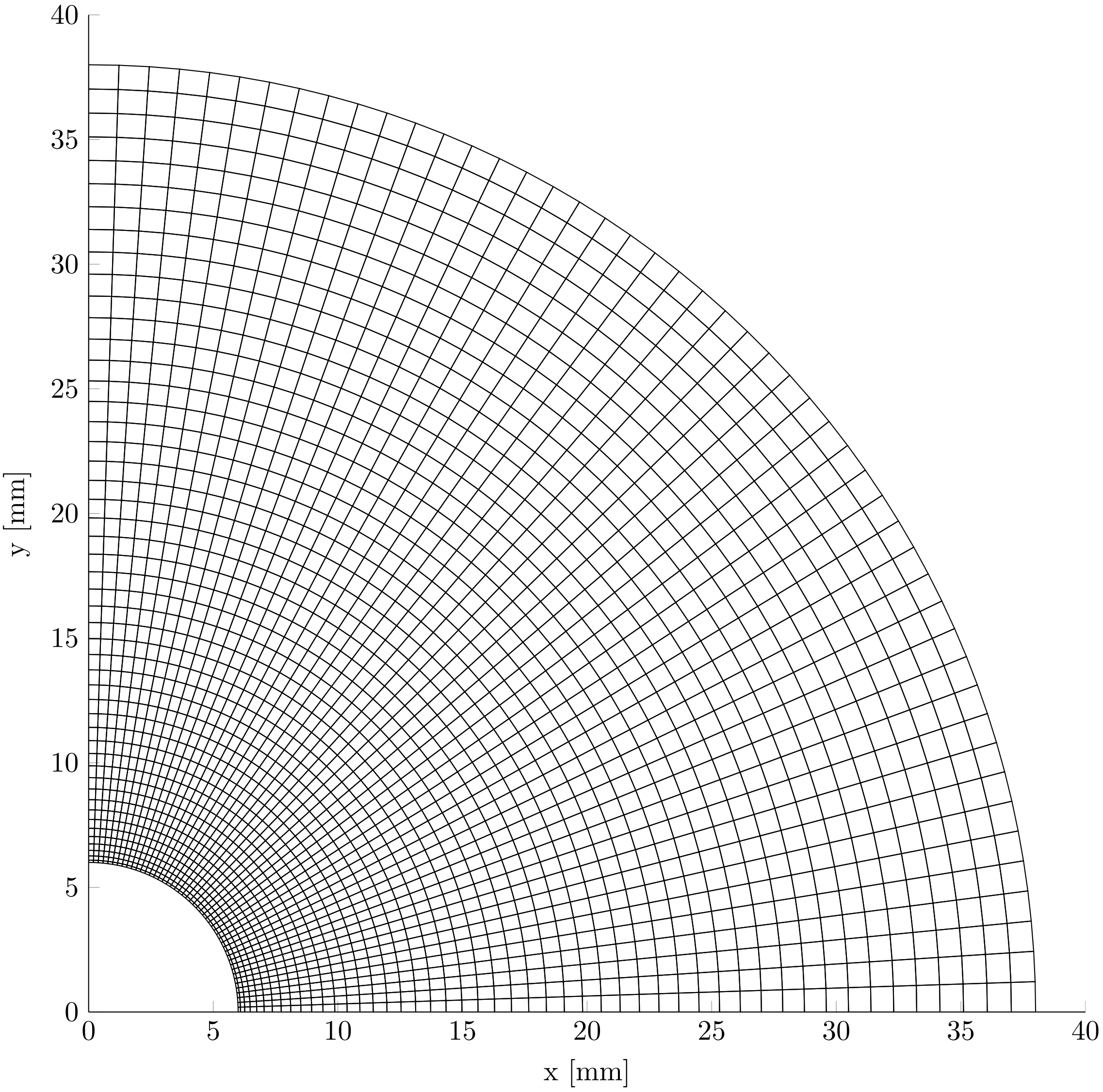

Figure D.2 Mesh in FEM model

The material properties and dimensions, given in table D.1 has been used in the simulation.

Nomenclature	Description	Value
ν	Poisson's ratio	0.37
E	Young's modulus	2.7 GPa
r_i	Inner radius	6 mm
r_o	Outer radius	38 mm

Table D.1 The material properties and dimensions

Young's modulus for epoxy E

In this appendix, an expression is derived for Young's modulus of the matrix material, as a function of Young's modulus of a composite. This is done by expressing the properties of the composite, dependent on the fibre and matrix properties respectively, and solving this expression with respect to Young's modulus of the matrix material.

The distance between the clamps is smaller than the length of the fibres. Hence, methods for determining the properties of continuous fibre composites are used.

The properties of a lamina of an unidirectional (UD) fibre composite can be expressed as the compliance matrix, S_{ij}. If the fibres are aligned with the coordinate system, as shown in figure E.1, the compliance matrix can be expressed as equation (E.1).

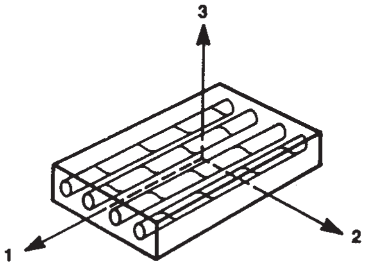

Figure E.1 UD fibre composite with fibres aligned with the coordinate system. [Jones, 1999]

$$S_{ij} = \begin{bmatrix} S_{11} & S_{12} & 0 \\ S_{12} & S_{22} & 0 \\ 0 & 0 & S_{66} \end{bmatrix} \tag{E.1}$$

$$S_{11} = \frac{1}{E_1} \tag{E.2}$$

$$S_{22} = \frac{1}{E_2} \tag{E.3}$$

$$S_{66} = \frac{1}{G_{12}} \tag{E.4}$$

$$S_{12} = -\frac{\nu_{12}}{E_1} \tag{E.5}$$

where: [Jones, 1999]

S_{ij}	Compliance matrix, $\left[\mathrm{Pa}^{-1}\right]$
E_1	Young's modulus along axis 1, [Pa]
E_2	Young's modulus along axis 2, [Pa]
G_{12}	Shear modulus w.r.t. axis 1 and 2, [Pa]
ν_{12}	Poisson's ratio w.r.t. axis 1 and 2, [ ]

Each term in equation (E.2) to (E.5) can be obtained from the properties of the matrix material and the fibre material. One approach is the "Mechanics of Materials Approach", where each property is determined from the "rule of mixture", as given in equation (E.6) to (E.9).

$$E_1 = E_f V_f + E_m(1 - V_f) \tag{E.6}$$

$$E_2 = \frac{E_f E_m}{E_f(1 - V_f) + E_m V_f} \tag{E.7}$$

$$\begin{aligned} G_{12} &= \frac{G_f G_m}{G_f(1 - V_f) + G_m V_f} \\ &= \frac{E_f E_m}{2\left(E_f - E_f V_f + E_m V_f + E_f \nu_m + E_m V_f \nu_f - E_f V_f \nu_m\right)} \end{aligned} \tag{E.8}$$

$$\nu_{12} = \nu_m(1 - V_f) + \nu_f V_f \tag{E.9}$$

where: [Jones, 1999]

E_f	Young's modulus of the fibre material, [Pa]
V_f	Volume fraction of fibres, [ ]
E_m	Young's modulus of the matrix material, [Pa]
G_f	Shear modulus of the fibre material, [Pa]
G_m	Shear modulus of the matrix material, [Pa]
ν_f	Poisson's ratio of the fibre material, [ ]
ν_m	Poisson's ratio of the matrix material, [ ]

If the fibres of the lamina is not aligned with the axes of the coordinate system, equation (E.1) is rotated to obtain equation (E.10).

$$\bar{S}_{ij}\ (\theta) = \begin{bmatrix} \bar{S}_{11}(\theta) & \bar{S}_{12}(\theta) & \bar{S}_{16}(\theta) \\ \bar{S}_{12}(\theta) & \bar{S}_{22}(\theta) & \bar{S}_{26}(\theta) \\ \bar{S}_{16}(\theta) & \bar{S}_{26}(\theta) & \bar{S}_{66}(\theta) \end{bmatrix} \tag{E.10}$$

where:

$\bar{S}_{ij}\ (\theta)$	Rotated compliance matrix, $\left[\mathrm{Pa}^{-1}\right]$
θ	Angle between fibre direction and axis 1, [rad]

It is assumed, that the compliance matrix of a CSM composite can be considered as the average of equation (E.10), when θ is varied from 0 to π, as in equation (E.11).

$$S_{ij_{CSM}} = \int_0^{\pi} \frac{\bar{S}_{ij}\ (\theta)}{\pi} \mathrm{d}\theta \tag{E.11}$$

where:

$S_{ij_{CSM}}$	Compliance matrix for CSM fibre composite, $\left[\mathrm{Pa}^{-1}\right]$

The CSM lamina is transversely isotropic, hence $S_{11_{CSM}}$ and $S_{22_{CSM}}$ is equal to the inverse Young's modulus. Thus, it is only necessary to determine the averaged value of $\bar{S}_{11}\ (\theta)$.

$$\frac{1}{E_{CSM}} = \int_0^{\pi} \frac{\bar{S}_{11}\ (\theta)}{\pi} \mathrm{d}\theta \tag{E.12}$$

where:

E_{CSM}	In-plane Young's modulus for CSM composite, [Pa]
$\bar{S}_{11}\ (\theta)$	Component of rotated compliance matrix, $\left[\mathrm{Pa}^{-1}\right]$

$\bar{S_{11}}\left(\theta\right)$ is calculated from equation (E.13).

$$\bar{S_{11}}\left(\theta\right) = S_{11}\cos\left(\theta\right)^4 + \left(2S_{12} + S_{66}\right)\sin\left(\theta\right)^2\cos\left(\theta\right)^2 + S_{22}\sin\left(\theta\right)^4 \tag{E.13}$$

[Jones, 1999]

Equation (E.13) is inserted in equation (E.12). When the integral is evaluated, equation (E.14) is obtained.

$$\frac{1}{E_{CSM}} = \frac{3S_{11} + 2S_{12} + 3S_{22} + S_{66}}{8} \tag{E.14}$$

By inserting equation (E.2) to (E.9) into equation (E.14), the expression can be written as equation (E.15).

$$aE_m^2 + bE_m + c = 0 \tag{E.15}$$

where:

$$a = \left(1 - V_f\right)\left(5E_{CSM}V_f - 8E_f + 2E_{CSM}V_f\nu_f\right) \tag{E.16}$$

$$b = 2E_fE_{CSM}\left(V_f^2\left(\nu_f + \nu_m + 5\right) - V_f\left(5 + \nu_f + \nu_m\right) + 4\right) - 8E_f^2V_f \tag{E.17}$$

$$c = E_f^2E_{CSM}V_f\left(1 - V_f\right)\left(2\nu_m + 5\right) \tag{E.18}$$

The general solution to equation (E.15) is given as equation (E.19)[1].

$$E_m = \frac{-b - \sqrt{b^2 - 4ac}}{2a} \tag{E.19}$$

Hence, Young's modulus of the matrix material, E_m, is expressed explicit as a function of: E_{CSM}, E_f, V_f, ν_f, and ν_m.

In figure E.2, E_m is shown as a function of E_{CSM}. The fibre volume fraction, V_f, of the test specimens, used to obtain the model in section 5.4.3, are 0.25 [Jakobsen et al., 2013b]. Values of E_f, ν_f, and ν_m are obtained from table lookup. These are given in table 5.4.

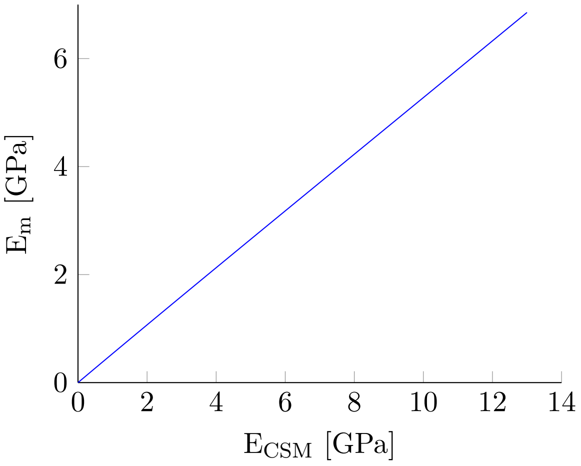

Figure E.2 Young's modulus of the epoxy matrix, as a function of Young's modulus of the composite

---

[1] Equation (E.15) has two solutions, however only one yields a positive result.

Derivations of instantaneous compliance and hereditary strain F

In this appendix, the derivations of the instantaneous compliance, D_I, and the hereditary strain, ε^H, are given for the Maxwell, Kelvin, and CHILE models.

The expression for the strain is formulated as a function of discrete time steps. Afterwards, D_I is determined as the terms which are multiplied by the current stress, whereas ε^H is the remaining terms.

F.1 Maxwell

Equation (5.16) is discretised by expressing it as the sum of n piecewise integrals. The time steps are represented by indexes, where $t_0 = 0$ and $t_n = t$.

$$\begin{aligned}\varepsilon(t) &= \int_0^t \frac{1}{E(t')}\frac{\mathrm{d}\sigma(t')}{\mathrm{d}t'} - \frac{\sigma(t')}{E(t')^2}\frac{\mathrm{d}E(t')}{\mathrm{d}t'} + \frac{\sigma(t')}{\eta(t')}\mathrm{d}t' \\ &= \sum_{k=1}^{n}\int_{t_{k-1}}^{t_k} \frac{1}{E(t')}\frac{\mathrm{d}\sigma(t')}{\mathrm{d}t'} - \frac{\sigma(t')}{E(t')^2}\frac{\mathrm{d}E(t')}{\mathrm{d}t'} + \frac{\sigma(t')}{\eta(t')}\mathrm{d}t' \end{aligned} \tag{F.1}$$

It is assumed, that the σ and E vary linearly with time, in the time interval from t_{k-1} to t_k. Hence, the derivatives with respect to time can be approximated as equation (F.2) and (F.3).

$$\frac{\mathrm{d}\sigma(t')}{\mathrm{d}t'} \approx \frac{\sigma(t_k) - \sigma(t_{k-1})}{t_k - t_{k-1}} \tag{F.2}$$

$$\frac{\mathrm{d}E(t')}{\mathrm{d}t'} \approx \frac{E(t_k) - E(t_{k-1})}{t_k - t_{k-1}} \tag{F.3}$$

These approximations are inserted in equation (F.16), to obtain equation (F.4).

$$\varepsilon(t_n) = \sum_{k=1}^{n}\int_{t_{k-1}}^{t_k} \frac{1}{E(t')}\frac{\sigma(t_k) - \sigma(t_{k-1})}{t_k - t_{k-1}} - \frac{\sigma(t')}{E(t')^2}\frac{E(t_k) - E(t_{k-1})}{t_k - t_{k-1}} + \frac{\sigma(t')}{\eta(t')}\mathrm{d}t' \tag{F.4}$$

The piecewise integrals are approximated by using the trapezoidal integration rule, to obtain equation (F.17).

$$\begin{aligned}\varepsilon(t_n) = \sum_{k=1}^{n}\Bigg\{&\left(\frac{1}{E(t_{k-1})} + \frac{1}{E(t_k)}\right)\frac{\sigma(t_k) - \sigma(t_{k-1})}{t_k - t_{k-1}}\frac{t_k - t_{k-1}}{2} \\ &- \left(\frac{\sigma(t_k)}{E(t_k)^2} + \frac{\sigma(t_{k-1})}{E(t_{k-1})^2}\right)\frac{E(t_k) - E(t_{k-1})}{t_k - t_{k-1}}\frac{t_k - t_{k-1}}{2} \\ &+ \left(\frac{\sigma(t_k)}{\eta(t_k)} + \frac{\sigma(t_{k-1})}{\eta(t_{k-1})}\right)\frac{t_k - t_{k-1}}{2}\Bigg\} \end{aligned} \tag{F.5}$$

Equation (F.17) is rearranged to obtain equation (F.18).

$$\begin{aligned}\varepsilon(t_n) = &\sum_{k=1}^{n} \Bigg\{ \left(\frac{1}{2E(t_{k-1})} + \frac{1}{2E(t_k)} - \frac{E(t_k) - E(t_{k-1})}{2E(t_k)^2} + \frac{t_k - t_{k-1}}{2\eta(t_k)} \right) \sigma(t_k) \\ &- \left(\frac{1}{2E(t_{k-1})} + \frac{1}{2E(t_k)} + \frac{E(t_k) - E(t_{k-1})}{2E(t_{k-1})^2} - \frac{t_k - t_{k-1}}{2\eta(t_{k-1})} \right) \sigma(t_{k-1}) \Bigg\}\end{aligned} \tag{F.6}$$

The last time step is moved out from the sum, as shown in equation (F.7).

$$\begin{aligned}\varepsilon(t_n) = &\sum_{k=1}^{n-1} \Bigg\{ \left(\frac{1}{2E(t_{k-1})} + \frac{1}{2E(t_k)} - \frac{E(t_k) - E(t_{k-1})}{2E(t_k)^2} + \frac{t_k - t_{k-1}}{2\eta(t_k)} \right) \sigma(t_k) \\ &- \left(\frac{1}{2E(t_{k-1})} + \frac{1}{2E(t_k)} + \frac{E(t_k) - E(t_{k-1})}{2E(t_{k-1})^2} - \frac{t_k - t_{k-1}}{2\eta(t_{k-1})} \right) \sigma(t_{k-1}) \Bigg\} \\ &+ \left(\frac{1}{2E(t_{n-1})} + \frac{1}{2E(t_n)} - \frac{E(t_n) - E(t_{n-1})}{2E(t_n)^2} + \frac{t_n - t_{n-1}}{2\eta(t_n)} \right) \sigma(t_n) \\ &- \left(\frac{1}{2E(t_{n-1})} + \frac{1}{2E(t_n)} + \frac{E(t_n) - E(t_{n-1})}{2E(t_{n-1})^2} - \frac{t_n - t_{n-1}}{2\eta(t_{n-1})} \right) \sigma(t_{n-1})\end{aligned} \tag{F.7}$$

The term in equation (F.7) which is multiplied with $\sigma(t_n)$, the stress at the current time step, yields the instantaneous compliance, as given in equation (F.8).

$$D_I(t_n) = \frac{1}{2E(t_{n-1})} + \frac{1}{2E(t_n)} - \frac{E(t_n) - E(t_{n-1})}{2E(t_n)^2} + \frac{t_n - t_{n-1}}{2\eta(t_n)} \tag{F.8}$$

The remaining terms yields the hereditary strain, given in equation (F.9).

$$\begin{aligned}\varepsilon^H(t_n) = &\sum_{k=1}^{n-1} \Bigg(\left(\frac{1}{2E(t_{k-1})} + \frac{1}{2E(t_k)} - \frac{E(t_k) - E(t_{k-1})}{2E(t_k)^2} + \frac{t_k - t_{k-1}}{2\eta(t_k)} \right) \sigma_{ij}(t_k) \\ &- \left(\frac{1}{2E(t_{k-1})} + \frac{1}{2E(t_k)} + \frac{E(t_k) - E(t_{k-1})}{2E(t_{k-1})^2} - \frac{t_k - t_{k-1}}{2\eta(t_{k-1})} \right) \sigma_{ij}(t_{k-1}) \Bigg) \\ &- \left(\frac{1}{2E(t_{n-1})} + \frac{1}{2E(t_n)} + \frac{E(t_n) - E(t_{n-1})}{2E(t_{n-1})^2} - \frac{t_n - t_{n-1}}{2\eta(t_{n-1})} \right) \sigma_{ij}(t_{n-1})\end{aligned} \tag{F.9}$$

F.2 Kelvin

Equation (5.23) is considered as a function of t_n, as shown in equation (F.10).

$$\varepsilon(t_n) = \frac{\sigma(t_n)}{E(t_n)} - \frac{\eta(t_n)}{E(t_n)} \frac{\mathrm{d}\varepsilon}{\mathrm{d}t}(t_n) \tag{F.10}$$

The derivative of ε is approximated as equation (F.11).

$$\frac{\mathrm{d}\varepsilon}{\mathrm{d}t}(t_n) \approx \frac{\varepsilon(t_n) - \varepsilon(t_{n-1})}{t_n - t_{n-1}} \tag{F.11}$$

The approximation is inserted in equation (F.10) to obtain equation (F.12)

$$\varepsilon(t_n) = \frac{\sigma(t_n)}{E(t_n)} - \frac{\eta(t_n)}{E(t_n)} \frac{\varepsilon(t_n) - \varepsilon(t_{n-1})}{t_n - t_{n-1}} \tag{F.12}$$

This causes $\varepsilon(t_n)$ to appear on both sides of the equal sign. Equation (F.12) is solved w.r.t. $\varepsilon(t_n)$ to obtain equation (F.13).

$$\varepsilon(t_n) = \frac{t_n - t_{n-1}}{(E(t_n)(t_n - t_{n-1}) + \eta(t_n))} \sigma(t_n) + \frac{\eta(t_n)\varepsilon(t_{n-1})}{(E(t_n)(t_n - t_{n-1}) + \eta(t_n))} \tag{F.13}$$

From equation (F.13), D_I is determined as the term which is multiplied with the stress, as given in equation (F.14)

$$D_I(t_n) = \frac{t_n - t_{n-1}}{(E(t_n)(t_n - t_{n-1}) + \eta(t_n))} \tag{F.14}$$

ε^H is determined as the remaining term, and is given in equation (F.15).

$$\varepsilon^H(t_n) = \frac{\eta(t_n)\varepsilon(t_{n-1})}{(E(t_n)(t_n - t_{n-1}) + \eta(t_n))} \tag{F.15}$$

F.3 CHILE

Equation (5.31) is formulated as a sum of n piecewise integrals:

$$\begin{aligned}\varepsilon(t_n) &= \int_0^{t_n} D_{CHILE}(t')\frac{\partial\sigma(t')}{\partial t'}\mathrm{d}t' \\ &= \sum_{k=1}^{n}\int_{t_{k-1}}^{t_k} D_{CHILE}(t')\frac{\partial\sigma(t')}{\partial t'}\mathrm{d}t'\end{aligned} \tag{F.16}$$

The time derivative is approximated by equation (F.2).

$$\varepsilon(t_n) = \sum_{k=1}^{n}\int_{t_{k-1}}^{t_k} D_{CHILE}(t')\frac{\sigma(t_k) - \sigma(t_{k-1})}{t_k - t_{k-1}}\mathrm{d}t' \tag{F.17}$$

The terms which are idependent on t' are moved outside the integral.

$$\varepsilon(t_n) = \sum_{k=1}^{n}\frac{\sigma(t_k) - \sigma(t_{k-1})}{t_k - t_{k-1}}\int_{t_{k-1}}^{t_k} D_{CHILE}(t')\mathrm{d}t' \tag{F.18}$$

The integral in equation (F.18) is solved by using the trapezoidal integration rule.

$$\varepsilon(t_n) = \sum_{k=1}^{n}\frac{(\sigma(t_k) - \sigma(t_{k-1}))\left(D_{CHILE}(t_k) + D_{CHILE}(t_{k-1})\right)}{2} \tag{F.19}$$

The last time step is moved out from the sum, as shown in equation (F.20).

$$\begin{aligned}\varepsilon(t_n) =& \sum_{k=1}^{n-1}\frac{(\sigma(t_k) - \sigma(t_{k-1}))\left(D_{CHILE}(t_k) + D_{CHILE}(t_{k-1})\right)}{2} \\ &+ \frac{(\sigma(t_n) - \sigma(t_{n-1}))\left(D_{CHILE}(t_n) + D_{CHILE}(t_{n-1})\right)}{2}\end{aligned} \tag{F.20}$$

The expression is rearranged.

$$\begin{aligned}\varepsilon(t_n) =& \sum_{k=1}^{n-1}\frac{(\sigma(t_k) - \sigma(t_{k-1}))\left(D_{CHILE}(t_k) + D_{CHILE}(t_{k-1})\right)}{2} \\ &- \frac{\sigma(t_{n-1})\left(D_{CHILE}(t_n) + D_{CHILE}(t_{n-1})\right)}{2} + \frac{D_{CHILE}(t_n) + D_{CHILE}(t_{n-1})}{2}\sigma(t_n)\end{aligned} \tag{F.21}$$

The term in equation (F.21) which is multiplied by $\sigma(t_n)$ yields D_I, as given in equation (F.22).

$$D_I(t_n) = \frac{D_{CHILE}(t_n) + D_{CHILE}(t_{n-1})}{2} \tag{F.22}$$

The remaining terms yield ε^H, given in equation (F.23).

$$\begin{aligned}\varepsilon^H(t_n) = & \sum_{k=1}^{n-1} \frac{\left(\sigma(t_k) - \sigma(t_{k-1})\right)\left(D_{CHILE}(t_k) + D_{CHILE}(t_{k-1})\right)}{2} \\ & - \frac{\sigma(t_{n-1})\left(D_{CHILE}(t_n) + D_{CHILE}(t_{n-1})\right)}{2}\end{aligned} \tag{F.23}$$

G Convergence study

In this appendix, a convergence study of the model is presented. It is studied how the number of elements and time steps influence the results.

The convergence study is conducted for the CHILE model, with the temperature profile of the slowly cooled test specimen in figure 4.8.

G.1 Number of elements

The effect of the number if elements are studied by performing simulations with 500 time steps. The principal stresses are evaluated at three different locations, as a function of the number of elements. The mesh is discretised into an equal number of elements in the radial direction and the tangential direction (along a quarter of the test specimen). In the following figures, the stress is given as a function of $\sqrt{n_{elem}}$, which is the number of elements in the radial or tangential direction. In every case, the stress is evaluated at the bottom row of elements.

In figure G.1, the stress is evaluated, at the midpoint of the element closest to the insert.

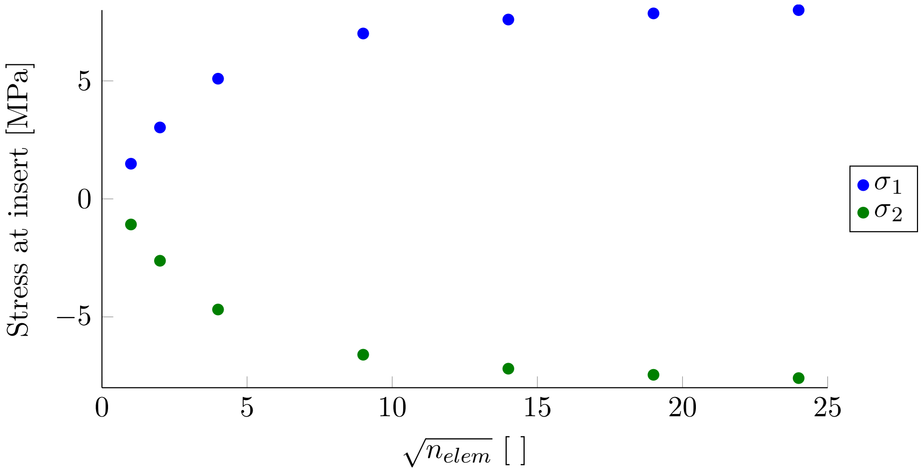

Figure G.1 Convergence of stress at the element, closest to the insert, as a function of the number of elements.

In figure G.2, the stress is evaluated, at the midpoint of the element at the outer edge of the test specimen.

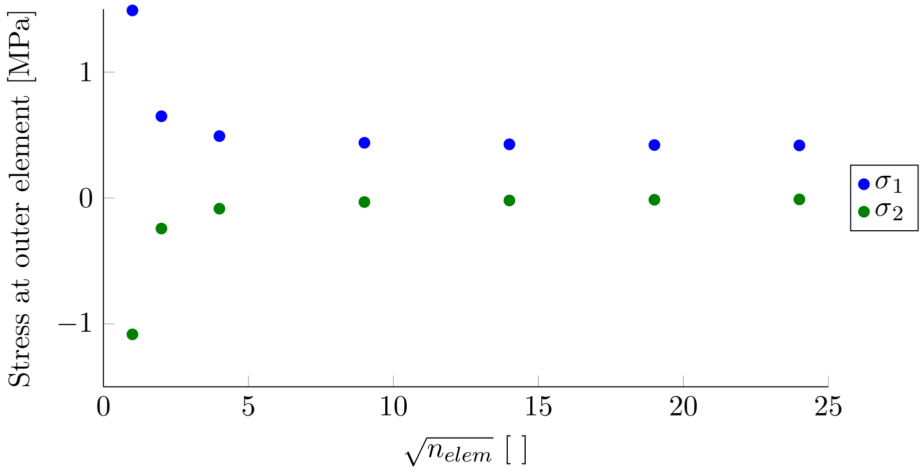

Figure G.2 Convergence of stress at the element, closest to the outer edge, as a function of the number of elements.

It appear, that the stresses of figure G.1 and G.2 converge towards a constant value. However, in both figures, the stress is evalueated at the midpoint of an element. When the mesh is refined, this point is moved. Hence, it can not be concluded whether the stress converge due to increased accuracy of the model, or due to movement of the point, at which the stress is evaluated.

In figure G.3 the convergence of the stress is shown at a constant location. The stress is evaluated at the midpoint of the edge of the insert, and the outer edge of the test specimen. If this point is not at the centre of an element, the stress is linearly interpolated between the neares element centres.

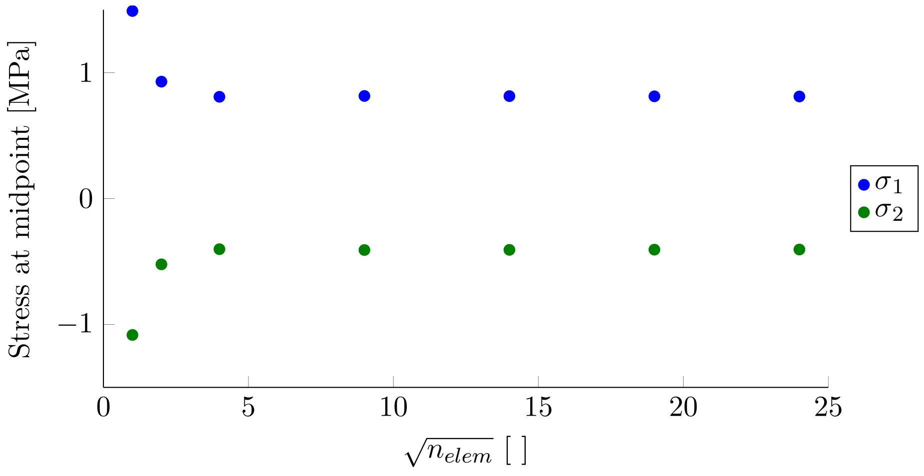

Figure G.3 Convergence of stress at the midpoint between the insert and the outer edge, as a function of the number of elements.

From this study of convergence, when the number of elements are varied, it is concluded that 9 elements in the radial and tangential direction, 81 elements in total, is adequate.

G.2 Time steps

In this section, convergence due to the number of time steps is studied. The simulations are conducted with a mesh of 9x9 elements. The stress is evaluated as described in section G.1.

In figure G.4, the stress is evaluated, at the midpoint of the element closest to the insert.

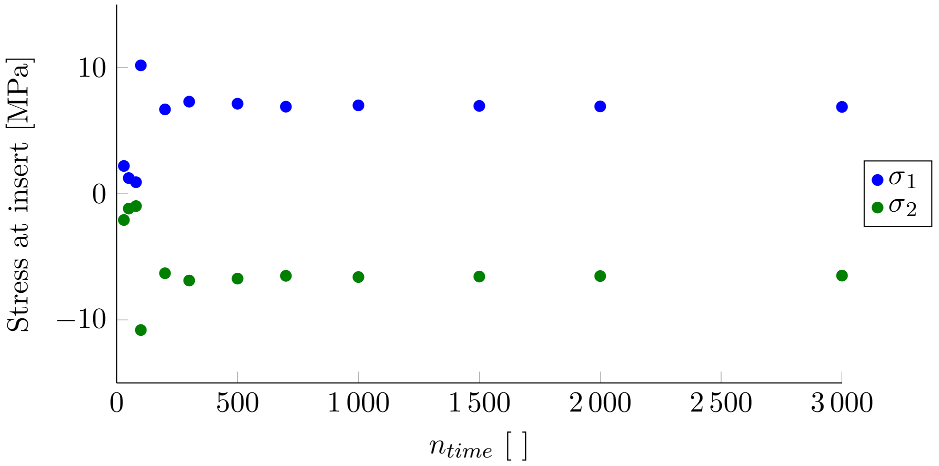

Figure G.4 Convergence of stress at the element, closest to the insert, as a function of the number of time steps.

In figure G.5, the stress is evaluated, at the midpoint of the element closest to the edge of the test specimen.

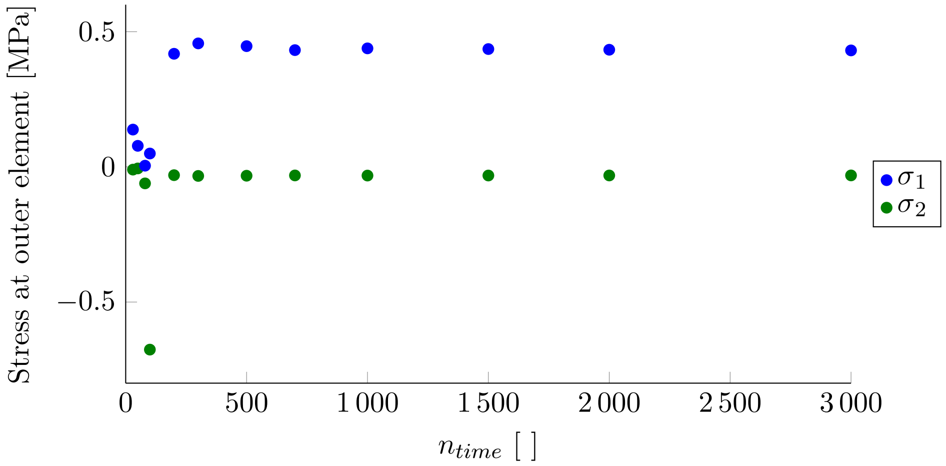

Figure G.5 Convergence of stress at the element, closest to the outer edge, as a function of the number of time steps

In figure G.6, the stress is evaluated, at the midpoint between the edge of the insert, and the outer edge of the test specimen.

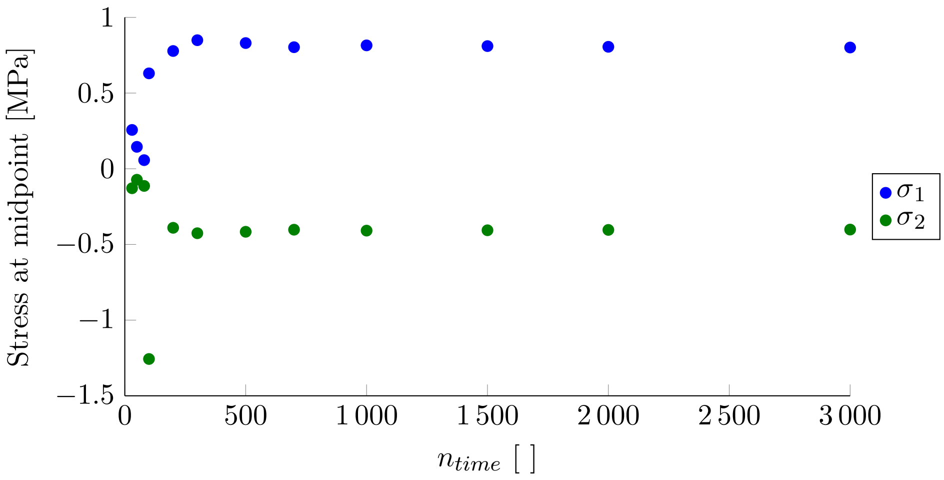

Figure G.6 Convergence of stress at the midpoint between the insert and the outer edge, as a function of the number of time steps.

In figure G.7, the convergence of the volumetric strains. The chemical strain is dependent on the accuracy of the curing model. The thermal strain depends on the accuracy of the temperature profile.

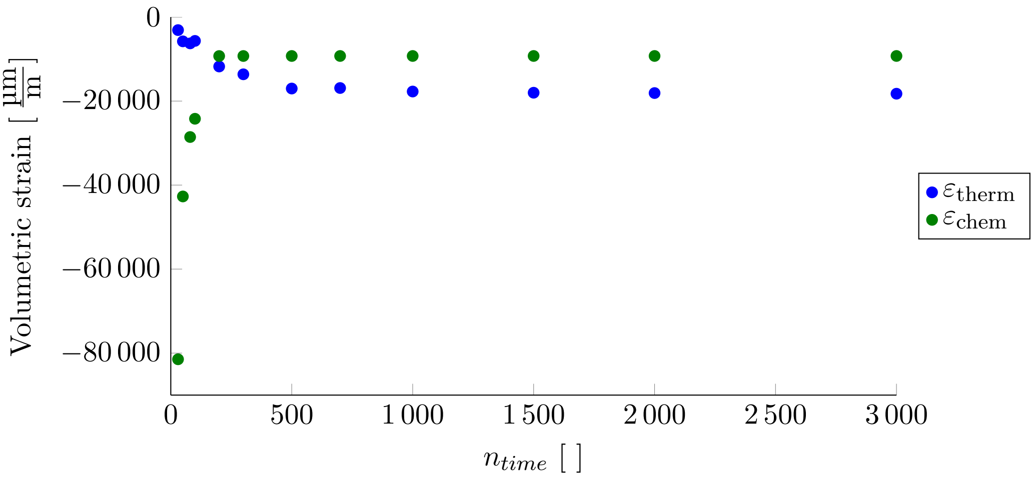

Figure G.7 Convergence of volumetric strainm as a function of the number of time steps.

It is concluded that 1000 time steps is adequate.

Technical drawing of mould for silicone mould

H

In this appendix, the technical drawings of the aluminium mould, used to mould the silicone mould, is appended.

The mould consist of thee parts: an external mould, an internal mould, and a crossbar. The crossbar is assembled with the internal mould, using two M6 screws. In the two threaded holes in the external mould, screws without heads are placed. These screws are used to guide the assembly of the crossbar and the internal mould, when the silicone mould is moulded.

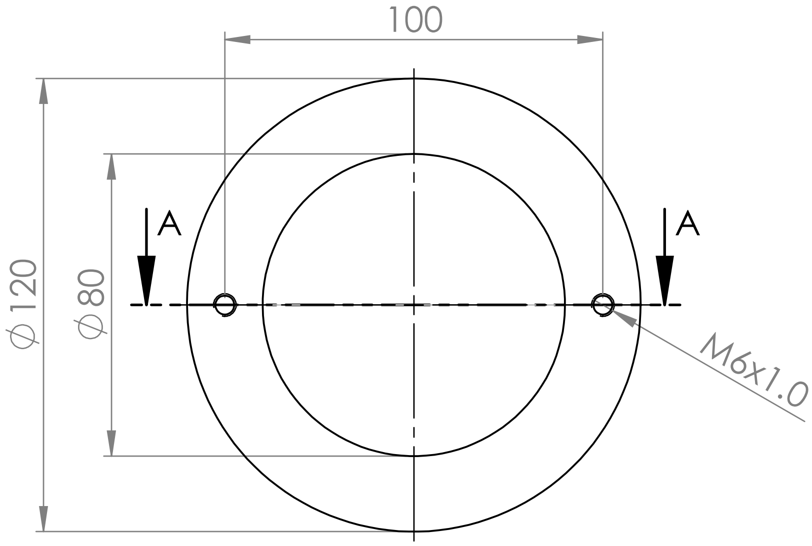

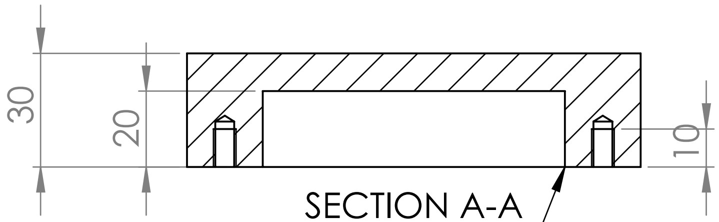

SECTION A-A

Break sharp edges

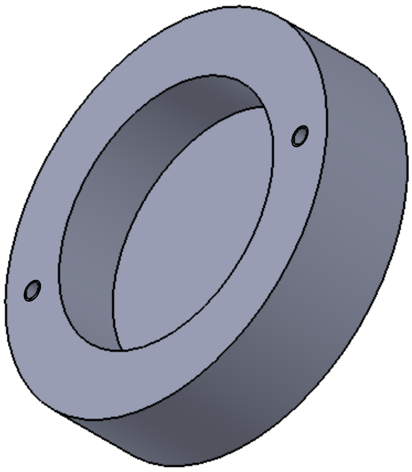

REVISION

Contact person
Jens Jørgensen

MATERIAL:
Alu

TITLE:
External mould

WEIGHT:
SCALE:1:2
DO NOT SCALE DRAWING
SHEET 1 OF 1
A4

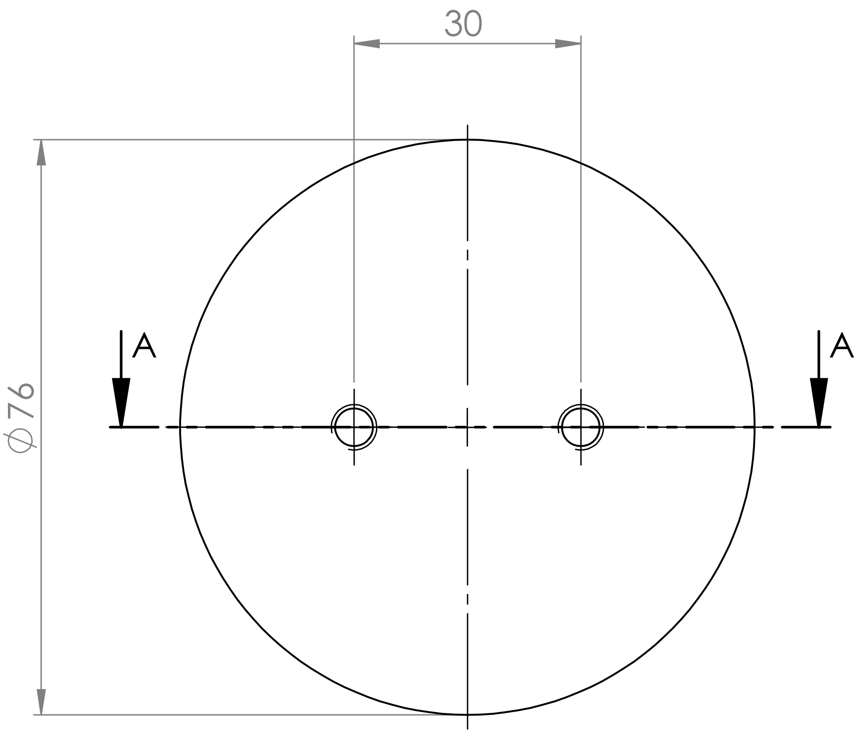

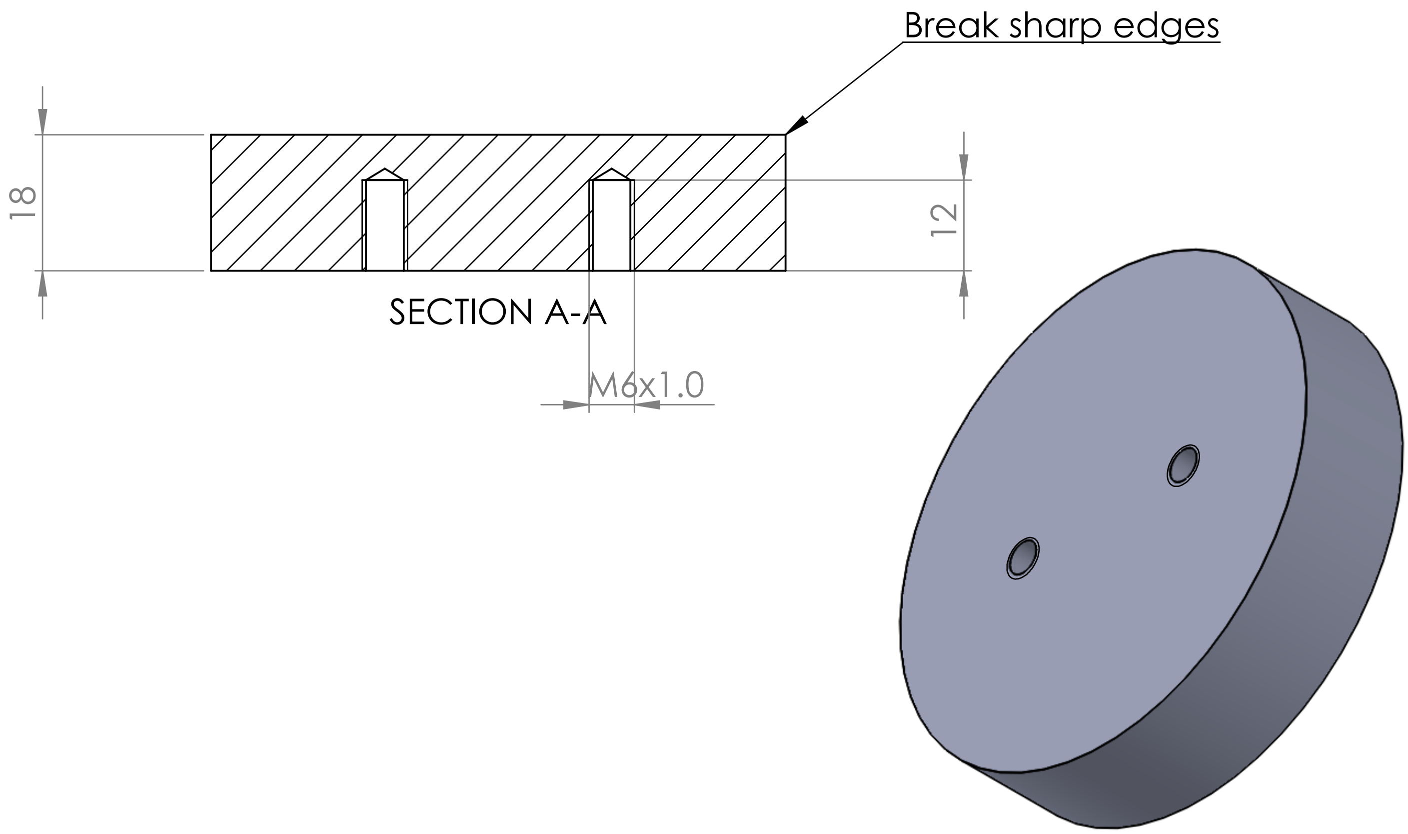

SECTION A-A

REVISION	TITLE: Internal mould
Contact person Jens Jørgensen	
MATERIAL: Alu	
WEIGHT:	SCALE:1:1 DO NOT SCALE DRAWING SHEET 1 OF 1 A4

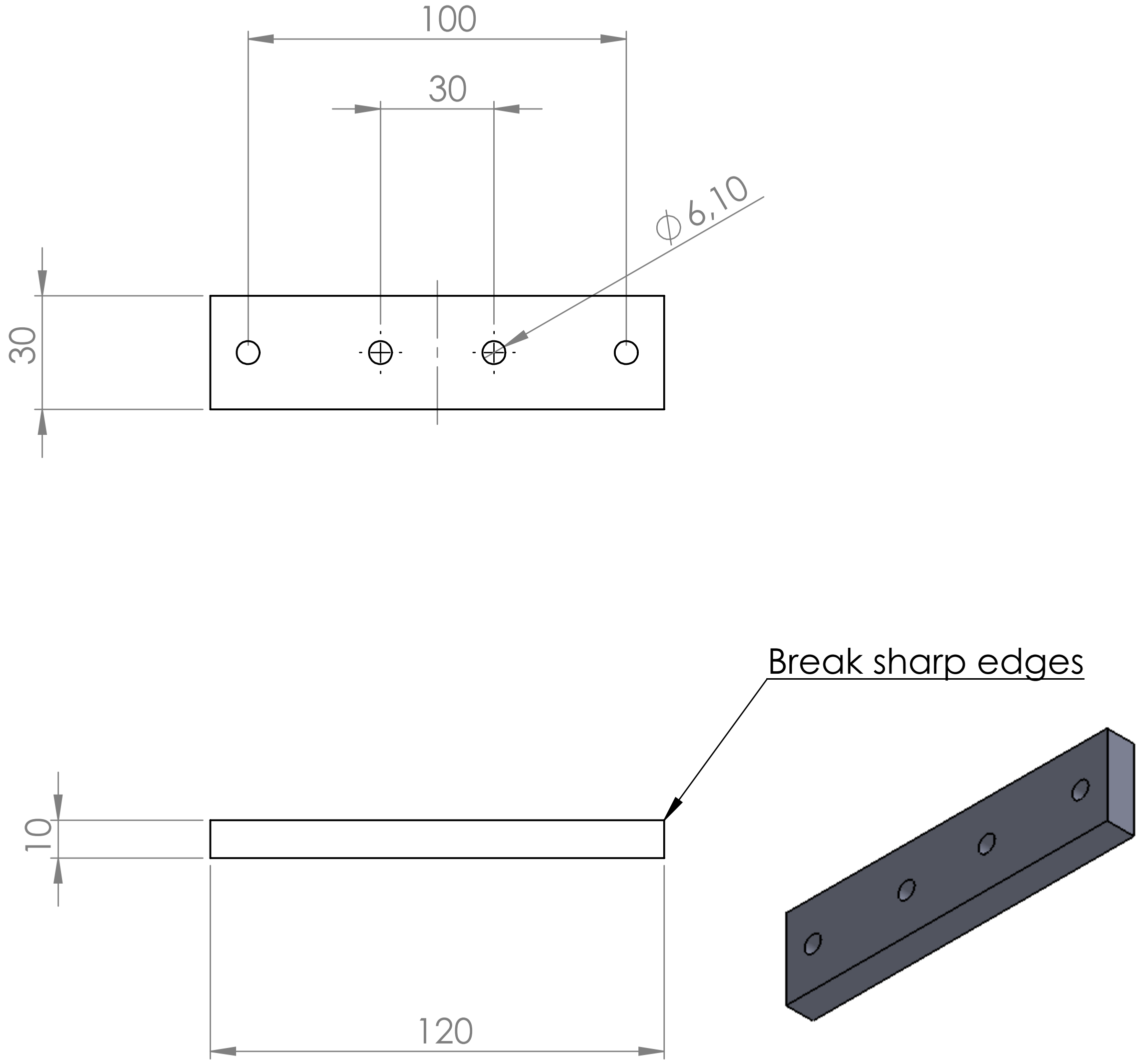

REVISION

Contact person
Jens Jørgensen

MATERIAL:
Alu

WEIGHT:

TITLE:
Crossbar

SCALE:1:2
DO NOT SCALE DRAWING
SHEET 1 OF 1
A4

Appendix CD I

An overview of the files on the appendix CD is given in this appendix.

- **MATLAB**[1]
  - **mainResidualStressModel.m**
    Main script file for non-linear model of process induced stress and deformation. The theory of the model is considered in part II of the report.
  - **mainLinearFEM_Fringeconstant.m**
    Main script file for linear FEM model, used to validate fringe constant, as described in section 4.3.4
  - **data**
    Folder with data files, used in the model
  - **fcn**
    Folder of MATLAB functions, called from the main scripts
- **LabVIEW data acquisition**[2]
  - **Main.vi**
    VI which is used for the data acquisition of the thermocouples. The VI is prepared for seven channels. The data, as well as a time stamp is written to an ASCII file. Furthermore, the degree of curing is calculated from one of the temperature channels, by use of equation (5.2).
  - **CureRate.vi**
    SubVI which is called from **Main.vi**, to calculated the curing rate.
- **DIC measurements**
  - **DIC_THE_MOVIE.avi**
    Animation which is compiled by the images, from both cameras, captured for the DIC measurements. In the top left corner, the time from the start of the experiment is shown.

---

[1] MATLAB code is written and tested in MATLAB R2013b.

[2] VI is programmed and tested in LabVIEW 2013 32-bit with NI-DAQ USB-6009.